

STRUCTURAL STUDIES OF THE CATALYTIC MECHANISMS OF TWO SUPERFAST
METALLOENZYMES: THE CARBONIC ANHYDRASES AND MANGANESE
SUPEROXIDE DISMUTASES

By

JOHN FRANCIS DOMSIC

A DISSERTATION PRESENTED TO THE GRADUATE SCHOOL
OF THE UNIVERSITY OF FLORIDA IN PARTIAL FULFILLMENT
OF THE REQUIREMENTS FOR THE DEGREE OF
DOCTOR OF PHILOSOPHY

UNIVERSITY OF FLORIDA

2009

© 2009 John Francis Domsic

To my parents, Kenneth and Gabrielle Domsic

ACKNOWLEDGMENTS

I would like to thank my mentor, Dr. Robert McKenna for his continued support and guidance. He has provided much insight into my research and has given myriad suggestions that have guided my research down the right path. His enthusiasm for research has been a key part of my motivation and success. I would also like to thank Dr. David Silverman for his mentorship and his availability to answer any questions that I have had throughout the past few years. In addition, I would like to thank the other members of my committee, Dr. Art Edison and Dr. John Aris. My committee has provided me with insight and support for my research that has been a major part of keeping me on track.

I would like to thank my fellow labmates and friends for all of their help throughout my time in the lab. Dr. Mavis Agbandje-McKenna, Dr. Lakshmanan Govindasamy, Dr. Hyun-Joo Nam, and Dr. Chingkuang Tu have provided me with assistance, without which none of this work would have been possible. My fellow graduate students in the McKenna Lab have provided an environment that has made working in the lab a wonderful experience. I would like to thank the undergraduates who I have had the pleasure to work with for all of their assistance with my research. Additionally I would like to acknowledge all of the researchers who I have had the pleasure to collaborate with over the past 4 years. Their assistance and insight was invaluable to this research.

Finally, I would like to thank my family for their continued support and guidance during this important stage of my career.

TABLE OF CONTENTS

	<u>page</u>
ACKNOWLEDGMENTS.....	4
LIST OF FIGURES.....	9
LIST OF ABBREVIATIONS.....	12
ABSTRACT	15
CHAPTER	
1 INTRODUCTION	17
Metalloproteins	17
Superoxide Dismutases	18
The Superoxide Radical	18
Superoxide Dismutases.....	19
Phenotypes of SOD deficiency	20
Catalytic mechanism.....	21
Structural descriptions	22
Carbonic Anhydrase	23
α , β , and γ Carbonic Anhydrases	24
Catalytic mechanism.....	24
Structure	25
α -class Isoforms	27
Carbonic Anhydrase Deficiencies.....	27
2 THE ROLE OF THE DIMERIC INTERFACE IN CATALYSIS BY HUMAN MANGANESE SUPEROXIDE DISMUTASE.....	34
Introduction	34
Materials and Methods.....	35
Enzymes.....	35
Visible Absorption.....	36
Pulse Radiolysis	37
Determination of Manganese and Iron Content.....	37
Crystallography	37
Differential Scanning Calorimetry	38
Results.....	39
Metal Content Analysis.....	39
pH Profile.....	39
Catalysis.....	40
Structural Analysis.....	41
Thermal Stability.....	42
Discussion	42

	Structures	43
	Spectroscopic Properties.....	44
	Catalysis.....	45
	Conclusions	47
3	COMPARATIVE STUDY OF HUMAN AND <i>ESCHERICHIA COLI</i> MANGANESE SUPEROXIDE DISMUTASE: KINETIC AND STRUCTURAL INSIGHTS.....	53
	Introduction	53
	Materials and Methods.....	55
	Enzymes.....	55
	Pulse Radiolysis.....	56
	Crystallization	56
	Data Collection and Refinement.....	56
	Results.....	57
	Catalysis.....	57
	Structural Analysis.....	59
	Discussion	60
	Catalysis.....	61
	Active Site Environment	63
	Conclusions	65
4	SEQUESTRATION OF SUBSTRATE CARBON DIOXIDE IN THE ACTIVE SITE OF HUMAN CARBONIC ANHYDRASE II.....	71
	Introduction	71
	Materials and Methods.....	72
	Enzymes.....	72
	Crystallization	73
	Carbon Dioxide Trapping.....	73
	Data Collection and Processing	74
	Structure Refinement	75
	Results.....	76
	Carbon Dioxide in the Active Site	76
	A Second Carbon Dioxide Binding Site	77
	Additional Protein Structural Features.....	78
	Discussion	78
	Trapping Carbon Dioxide.....	78
	Physiological Relevance.....	79
	Implications For the Catalytic Mechanism	80
	Conclusions	81
5	THE ROLE OF SURFACE RESIDUES IN PROTON TRANSFER BY HUMAN CARBONIC ANHYDRASE II.....	90

Introduction	90
Materials and Methods.....	92
Enzymes.....	92
Crystallization and Data Collection.....	92
Data Processing and Refinement.....	92
¹⁸ O Exchange.....	93
Esterase Activity.....	94
Results.....	95
Catalysis.....	95
Structure.....	96
Discussion	97
Conclusions	98
6 UNDERSTANDING THE MECHANISM OF γ -CA FROM <i>METHANOSARCINA THERMOPHILA</i> : A COMPARISON WITH THE α -CA, HUMAN CARBONIC ANHYDRASE II	105
Introduction	105
Materials and Methods.....	107
Enzymes.....	107
Crystallization and Data Collection.....	108
Refinement.....	109
Results.....	109
Discussion	110
7 CONCLUSIONS AND FUTURE DIRECTIONS	117
Summary and Conclusions	117
Future Directions	120
LIST OF REFERENCES	122
BIOGRAPHICAL SKETCH.....	130

LIST OF TABLES

<u>Table</u>	<u>page</u>
1-1	The tissue specificities, structural topologies, and catalytic activities of the known α -class carbonic anhydrases..... 28
2-1	Rate constants for catalysis by wild-type and mutant human MnSOD 48
2-2	X-ray diffraction data processing and structure refinement statistics for E162D and E162A human MnSOD 48
3-1	X-ray diffraction data processing and structure refinement statistics for F66A and F66L human MnSOD..... 65
3-2	Rate constants for catalysis by wild-type and mutant human and <i>E. coli</i> MnSOD obtained by pulse radiolysis..... 66
3-3	Geometric distances with the active site of wild-type, F66A, and F66L human and wild-type <i>E. coli</i> MnSOD as illustrated in Figure 3-7..... 66
4-1	Data collection and refinement statistics for the CO ₂ -bound holo and apo HCA II structures. 82
4-2	Distances between atoms in the structures of CO ₂ -bound holo and apo HCA II 83
5-1	Data collection and refinement statistics for the Lys170 variant structures of HCA II..... 100
5-2	Apparent values of pK _a and maximal rate constants for kinetic measurements of catalysis by wild type and site-specific mutants of HCA II at residue 170 obtained by ¹⁸ O exchange at 25 °C. ^a 101
5-3	Values of the pK _a for the zinc-bound water and the maximal value of k_{cat}/K_M for the catalysis of the hydration of 4-nitrophenylacetate by variants of HCA II at 25 °C..... 101
6-1	Data processing and refinement statistics for the structures of the Cam mutants..... 112

LIST OF FIGURES

<u>Figure</u>		<u>page</u>
1-1	The dismutation of superoxide as catalyzed by human MnSOD, monitored spectroscopically at 250 nm	29
1-2	The four known classes of superoxide dismutase share very little structural similarity	30
1-3	A stereoview of the active site of human MnSOD illustrates the amino acid and solvent hydrogen bonded network.....	31
1-4	The tetrameric structure of human manganese superoxide dismutase contains 2 two-fold axes of symmetry.....	31
1-5	The structures of three classes of carbonic anhydrase show that, despite catalyzing the same reaction, there is a large divergence in structure	32
1-6	A stereoview of the active site of human CA II showing the hydrophilic side of the active site cavity	33
2-1	The active site structure of wild-type human manganese superoxide dismutase shows an intricate interaction network.....	49
2-2	The pH profile for molar absorptivity at 480 nm for hMn ³⁺ SOD, wild-type and mutants.....	49
2-3	Change in absorbance at 420 and 480 nm over a 0.25 ms time scale after generation of superoxide by pulse radiolysis in a solution containing E162D human MnSOD.....	50
2-4	Normalized transitions for E162D (A), wild-type (B), and E162A (C) human MnSOD as determined by differential scanning calorimetry	51
2-5	Structures of the dimeric interface of wild-type (top), E162D (middle), and E162A (bottom) human MnSOD.....	52
3-1	Superposition of the active sites of human (magenta) (Hearn <i>et al.</i> , 2003) and <i>E. coli</i> MnSOD (green) (Borgstahl <i>et al.</i> , 2000) shows the high degree of similarity in the active site	67
3-2	Output from pulse radiolysis studies shows the decrease in absorbance at 260 nm over the course of the reaction demonstrating the zero-order phase of catalysis seen in F66A and wild-type human MnSOD	67
3-3	The pH dependence of k_4 in catalysis by F66A human MnSOD.....	68

3-4	Spectroscopic evidence of the formation of an inhibited complex in wild-type human MnSOD.....	68
3-5	The effects of mutations at Phe66 in human MnSOD are clearly visible at position 119 when compared to wild-type (magenta) (Hearn <i>et al.</i> , 2003).....	69
3-6	A stereoscopic view of the active site environment of human MnSOD and its mutants F66A and F66L.....	69
3-7	A diagrammatic representation of the geometry of the active site of the MnSODs with the distances presented in Table 3-3 defined with dashed lines..	70
3-8	A histogram showing the normalized B-factors of the atoms located in the active site of MnSOD.....	70
4-1	The active site of human carbonic anhydrase II is located at the bottom of a conical cavity.....	84
4-2	The electron density for the carbon dioxide molecule in both holo (top) and apo (bottom) HCA II is clearly observed in the hydrophobic patch (green mesh and sticks).....	85
4-3	The non-catalytic carbon dioxide binding site was found in a hydrophobic patch (magenta surface) on the side of the enzyme opposite the hydrophobic patch.....	86
4-4	Two glycerol molecules were found in the structures of CO ₂ -bound holo and apo HCA II.....	86
4-5	A superposition of the CO ₂ -bound holo HCA II structure with that of V143Y HCA II (Alexander <i>et al.</i> , 1991) clearly shows that the side chain of Tyr143 (white sticks) would directly interfere with CO ₂ binding (cyan sticks).....	87
4-6	The catalytic mechanism of CO ₂ hydration as catalyzed by HCA II, as proposed by Lindskog (1983).....	88
4-7	The structure of bicarbonate-bound T200H HCA II reveals that the binding site of CO ₂ observed in this study is the catalytic site.....	89
5-1	The protein environment around the proton shuttle residue His64 includes residues Trp5 and Lys170.....	101
5-2	A surface representation of HCA II shows the location of Lys170 relative to the active site core.....	102
5-3	The pH dependence of k_{cat}/K_M is apparently unchanged in the four Lys170 mutants.....	102

5-4	Mutation of Lys170 results in a change in the rate and pH dependence of the proton transfer controlled value of $R_{H_2O}/[E]$	103
5-5	The electron density corresponding to His3 is visible in all four Lys170 HCA II mutants, although to varying degrees.....	103
5-6	The location of His3 in all four mutants is roughly the same, apparently pi-stacking with the side chain of Trp5.....	104
5-7	A novel interaction is observed between residues 64 and 170 in the structure of K170D HCA II.....	104
6-1	An alignment of Cam (from <i>M. thermophila</i>) and CamH (from <i>M. acetivorans</i>) shows the lack of the acidic loop (black box) in CamH.....	113
6-2	The trimeric organization of Cam yields three active sites per enzyme, each at a monomer-monomer interface	114
6-3	The structure of a Cam monomer shows a left-handed β -helix topology with several N-terminal (blue) surface loops and a C-terminal (red) α -helix.....	115
6-4	The 63-64-65 loop in the mutants of Cam occupies a different conformation then that observed in all reported Cam structures.....	115
6-5	The electron density for the 62-63-64 loop clearly defines its orientation in the structure of W19N Cam	116

LIST OF ABBREVIATIONS

Å	Angstrom
atm	atmosphere (unit of pressure)
BH ⁺	protonated base
C ^α	alpha carbon
CA	carbonic anhydrase
Cam	<i>Methanosarcina thermophila</i> γ-class carbonic anhydrase
CamH	<i>M. acetivorans</i> γ-class carbonic anhydrase
CAPS	N-cyclohexyl-3-aminopropanesulfonic acid
CNS	Crystallography and NMR System
CO ₂	carbon dioxide
CTD	C-terminal domain
Cu	copper
ΔC _p	change in heat capacity
DNA	deoxyribonucleic acid
DSC	differential scanning calorimetry
E	enzyme
<i>E. coli</i>	<i>Escherichia coli</i>
EDTA	ethylenediaminetetraacetic acid
ETC	electron transport chain
Fe	iron
GPI	glycosylphosphatidylinositol
H ⁺	proton / hydrogen ion
H ₂ O ₂	hydrogen peroxide
HCA	human carbonic anhydrase

HCO_3^-	bicarbonate ion
IPTG	isopropyl- β -D-thiogalactopyranoside
k	rate constant
kcal	kilocalorie
k_{cat}	turnover number
k_{cat}/K_M	specificity constant
K_D	dissociation constant
kDa	kilodalton
kV	kilovolt
LB	lysogeny broth
M	molar
MES	2-(4-morpholino)-ethane sulfonic acid
Mn	manganese
MOPS	3-(N-morpholino)-propanesulfonic acid
μM	micromolar
mA	milliampere
mM	millimolar
mm	millimeter
mol	mole
NCO^-	thiocyanate ion
Ni	nickel
NTD	N-terminal domain
nm	nanometer
O_2	dioxygen
O_2^-	superoxide ion

O_2^{2-}	superoxide dianion
OD	optical density
OH^-	hydroxide ion
PDB	Protein Data Bank
pH	negative log of proton concentration
pK_a	acid dissociation constant
PSR	proton shuttle residue
rmsd	root mean square deviation
ROS	reactive oxygen species
RT	room temperature
SDS-PAGE	sodium dodecyl sulfate polyacrylamide gel electrophoresis
SOD	superoxide dismutase
TAPS	N-tris(hydroxymethyl)methyl-3-aminopropanesulfonic acid
TM	transmembrane
Tris	tris(hydroxymethyl)aminomethane
Zn	zinc

Abstract of Dissertation Presented to the Graduate School
of the University of Florida in Partial Fulfillment of the
Requirements for the Degree of Doctor of Philosophy

STRUCTURAL STUDIES OF THE CATALYTIC MECHANISMS OF TWO SUPERFAST
METALLOENZYMES: CARBONIC ANHYDRASES AND MANGANESE SUPEROXIDE
DISMUTASES

By

John Francis Domsic

December 2009

Chair: Robert McKenna

Cochair: David Silverman

Major: Medical Sciences – Biochemistry and Molecular Biology

The utilization of metals in biological enzymes is ubiquitous in the diverse kingdoms of life. These metals, on their own are inactive, but when incorporated into a protein allow for the enhancement a myriad of chemical reactions. To understand how an enzyme functions it is necessary to gain detailed knowledge of its active site structure and how this correlates to catalytic efficiency. Additionally, a knowledge of the interactions between enzyme and substrates and products aids in the elucidation of catalytic pathways.

The manganese superoxide dismutases (MnSOD) neutralize naturally occurring toxic superoxide radicals. Mutational analysis of human MnSOD demonstrated that Glu162, a second-shell ligand of the Mn ion is necessary for efficient activity, due to tuning of the Mn. Additionally, the eukaryotic MnSODs are typically more product-inhibited than their prokaryotic counterparts. Alteration of the active site mouth in human MnSOD resulted in a weakly product-inhibited form.

The carbonic anhydrases (CAs) are a family of structurally diverse enzymes that catalyze the reversible hydration of carbon dioxide to bicarbonate and a proton. Due to

the high turnover rate, an understanding of enzyme-substrate interactions has been elusive. The use of a high-pressure environment allowed for successful capture of carbon dioxide in the hydrophobic pocket in the active site of human CA II. The x-ray crystal structure of both zinc-bound and zinc-free HCA II revealed that the active site remains relatively static, acting as a solvation site for CO₂, thus allowing for rapid turnover.

A proton transfer step is also required in the catalytic cycle of CA to allow for the regeneration of the active zinc-bound hydroxide. This is accomplished by proton transfer along a solvent-mediated proton wire, leading to the final proton acceptor. Mutational analysis of the environment surrounding the proton shuttle residue, His64, in HCA II revealed that the enzyme finely tunes this region to allow for bidirectional proton transfer under physiological conditions. Mutational analysis of a γ -CA revealed that residues located adjacent to the active site affect the proton transfer properties in this enzyme. These data suggest that one must carefully consider residues outside the active site environment when analyzing the catalytic activity of an enzyme.

CHAPTER 1 INTRODUCTION

Metalloproteins

From the calcium ions required for calmodulin, to the zinc ion in zinc-finger-containing transcription factors, to the iron ion in the iron-sulfur clusters of plant photosystems, metal ions are vital cofactors for the functions a myriad of proteins. The roles of metal ions in biological macromolecules are as varied as the functions of these molecules. Functions of metals include a role as conformational regulators that allow proteins, such as zinc-finger transcription factors (zinc) and calmodulin (calcium), to fold and function properly. (Coleman, 1992; Chin & Means, 2000). The enzymatic functions of metals (metalloenzymes) involves a modulation of the local environment to favor more efficient reaction conditions. One example is the formation of a redox-active catalytic site as occurs in the superoxide dismutases. Another example is the modulation of the pK_a of a metal-bound ligand, such as a solvent molecule, as is present in the carbonic anhydrases.

Additionally, the protein itself can finely tune the metal to assist in the formation of a catalytically efficient active site. These effects can be both short- and long range. Short-range interactions involve the direct coordination of the metal ion by amino acid side chains and ligands and the subsequent configuration of additional coordination sites. Long-range interactions are involved in finely tuning the environment surrounding the metal ion, thus modulating the kinetic properties of the enzyme. This work will focus on the effects of the protein on modulating the activity of two metalloenzymes, human manganese superoxide dismutase and human carbonic anhydrase II.

Superoxide Dismutases

The Superoxide Radical

The formation of superoxide occurs during cellular respiration in the electron transport chain (ETC) of the mitochondria. Complexes I and III of the ETC have been implicated as the major producers of superoxide due to a lack of efficiency in the transfer of electrons from two-electron carriers to one-electron carriers (St-Pierre *et al.*, 2002). The occasional leakage of the extra electron can result in the one electron reduction of molecular oxygen, thus forming the superoxide radical. This can further reduce to hydrogen peroxide or a hydroxyl radical. Superoxide cannot combine, spontaneously, with other non-radical molecules due to spin restriction. However, it does have the ability to interact with other radicals. Interaction with nitric oxide forms peroxynitrite, which can, in turn, cause lipid peroxidation and tyrosine nitration. Superoxide can also cause the release of iron from sources such as the iron-binding protein ferritin. The resulting elevated iron levels can result in interactions with hydrogen peroxide to produce hydroxyl radicals via the Fenton reaction (McCord, 2002). Ultimately hydroxyl radicals cause the formation of DNA lesions occurs due to 8-oxoguanine and thymine glycol dimers, lipid peroxidation, and protein damage due to backbone breakage and the formation of non-canonical amino acid side chains (for a review see Davies, 2005). This oxidative stress caused by the formation of reactive oxygen species (ROS) is the cornerstone for the free radical theory of aging (Harman, 1956). This theory suggests that the accumulation of cellular abnormalities due to oxidative stress leads to a decline in cell processes and ultimately to cell death.

Superoxide Dismutases

The neutralization of superoxide is therefore necessary for the survival of cells that respire aerobically. This is accomplished by the superoxide dismutases (SODs), a family of enzymes (EC 1.15.1.1) of which there are four classes that are categorized based on the metal(s) in the active site: copper/zinc (Cu/Zn), iron (Fe), manganese (Mn), and nickel (Ni). Cu/ZnSOD utilizes a two metal active site, with the copper ion being the catalytic metal. This class can be found in both prokaryotic organisms and eukaryotic organisms, from plants to mammals (Fink & Scandalios, 2002). The iron and manganese enzymes share very similar properties structurally and, indeed, several cambialistic enzymes have been discovered that are active with iron or manganese active site ions (Sugio *et al.*, 2000; Chen *et al.*, 2002). The iron enzymes are found mainly in prokaryotes and the chloroplasts of plants (Muñoz *et al.*, 2005). The manganese enzymes are found ubiquitously in nature and occur as a mitochondrially-targeted enzyme in eukaryotes (human *SOD2*, for example). NiSOD is the most recently discovered of these classes with existence confirmed in *Streptomyces* (Youn *et al.*, 1996; Youn *et al.*, 1996b; Barondeau *et al.*, 2004) and a strain of cyanobacteria (Palenik *et al.*, 2003).

The physiological importance of the reaction catalyzed by the SODs is underscored by the presence of multiple classes within the same organism. For example, *Escherichia coli* is known to express both an iron and a manganese SOD. Also, there are three human SODs, a cytosolic Cu/ZnSOD, an extracellular Cu/ZnSOD, and the mitochondrial MnSOD. Members of the Cu/Zn, Fe, and Mn SODs have been found in various plant species, though a given species doesn't necessarily contain all three (Gupta *et al.*, 1993).

Phenotypes of SOD deficiency

The necessity of the various forms of SODs has also been demonstrated by numerous studies on SOD deficient models. Phillips *et al.* (1989) demonstrated that a mutational defect in Cu/ZnSOD in *Drosophila* leads to a drastic decrease in longevity and fertility and sensitivity to increased levels of superoxide. Superoxide sensitivity and increased rates of mutagenesis were observed in Cu/ZnSOD-deficient yeast and, interestingly, normal function was rescued by the introduction of a bacterial MnSOD (Bowler *et al.*, 1990). In mice with defective Cu/ZnSOD, a reproductive deficiency was observed (Reaume *et al.*, 1996). Probably the most well documented disease state associated with SOD is familial amyotrophic lateral sclerosis, otherwise known as Lou Gehrig's Disease (Noor *et al.*, 2002; Strange *et al.*, 2007). This disease is associated with defects in Cu/Zn SOD (*SOD1*) that can cause both aggregation of misfolded protein and increase in the rate of production of hydroxyl radical, depending on the mutation(s) present.

Deficiencies in the manganese form of SOD have also been phenotypically characterized. SOD double-knockouts (Fe and Mn) in *E. coli* demonstrated an increased sensitivity to superoxide as well as an increase in the rate of spontaneous mutagenesis and an oxygen-dependent decrease in growth rate (Farr *et al.*, 1986). In a very extreme case, mice lacking any MnSOD had a life span of 1-2 weeks as a result of faulty mitochondrial activity (Lebovitz *et al.*, 1996; Li *et al.*, 1995). Disease states that propagate in the human population are not usually associated with a completely inactive enzyme, as one would expect a lack of MnSOD would lead to rapid oxidative damage and organism death. Rather, the most analyzed polymorphism results in the amino acid substitution V16A, located in the mitochondrial targeting peptide at the N-terminus of the

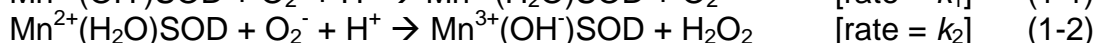
immature protein. This sequence is recognized by transporters on the mitochondria that uptake the protein, followed by cleavage of the signal peptide. Thus, a mutation in the signal peptide results in a decreased level of targeting and, therefore, mitochondrial MnSOD, although the mature form of the enzyme has normal activity. This inadequate targeting has been suggested to cause an increased risk of nephropathy and retinopathy in certain diabetic patients (Möllsten *et al.*, 2007; Hovnik *et al.*, 2009). Also this polymorphism is associated with an increased risk of Parkinson's disease (Farin *et al.*, 2001).

Catalytic mechanism

Even though there are differences in the catalytic metal, all families of SOD catalyze the disproportionation of two superoxide molecules to form hydrogen peroxide (H_2O_2) and dioxygen (O_2). The detailed mechanism discussed here is specific to the MnSODs in its pathways, although all SODs share the general mechanism, the difference being the oxidation state of the metal and the occurrence of a product-inhibited state. During the catalytic process, the active site metal cycles between an oxidized and reduced state. The catalytic cycle begins when superoxide binds at an unoccupied, 6th coordination site on the Mn. The first step of catalysis is a first-order reaction with respect to superoxide (Figure 1-1). In this step, one molecule of superoxide is oxidized to dioxygen with a concurrent reduction of the manganese and the protonation of the manganese-bound hydroxide (eq 1-1).

There are two possible routes during the second step of catalysis by MnSOD. The first involves the uninhibited formation of H_2O_2 from one molecule of superoxide and two protons (one from Mn-bound water and one from bulk buffer) as well as the concurrent oxidation of the manganese (eq 1-2). The second possibility involves a zero-order

decay that has been attributed to the presence of a reversibly product-inhibited form of the enzyme (Figure 1-1). This is believed to involve the formation of a peroxide dianion in complex with oxidized manganese (eq 1-3). Once the product-inhibited state is released the catalytic cycle can complete (eq 1-4). This results in the formation of H₂O₂ and a return of the enzyme to its initial state, a manganese-bound hydroxide and the oxidized manganese.



The hydrogen peroxide is then obviated directly by enzymes such as glutathione peroxidase, peroxiredoxin, and catalase (Smith *et al.*, 2003).

Structural descriptions

Despite the similarities in the catalytic mechanisms across the SOD families, the structural features of the various forms of SODs generally vary greatly between families (Figure 1-2). The subunit organization of all known iron (Figure 1-1 A) and manganese SODs consists of a homodimer with several eukaryotic forms including the human manganese enzyme, further organized into a dimer of dimers (Figure 1-1 B). The nickel enzyme exists as a hexamer of monomers, which are structurally distinct from the other forms (Figure 1-1 C). The Cu/Zn SODs also exist as dimers but have a different monomeric structure than the iron and manganese SODs (Figure 1-1 D) (Strange *et al.*, 2007). The general topology of all iron and manganese SOD monomers and dimers is virtually the same, and the majority of this work will focus on the human mitochondrial MnSOD unless otherwise stated.

The human MnSOD monomer can be divided into two domains: the N-terminal domain (NTD) (residues 1-83) made up of α helices, and the C-terminal domain (CTD) (residues 84-198) consisting of a mixed α/β motif. The active site metal ion is sandwiched between these two domains and is coordinated by two histidines from the NTD (His26 and His74) and by an aspartate and histidine from the CTD (Asp159 and His163). A fifth coordination site of the Mn is occupied by a solvent molecule, either a hydroxide or water depending on the oxidation state of the manganese, thus completing a trigonal bipyramidal complex with the manganese (Figure 1-3). The active site may be further extended by considering the presence of an extensive hydrogen-bonded network that may be utilized as a proton transfer pathway during the second stage of catalysis. Two monomers are organized to form the dimeric interface that is required for efficient catalytic activity in all known MnSODs (Figure 1-4). In the tetrameric MnSODs, two of these dimers are required to form the physiological tetramer.

Carbonic Anhydrase

As was mentioned at the beginning of this chapter, another role for metals in catalysis is altering the acid/base properties of metal-bound ligands. One such class of enzymes that utilize this is the carbonic anhydrases (CA) (EC 4.2.1.1), which catalyze the reversible hydration of carbon dioxide to form bicarbonate and a proton. There are five known classes of CAs, categorized based on their overall fold and their amino acid sequence: α , β , γ , δ , and ζ . The latter two classes were relatively recently discovered and have only been found in a few organisms. The δ -class is found in diatoms and the lone member of the ζ -class is the only known cadmium-containing enzyme and was discovered in *Thalassiosira weissflogii* (Roberts *et al.*, 1997; So *et al.*, 2004; Lane *et al.*, 2005). There was at one point an ϵ -class CA, discovered in the carboxysomal shell of

cyanobacteria. However, structural analysis revealed it to be a gene-duplicated β -CA with one of the two domains having diverged to the point that sequence analysis no longer recognized it as a β -CA domain (Sawaya *et al.*, 2006). The α -CAs are generally mammalian enzymes, but have also been discovered in mosquitoes and green algae (Corena *et al.*, 2002; Karlsson *et al.*, 1995). The β -CAs are plant, bacterial, and fungal enzymes (Elleuche & Pöggeler, 2009). The γ -CAs have been found in archaea and plants (Alber & Ferry, 1994; Sunderhaus *et al.*, 2006).

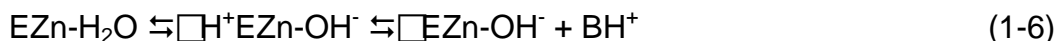
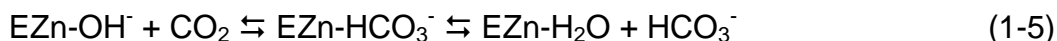
α , β , and γ Carbonic Anhydrases

Of the five known classes, only three, α , β , and γ , have been studied extensively. Structures of at least two representatives of each of these classes have been solved by x-ray crystallography with an even larger number having been characterized kinetically. Zinc has been implicated as the metal of choice for these enzymes, though a recent study suggests that, when in an anaerobic environment, the γ -CAs utilize iron as the active site metal.

Catalytic mechanism

The catalytic mechanism of the α -CAs has been the most extensively studied of all the CAs. This mechanism is believed to be similar in the β -CAs and quite possibly the γ -CAs, although the mechanics are slightly different (Rowlett, 2009; Ferry, 2009). As was shown with the superoxide dismutases, catalysis by the CAs involves a two-step mechanism. In the first step carbon dioxide binds to the active site and the zinc-bound hydroxide nucleophilically attacks the carbon of the CO_2 molecule, thus forming HCO_3^- (eq 1-5). A water molecule then diffuses freely into the active site, displaces the bicarbonate, and coordinates with the zinc. The zinc-bound water is catalytically inactive, and therefore a hydroxide must be generated by proton removal. This occurs

during the second step of catalysis in which a solvent-mediated proton wire transfers a proton from the zinc-bound water to the proton acceptor, amino acid His64 (eq 1-6) (Figure 1-6). This proton transfer is the rate-limiting step of catalysis, occurring at 10^6 s^{-1} (Silverman & Lindskog, 1988).



Structure

Despite catalyzing the same general reaction, there is an astounding lack of structural identity, thus providing an excellent example of convergent evolution. The α -class enzymes all share the same general structure: a catalytic core of a 10 strand, anti-parallel, twisted β sheet, with a total of 7 α helices located at the enzyme's surface (Figure 1-5 A). The catalytic site is located in an active site cavity that is directly accessible from the surface. At the bottom of this cavity, situated on the β sheet, is the zinc ion. The zinc is covered by two flaps (residues 1-26 and 196-207) and is directly coordinated by three histidines (HCA II numbering His94, His96, and His119) and a solvent molecule (H_2O or OH^-).

The β -CAs display the greatest intra-class structural dissimilarities, with a high degree of oligomeric heterogeneity across this family, with physiological molecular weight ranging from 45-200 kDa. The level of oligomerization is most likely a result of surface structure variation, with the functionally active moiety being a dimer, and all known β CA structures having a number of monomers equal to 2^n , where n is 1, 2, or 3 (Figure 1-5 B). Also, *Porphyridium purpureum* CA exists as pseudo-dimer in which there appears to have been a gene duplication event leading to a functional monomer with two nearly identical domains (Mitsuhashi *et al.*, 2000). There have been two

subclasses identified based on metal coordination (Rowlett, 2009). In type I enzymes, the zinc is coordinated by one histidine and two cysteines, with a fourth coordination site occupied either by a solvent molecule. In type II enzymes, the zinc is also coordinated by one histidine and two cysteines, with the fourth coordination site occupied by an aspartate. The zinc-coordinating amino acids are located all within one monomer, with additional active site residues contributed by the neighboring monomer.

The structural organization of the γ -CAs is also oligomeric with the physiological unit existing as a trimer with three active sites, each sandwiched at the three interfaces (Figure 1-5 C). The monomer exhibits an overall left-handed β -helix topology (21 β -strands) with several intervening loops and a C-terminal helix that runs along base of the trigonal prism formed by the β -helix. The intervening loops occur at three points in the β -helix towards the N-terminus of the protein. All three loops exist on the face opposite of the interfacial sides of the β -helix core. Three histidines and a solvent molecule, in a fashion similar to the α -CAs, coordinate the active site metal. When synthesized aerobically in *E. coli*, the γ -CA from *Methanosarcina thermophila* (Cam) contains zinc in its active site (Alber *et al.*, 1999). However, it has been demonstrated that Cam contains iron in its active site when synthesized in an archaeal expression system anaerobically (Macauley *et al.*, 2009). The structure of another γ -CA, from *Pyrococcus horikoshii*, reveals an identical fold, with the exception that one of the loops is absent (Jeyakanthan *et al.*, 2008).

The most widely studied of the CA families is by far the mammalian α -class. In fact, the first carbonic anhydrase was an α -CA isolated as a carbon dioxide hydrating preparation from ox blood (Meldrum and Roughton, 1932). Since this initial discovery, a

plethora of studies have elucidated many physiological, catalytic, and structural properties of this enzyme.

α -class Isoforms

The human genome encodes 15 known CAs (I-XV), all of which belong to the α -class. Three of these isoforms, VII, X, and XI, are not capable of typical CA activity as they lack one of the zinc-binding histidine ligands. There is also an additional mammalian isoform, XV, which shows active expression in rats and mice, but has not been observed in humans (Hilvo *et al.*, 2005). The remaining human isoforms have all been characterized in terms of expression patterns (mRNA), while a large majority have also been characterized kinetically. Table 1-1 shows the localization, domain organization, and kinetic properties of all 14 human CAs.

Like the considerable variations in tissue distribution, the human CAs also have a wide range of functions. CAs are believed to supply bicarbonate for the initial steps of ureagenesis and gluconeogenesis (Henry, 1996). They have also been demonstrated to be important in acid/base balance, including gastric acid production and renal and male reproductive tract acidification (Breton, 2001). There is also accumulating evidence for a role of CA in regulating the function of ion transport by the sodium/bicarbonate transporter, possibly by direct interaction between the two proteins (Vince & Reithmeier, 1998; Becker & Deitmer, 2007).

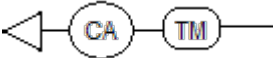
Carbonic Anhydrase Deficiencies

The variety of isoforms provides functional redundancy that allows for survival of organisms that may have a mutation leading to reduced or lost function of an isoform (Sly & Hu, 1995). For example, CA III, which makes up approximately 8% and 25% of the protein mass in skeletal muscle and adipocytes, respectively, can be knocked out in

mice without any noticeable effects on fitness or appearance (Kim *et al.*, 2004). Also, mutations in the gene encoding human CA I that have been shown to result in decreased or lost activity but do not cause any phenotypic differences (Venta, 2000). Presumably, human CA II (HCA II), which is also found in red blood cells, is able to make up for the loss of CA I, as CA II is a much more efficient enzyme. The importance of HCA II is highlighted by mutations that cause a loss of functional HCA II resulting in a disease aptly known as HCA II deficiency syndrome (Hu *et al.*, 1997). The symptoms of this disease are severe and illustrative of the myriad functions of HCA II. They include renal tubular acidosis, hearing impairment, mental retardation, facial dysmorphism, growth failure, increased bone density, and intracerebral calcification (Venta *et al.*, 1991; Borthwick *et al.*, 2003).

Table 1-1. The tissue specificities, structural topologies, and catalytic activities of the known α -class carbonic anhydrases. In the topology column, CA = CA domain, TM = transmembrane domain, and GPI = glycosylphosphatidylinositol lipid anchor. The domains shown as triangles are extracellular, circles are intracellular, and rounded squares are transmembrane segments.

Isozyme	Localization	Topology ^a	$\frac{k_{cat}}{K_M}$ ($M^{-1} s^{-1}$) _b	k_{cat} (s^{-1}) _b
I	erythrocytes, epithelium of large intestine, adipose tissue, sweat glands, corneal epithelium		5.0×10^7	2.0×10^5
II	virtually all tissue types		1.5×10^8	1.4×10^6
III	red skeletal muscle cells, adipocytes, several other tissues in low concentrations		3.0×10^5	1.0×10^4
IV	membrane-bound in lungs, kidneys, gastrointestinal tract		5.0×10^7	1.1×10^6
V	liver mitochondria		3.0×10^7	3.0×10^5
VI	saliva		1.6×10^7	7.0×10^4
VII	cytosolic		7.6×10^7	9.4×10^5

VIII	Purkinje cells	N/A	N/A	N/A
IX	membrane-bound, colorectal tumor cells		5.5×10^7	3.8×10^5
X	mRNA found in adult brain	N/A	N/A	N/A
XI	mRNA found in adult brain	N/A	N/A	N/A
XII	membrane-bound mRNA overexpressed in renal cell cancers		3.4×10^7	4.0×10^5
XIII	salivary glands, kidney, small intestine, colon, uterus, testis		active	active
XIV	membrane-bound in brain, heart, skeletal muscle, lung, liver		3.9	
XV	does not appear to be expressed in higher primates		active	active

a derived from (Purkerson & Schwartz, 2007); b from (Duda & McKenna, 2004)

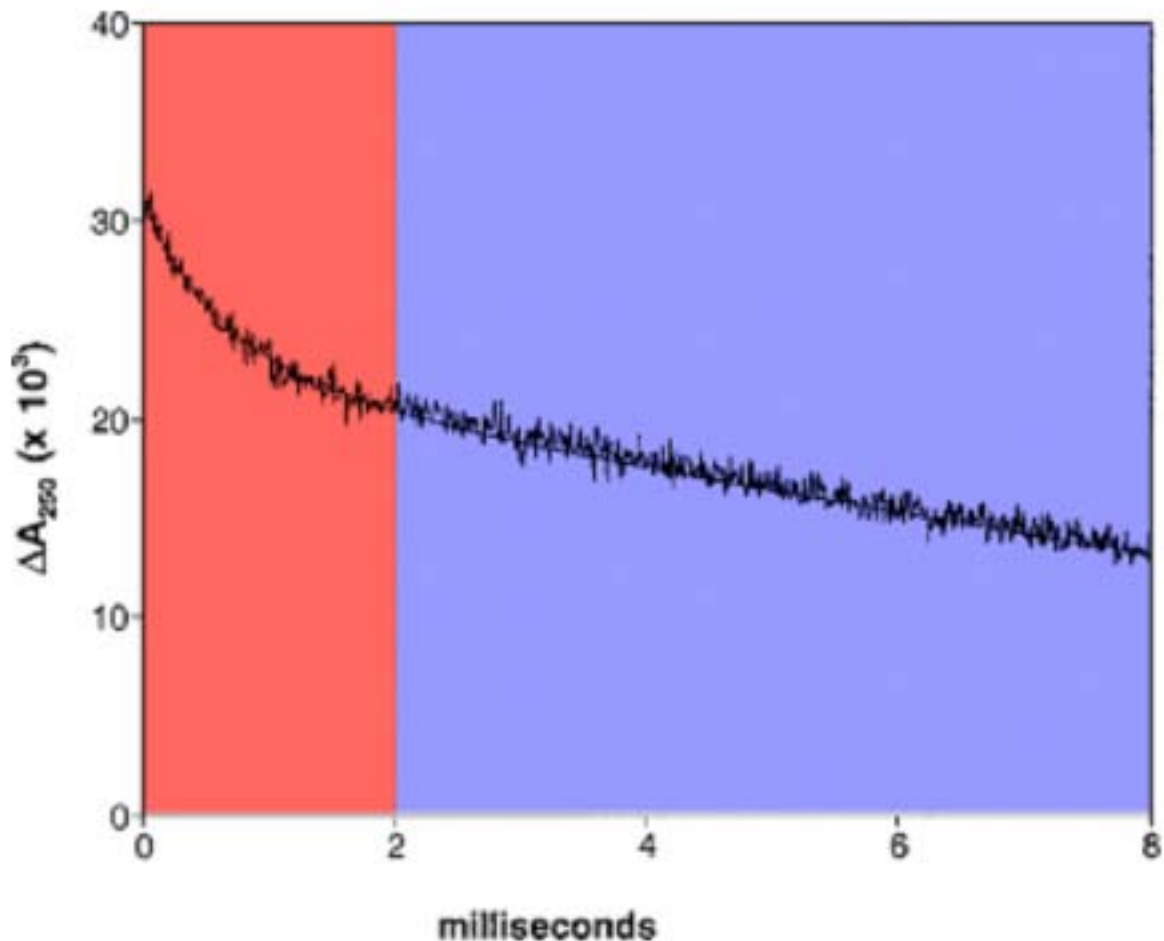


Figure 1-1. The dismutation of superoxide as catalyzed by human MnSOD, monitored spectroscopically at 250 nm. The red shaded area outlines the initial burst phase of first order conversion of superoxide to dioxygen. The blue shaded

area outlines the zero-order decay of superoxide that occurs when the enzyme enters a product-inhibited state. (derived from Hsu *et al.*, 1996).

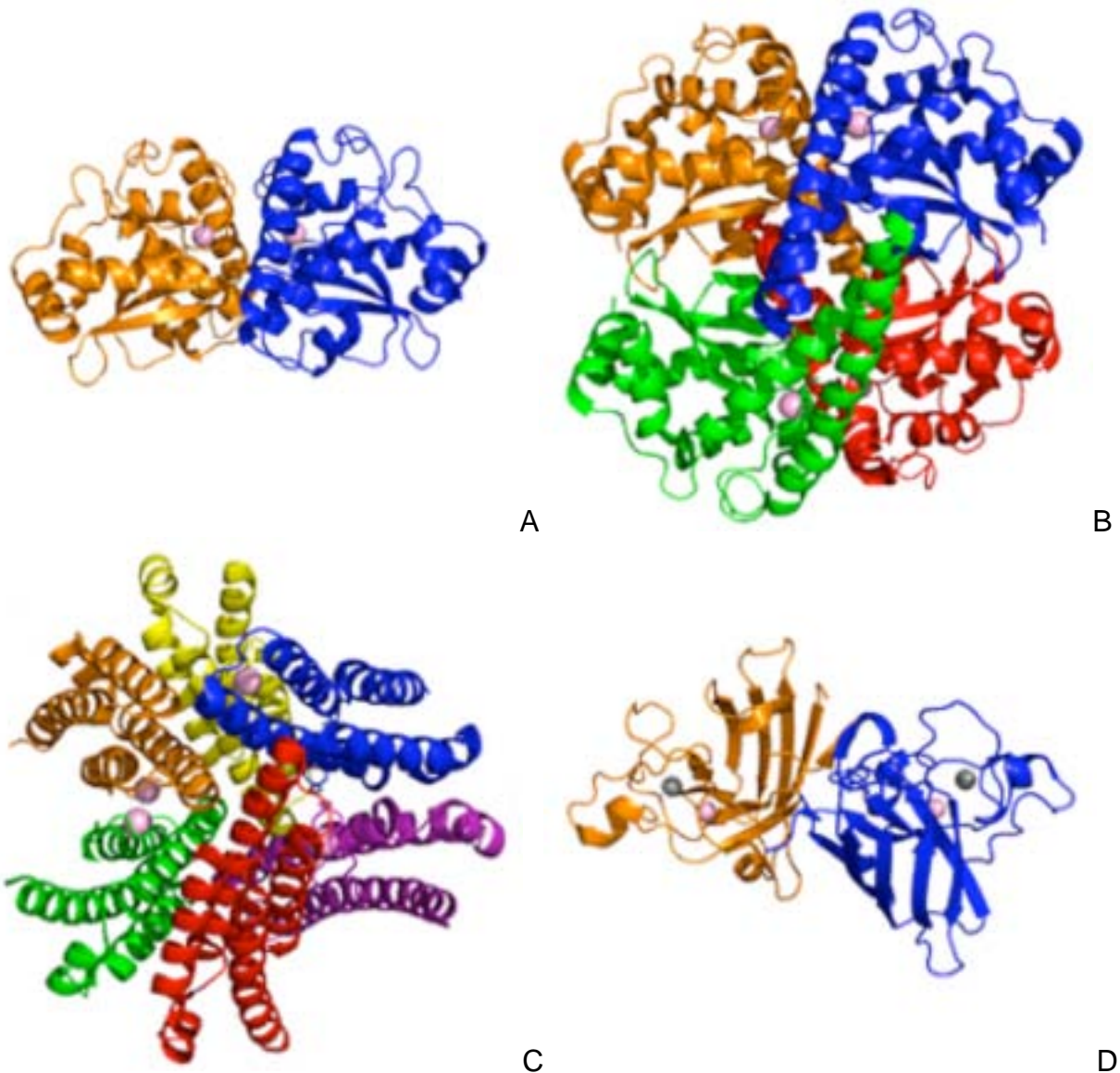


Figure 1-2. The four known classes of superoxide dismutase share very little structural similarity. The closest families, structurally, are the iron (A) and manganese (B) enzymes as shown here from *E. coli* (PDB ID 1isa, Lah *et al.*, 1995) and human (PDB ID 1luv, Hearn *et al.*, 2003) sources, respectively. Nickel SOD exists as a hexamer in *Streptomyces coelicolor* (PDB ID 1t6u, Barondeau *et al.*, 2004). Another human SOD is copper/zinc SOD, the structure of which is a dimer with a dimetallic active site (PDB ID 2v0a, Strange *et al.*, 2007).

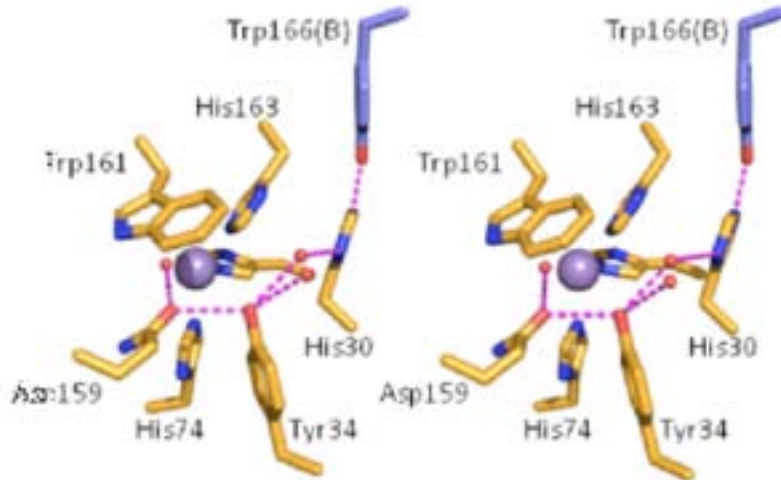


Figure 1-3. A stereoview of the active site of human MnSOD illustrates the amino acid and solvent hydrogen bonded network. The Mn is shown as a purple sphere, and dashed magenta lines represent distances that would allow for hydrogen bonding. The majority of the active site is made up of one monomer (orange) with some contribution from the neighboring monomer (blue).

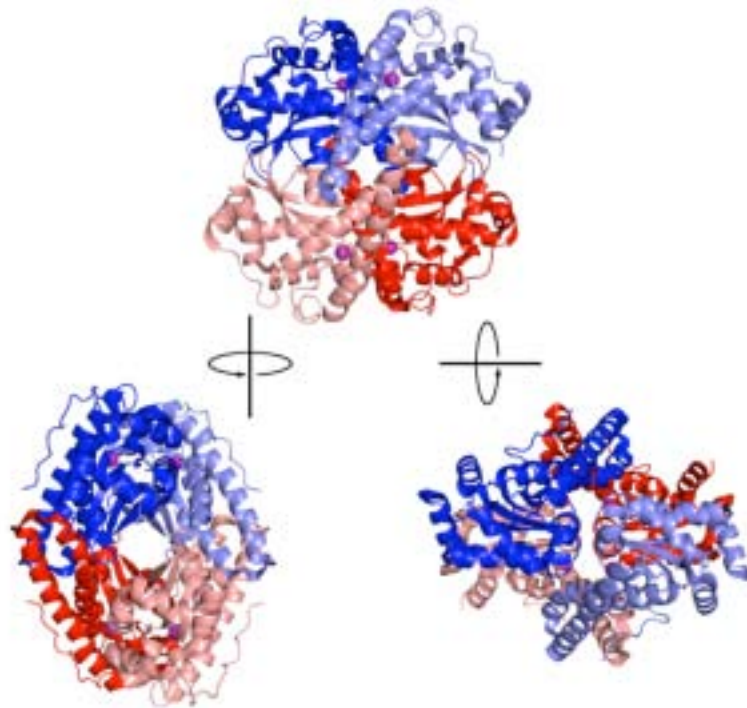


Figure 1-4. The tetrameric structure of human manganese superoxide dismutase contains 2 two-fold axes of symmetry. Each dimeric interface forms two active sites. The monomers that constitute each dimer are colored similarly in this figure (dark and light blue or red). The dimeric interface can be observed by viewing the protein along the x-axis (bottom right). The tetrameric interface, which is involved in protein stability, can be seen by viewing down the y-axis (bottom left).

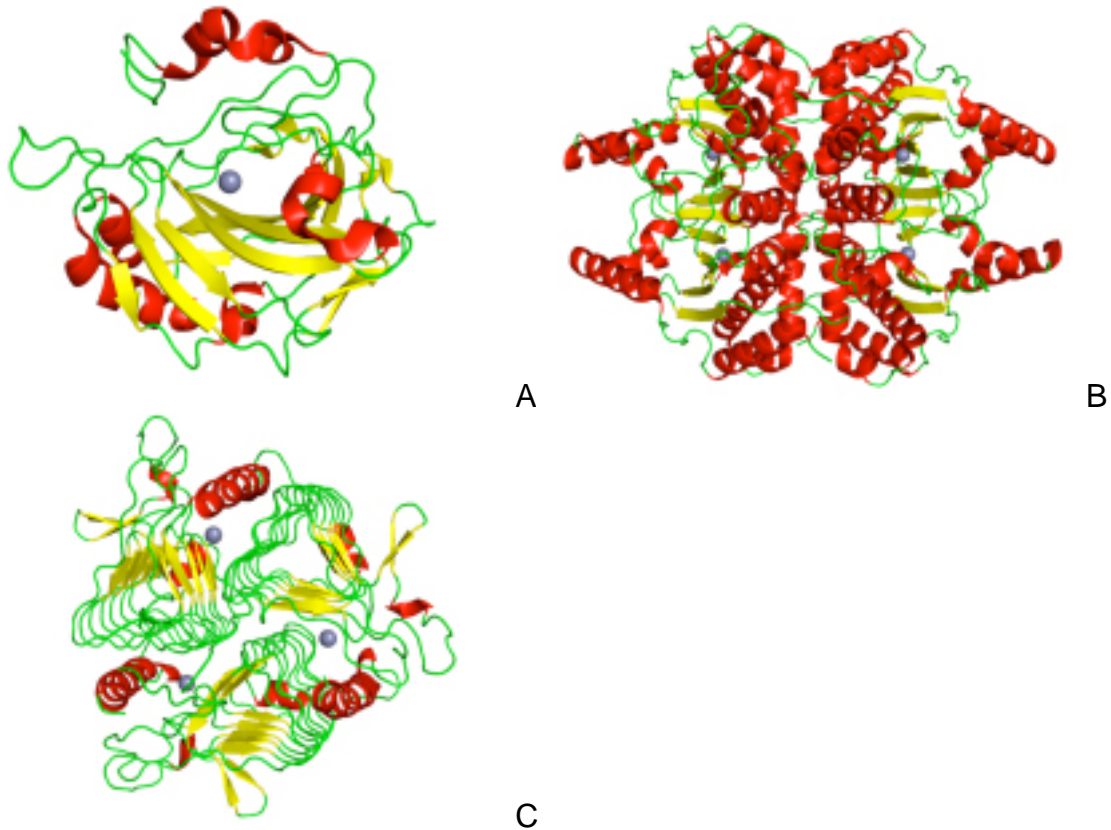


Figure 1-5. The structures of three classes of carbonic anhydrase show that, despite catalyzing the same reaction, there is a large divergence in structure. (A) The α -class enzyme, human CA II, represents the monomeric structure of most α -CAs (PDB ID 1tbt, Fisher *et al.*, 2005). (B) The β -CAs are all believed to be oligomeric with either 2, 4, or 8 monomers. Shown here is the tetrameric structure of *Porphyridium purpureum* CA (PDB ID 1ddz, Mitsuhashi *et al.*, 2000). (C) The γ -CAs are all trimeric enzymes with a central left-handed β helix core, as illustrated by the CA from *Methanosarcina thermophila* (PDB ID 1thj, Kisker *et al.*, 1996).

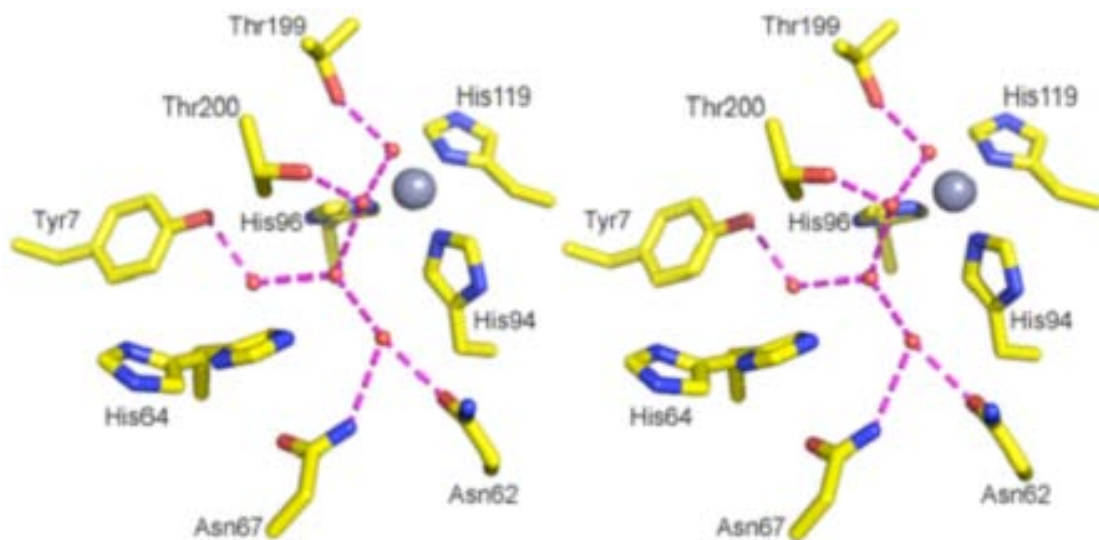


Figure 1-6. A stereoview of the active site of human CA II showing the hydrophilic side of the active site cavity. The residues in this half are responsible for forming the solvent-mediated proton network, shown here as magenta dashes. It is along this network that a proton is transferred during the second catalytic step. The proton accepting residue, His64, is shown in both its “in” and “out” conformations. (PDB ID 1tbt, Fisher *et al.*, 2005).

CHAPTER 2 THE ROLE OF THE DIMERIC INTERFACE IN CATALYSIS BY HUMAN MANGANESE SUPEROXIDE DISMUTASE

Introduction

As discussed in Chapter 1, the manganese superoxide dismutases (MnSOD) catalyze the disproportionation of superoxide to produce O_2 and H_2O_2 . The MnSODs are multimeric enzymes, with each monomer containing one active site manganese, coordinated by three histidines, an aspartate, and a solvent molecule. Human MnSOD is a mitochondrial enzyme that exists as a physiological tetramer, a dimer of dimers. The dimeric interface is quite conserved, structurally, between the eukaryotic and prokaryotic forms of the enzyme (Borgstahl *et al.*, 1992, Edwards *et al.*, 1998). The tetrameric interface, however, is unique to the eukaryotic forms of MnSOD and may act to stabilize the enzyme. Evidence for this is provided by thermal denaturation studies of human MnSOD and *Escherichia coli* MnSOD, a dimeric MnSOD. A major thermal unfolding transition occurs around 90 °C for human MnSOD, while that for *E. coli* MnSOD is around 76 °C (Mizuno *et al.*, 2004, Greenleaf *et al.*, 2004).

There have been several studies that have examined the catalytic and structural role of dimeric and tetrameric interface residues in human MnSOD. In the I58T tetrameric interfacial mutant of human MnSOD, it was found that the enzyme predominantly existed in the dimeric form and had a greatly reduced major unfolding temperature of 76 °C, identical to that of *E. coli* MnSOD (Borgstahl *et al.*, 1996). Also, there was only a slight reduction in the catalytic activity of the enzyme. Mutational analysis of a dimeric interfacial residue, Tyr166, revealed that the Y166F variant exhibited two major defects: a major unfolding temperature of 74 °C and a 40-fold reduction of activity (Hearn *et al.*, 2004). The loss of activity can be attributed to the role

of this residue in forming the putative proton transfer wire. An NMR study utilizing hydrogen-deuterium exchange showed that in wild-type human MnSOD the tetrameric interface was more dynamic than the dimeric interface (Quint *et al.*, 2006). Taken together these results support the hypothesis that the dimeric interface is vital for catalysis and overall stability, while the tetrameric interface only acts to slightly increase the stability of the enzyme.

To further investigate the function of the dimeric interface, the role of a glutamate residue, Glu162, was examined. Glu162 spans the dimeric interface and forms a hydrogen bond with one of the manganese coordinating histidines, His163, in a neighboring monomer (Figure 2-1) (Quint *et al.*, 2008). The importance of this interaction is highlighted by its conservation in all MnSODs, such as that from *E. coli*. The mutation E170A in *E. coli* MnSOD resulted in an enzyme that more readily dissociated into monomers and, intriguingly, preferentially bound to iron instead of manganese, thus nullifying enzymatic activity (Whittaker & Whittaker, 1998). This chapter will examine the corresponding mutation in human MnSOD, E162A, as well as a more conservative mutation, E162D. Despite the conservation of this glutamic acid in all MnSODs, the mutations did not exhibit all of the effects seen in the *E. coli* E170A mutant. The mutant human enzymes showed no appreciable change in metal specificity or stability. However, major changes in catalytic efficiency were observed, with both mutants being catalytically deficient.

Materials and Methods

Enzymes

The gene encoding the wild-type human MnSOD gene was contained in the vector pTrc99A. Mutations were made using the QuikChange Site-Directed

Mutagenesis kit from Stratagene (La Jolla, CA). Thermocycling was performed using oligonucleotides containing the desired mutation as primers. The presence of the mutation was verified by DNA sequencing (ICBR, University of Florida). The plasmid containing the mutated gene was then transformed into QC774 strain of *E. coli* that lacks the genes that encode endogenous FeSOD (*SodB*) and MnSOD (*SodA*) (Carlioz and Touati, 1986).

Cells were grown in LB broth supplemented with 6 mM MnCl_2 and ampicillin for antibiotic selection. Cultures were grown to OD_{580} of 0.8 and then induced with IPTG at 1 mM final concentration for 4 hours. Cells were then harvested via centrifugation and frozen at $-20\text{ }^\circ\text{C}$. Lysis was carried out using hen egg white lysozyme in 20 mM Tris, pH 8.2, 10% glycerol, and 1 mM EDTA. Following lysis, the suspension was heated to $60\text{ }^\circ\text{C}$ for 20 minutes to remove the majority of contaminating proteins. The lysate was then centrifuged at $30000\text{ }xg$ for 30 minutes. Prior to further purification, the supernatant was dialyzed against three exchanges of 20 mM Tris, pH 8.2. Q-sepharose HP (GE Healthcare) was used for ion exchange with elution by a 20% gradient of 500 mM sodium chloride. Purity was assessed via SDS-PAGE analysis and final concentrations were determined using UV spectrometry at 280 nm with $\epsilon_{280} = 40500\text{ M}^{-1}\text{ cm}^{-1}$ (Greenleaf *et al.*, 2004).

Visible Absorption

The visible spectrum of human MnSOD exhibits a broad absorption, with a maximum at 480 nm ($\epsilon_{480} = 610\text{ M}^{-1}\text{ cm}^{-1}$) (Leveque *et al.*, 2001). Enzyme samples were diluted 1:1 (final enzyme concentration $\sim 500\text{ }\mu\text{M}$) in a buffer composed of 200 mM MES and 200 mM TAPS, with the pH adjusted by potassium hydroxide and the absorbance at 480 nm was recorded as a function of pH.

Pulse Radiolysis

Pulse radiolysis experiments were performed by Dr. Diane E. Cabelli at Brookhaven National Laboratory using the 2 MeV van de Graaff accelerator to instantaneously produce superoxide in solution. The formation of superoxide radicals is driven by the exposure of air-saturated solution to the high-dose electron pulse according to the methods of Schwarz (Schwartz, 1981). This results in the production of superoxide at final concentrations in the range of 45 μM . Enzyme solutions were made in 2mM buffer (MOPS at pH 6.5-8.0, TAPS at pH 8.0-9.0, or CAPS at pH 9.0-10.0), 50 μM EDTA, and 30 mM formate (a hydroxyl radical scavenger). Reactions were monitored using a Cary 210 spectrophotometer at 25 °C, by following changes in either the absorbance of superoxide ($\epsilon_{260} = 2000 \text{ M}^{-1} \text{ cm}^{-1}$) (Rabani *et al.*, 1969) or the absorbance of the enzyme (Cabelli *et al.*, 1999).

Determination of Manganese and Iron Content

Manganese concentrations for the enzymes were determined by Patrick Quint in Dr. David Silverman's lab using a Perkin-Elmer 308 flame atomic absorption spectrometer fitted with a multi-ion lamp and a 3-slit burner and the absorption at 279 nm was monitored. The typical occupancies for manganese content ranged from 54-90%, depending on the mutation. Iron content was measured by ABC Research Corp. (Gainesville, FL) and accounted for no more than 2% of the total metal content of the mutants. Therefore, the manganese concentrations were used as the active enzyme concentration for catalytic measurements.

Crystallography

Crystals of E162D and E162A MnSOD were grown with a precipitant solution of 3 M ammonium sulfate, 50 mM imidazole, and 50 mM malate at pH 7.8–8.2 using the

vapor diffusion hanging drop method. Hexagonal crystals with dimensions of approximately 0.2 mm × 0.2 mm × 0.3 mm grew at room temperature (RT) within 1 week and were magenta in color. Diffraction data were collected from visually selected single crystals wet mounted in quartz capillaries (Hampton Research) on an R-AXIS IV⁺⁺ image plate system with Osmic mirrors and a Rigaku RU-H3R CU rotating anode operating at 50 kV and 100 mA. A 0.3 mm collimator was used with a crystal to detector distance of 220 mm and a 2 θ angle of 0°. The frames were collected using a 0.3° oscillation angle with an exposure time of 5 min/frame at RT. Both data sets were indexed using *DENZO* and scaled and reduced with *SCALEPACK* (Otwinowski & Minor, 1997). Useful diffraction data were collected to 2.3 and 2.5 Å resolution for the E162D and E162A MnSOD crystals, respectively. To prevent model bias, the E162D and E162A MnSOD crystal data sets were phased using the human wild-type MnSOD structure (Quint *et al.*, 2006) (PDB ID 2adq) in which the residue at position 162 was replaced with an alanine and all waters and the active site manganese had been removed. The structures were phased and refined using *CNS* (Brunger *et al.*, 1998). Refinement cycling (using rigid body, simulated annealing for the first cycle, and energy minimization and individual B-factor refinement for all subsequent cycles) was done in conjunction with rounds of manual model building using *COOT* for molecular modeling (Emsley & Cowtan, 2004). The refined model statistics are given in Table 2-2. The refined models and structure factor files have been deposited with the Protein Data Bank as entries 3c3t and 3c3s for E162D and E162A MnSOD, respectively.

Differential Scanning Calorimetry

Samples of each mutant were buffered with 20 mM potassium phosphate at pH 7.8, with a final enzyme concentration of 1 mg/mL. The samples and references were

then degassed for 10 minutes prior to data collection. Scans were performed by Patrick Quint in the Silverman lab, using a temperature range from 25-110 °C at a rate of 1 °C/min (Microcal VP-DSC). A buffer blank was subtracted from the final protein scan and a cubic baseline was fit to the profile. Changes in heat capacity (ΔC_p) for the unfolding peaks were corrected by fitting a reversible, non-two-state model with two components. Baseline correction and peak fitting were performed using *Origin* (Microcal Software, Northampton, MA).

Results

Metal Content Analysis

The replacement of Glu162 with either aspartate (E162D) or alanine (E162A) had no effect on the preferential binding of manganese to the active site, with both enzymes having an iron content of only 2 %. However, there was a large change in the amount of active enzyme present as determined by manganese analysis. The Mn occupancy of E162D was determined to be 88% and that for E162A was 54%, indicating a weaker metal binding site.

pH Profile

Wild-type human MnSOD with Mn^{3+} exhibits a characteristic absorbance at 480 nm. The reduced form, Mn^{2+} , on the other hand shows no significant visible absorbance peaks. The pH profile for wild-type human MnSOD was fit with a single ionization that had a pK_a of 9.2 ± 0.1 (Figure 2-2). Two different effects were seen with mutation of Glu162: E162D had a lower pK_a of 8.7 ± 0.2 while E162A had a higher pK_a of 10.1 ± 0.1 .

Catalysis

The reaction catalyzed by human MnSOD is the disproportionation of superoxide via a two-step mechanism in which the active site metal cycles between Mn^{2+} and Mn^{3+} . Concurrent with this cycling is the uptake or release of a proton by the manganese-bound solvent molecule, respectively (see Introduction for details). Additionally, during the second step of catalysis, a product-inhibited form of the enzyme occurs. In total, four rate constants for catalysis can be measured (eq 1-1 – 1-4): k_1 is the rate of reaction for the first step, the reduction of the Mn, the protonation of the Mn-bound hydroxide, and the release of dioxygen; k_2 is the rate of the second step along an uninhibited pathway, the oxidation of the Mn, deprotonation of the Mn-bound water, and the formation of H_2O_2 ; k_3 is the rate of formation of the product inhibited state; k_4 is the rate of release from the product inhibited state and subsequent formation of product, H_2O_2 . The values of k_1 - k_4 for wild-type, E162A, and E162D are provided in Table 1-1. The rate constant k_1 was measured using two different methods, the disappearance of superoxide ($\lambda=260$ nm) and the rate of change in the visible absorption of human MnSOD ($\lambda=480$ nm) under single turnover conditions ($[E] \gg [S]$) (Cabelli *et al.*, 1999). The resulting rates as measured by both methods were in agreement. The rate constants k_2 and k_4 were measured by first reducing the active site with H_2O_2 followed by superoxide generation via pulse radiolysis. This caused an increase in absorption at 480 nm, indicating the oxidation of the Mn and a return to the initial state of the enzyme. The initial part of the curve gave k_2 and the later part gave k_4 . Finally, k_3 was measured by monitoring the increase in absorption at 420 nm, the characteristic absorbance peak for the product-inhibited complex (Bull *et al.*, 1991, Hearn *et al.*, 2001), and the decrease in absorption at 480 nm (Figure 2-3).

There was no pH dependence observed for the values of k_1 - k_4 of wild-type human MnSOD in the pH range of 7.0-9.5. However, the value for k_1 in the E162D mutant was pH dependent and was fit to a single ionization with a maximum at $355 \pm 33 \mu\text{M}^{-1} \text{s}^{-1}$ and a $\text{p}K_a$ of 8.7 ± 0.2 . The data for k_2 and k_3 for E162D decreased to approximately $50 \mu\text{M}^{-1} \text{s}^{-1}$ at pH 9.9 from the values reported at pH 7.7 (133 and $215 \mu\text{M}^{-1} \text{s}^{-1}$, respectively) (Table 1-1). Additionally, the value for k_4 of E162D showed no pH dependence. Conversely, the values of k_1 - k_3 for the E162A mutant showed no pH dependence, but k_4 exhibited a 10-fold decrease as pH changed from 8 ($30 \pm 3 \text{s}^{-1}$) to 10 ($3 \pm 1 \text{s}^{-1}$) and was unable to be fit by a single ionization. Another rate constant, $k_0/[\text{E}]$, describing the product-inhibited, zero-order region of catalysis at steady state is near 500s^{-1} for wild-type, with no pH dependence (Hearn *et al.*, 2001, Hsu *et al.*, 1996). For E162D, the rate was decreased to a value of 270s^{-1} , and showed no pH dependence. The value of $k_0/[\text{E}]$ for E162A showed greater pH dependence with the rate decreasing from 190s^{-1} at pH 7.7 to 18s^{-1} at pH 8.4.

Structural Analysis

Both mutants of human MnSOD crystallized in the hexagonal space group $P6_122$ under similar crystallization conditions. The asymmetric unit consisted of one dimer with the tetramer formed by a crystallographic 2-fold symmetry operator. The structures of the two mutants did not show any large, overall structural deviations compared to wild-type with a rmsd of 0.2 \AA for both mutants.

The most significant difference between the mutant and wild-type structures was, not surprisingly, an alteration of the interaction between residue 162 and His163 at the dimeric interface (Figure 2-5). In the wild-type enzyme, there is a direct interaction between Glu162^B (where ^B indicates monomer B) and His163^A (where ^A indicates

monomer A). In E162D, the interaction between the two residues is mediated by a solvent molecule that apparently interacts with the carboxylate of Asp162^B and an imidazole nitrogen of His163^A. This interaction is completely lost in the E162A mutant due to the distance between the two residues and the hydrophobic nature of Ala162^B. In addition to this change in interaction, a putative sulfate is seen to penetrate into the channel near the 162^B-His163^A interaction. The sulfate is seen to enter further into the channel (and closer to the 162-163 interaction) as the side chain of residue 162 is shortened (Figure 2-5).

Thermal Stability

The major thermal transition temperatures for the unfolding of E162A and E162D were determined by differential scanning calorimetry. The data for E162D showed two peaks with melting temperatures that were very similar to that of wild-type human MnSOD. The thermal inactivation temperature for E162D was 72 °C with an unfolding temperature of 88 °C (Figure 2-4). For comparison, the values for wild-type enzyme were reported as 68 and 90 °C, respectively (Borgstahl *et al.*, 1996) with the values independently determined by our group to be 72 and 94 °C, respectively. The inactivation temperature for E162A was increased to 77 °C, though the denaturation temperature was decreased to 81 °C.

Discussion

Mutagenic analysis of residue 162 in human manganese superoxide dismutase has provided insights into the role of this second shell Mn ligand both catalytically and structurally. The sight specific mutants E162D and E162A create catalytic deficiencies that have been correlated to the accompanying structural changes.

Structures

The manganese ion in wild-type human MnSOD is coordinated by three histidines, one aspartate, and one solvent molecule, either a water or hydroxide depending on the stage of catalysis. Additionally there are several second-shell ligands that possibly play roles in fine-tuning the redox state of the Mn and the pK_a 's of surrounding solvent molecules and amino acids. Glu162 spans the dimeric interface and interacts directly with the adjacent monomer with His163, a coordinating ligand of the Mn (Figure 2-1, Figure 2-5 top). Mutation of glutamate to aspartate effectively shortens the length of the side chain by one carbon-carbon bond, and thus lengthens the interaction distance between the two amino acids. Keeping the carboxylate group, however, allows for a water molecule to intervene between the aspartate and histidine. Mutation to alanine completely abolishes the interaction due to the much shorter, hydrophobic side chain.

Interestingly, a sulfate molecule was observed adjacent to this portion of the dimeric interface, and represents a novel sulfate binding site. This indicates the widening of a solvent-accessible channel that exists along the dimeric interface. In E162D, this sulfate displaces a water molecule (S_2 in Figure 2-1) that is believed to be part of a putative proton wire. Further inward movement of the sulfate in the E162A mutant allows it to interact directly with the side chains of His30 and Tyr34, both of which are partially solvent exposed in wild-type. This suggests that part of the catalytic deficiency of the mutant enzymes is due in part to a weakening of the proton wire, thus providing further support for a role of proton transfer in the catalytic mechanism. It should be noted that the catalytic effects of sulfate were not examined, as no sulfate was present in the kinetic or spectroscopic assays.

Thermal denaturation analysis, as measured by differential scanning calorimetry, indicates that the Glu162^B-His163^A interaction plays a role in stabilizing the protein. The maintenance of the interaction by a water molecule in E162D results in only a slight, possibly insignificant, decrease in the major unfolding transition (88 °C for E162D, 90-94 °C for wild-type). The E162A mutant in which this interaction is lost and the major unfolding transition occurs at 81 °C further supports this stabilizing role. The loss of this interaction did not affect the ability of the protein to form tetramers, indicating that there were no major changes in overall protein mobility.

Spectroscopic Properties

Wild-type human Mn³⁺SOD exhibits a broad absorption spectrum with a peak at 480 nm (Bull *et al.*, 1991, Hsu *et al.*, 1996, Maliekal *et al.*, 2002). The pH profile at this maximum titrates with a p*K*_a value of 9.2. It is believed that the source of this ionization is Tyr34 with evidence provided by a study done on *E. coli* MnSOD (Maliekal *et al.*, 2002) and Y34F human MnSOD, which has a significantly altered p*K*_a of 11 (Hsu *et al.*, 1996, Guan *et al.*, 1998). There is a shift of this critical p*K*_a in E162D and E162A human MnSOD, though the shifts occur in opposite directions (wild-type = 9.2 ± 0.1, E162D = 8.7 ± 0.2, E162A = 10.1 ± 0.1) (Figure 2-2). This effect is likely due to the indirect interaction between Glu162^B and Tyr34^A (Figure 2-1). The side chain of Tyr34^A is located 6.2 Å away from the carboxylate of Glu162^B in wild-type human MnSOD. The interaction traces a path from Glu162^B to His163^A, and then to solvent molecule S₂, which interacts with Tyr34^A. The preservation of the Asp162^B-His163^A interaction via a mediating water in E162D results in an enzyme in which the p*K*_a is only slightly altered. The loss of this indirect interaction in E162A results in a much larger (1 pH unit) p*K*_a shift with a value similar to that of tyrosine in solution.

Catalysis

A diminished level of catalysis (4-8 fold) was seen in E162D MnSOD as measured by k_1 and k_2 (Table 1-1). Mutation to alanine results in an enzyme with a 22-24 fold lower rate for k_1 and k_2 . The observed changes in catalytic rates are a result of the weakened or lost dimeric interfacial interaction between 162^B and His163^A and the subsequent effects on the properties of the active site metal and the atoms in the active site. Similar effects have been observed in previous studies that have shown that mutations of second-shell ligands and also at the dimeric interface can have substantial effects on the catalytic properties of human MnSOD. Mutation of the second shell ligand (via the Mn-bound solvent) Gln143 to asparagine resulted in a 100-fold reduction in catalytic activity. Also, there was evidence of an increase in the redox potential of the active site, as Q143N enzyme did not have an absorbance peak at 480 nm (Leveque *et al.*, 2000, Hsieh *et al.*, 1998). Another mutation, the dimeric interfacial mutant Y166F, resulted in a breaking of the proton wire and, not surprisingly, caused a 10-fold decrease in catalysis (Hearn *et al.*, 2004).

The catalytic rate, k_1 , for the E162D mutant exhibited an interesting property. The pH dependence of k_1 gave a pK_a near 8.7 that is nearly in agreement with the pK_a from the spectroscopically monitored titration of the active site (Figure 2-2). This indicates that there is a catalytic dependence on the protonated state of a single group with a pK_a near 8.7. It is possible that the group of interest is the Mn-bound hydroxide/water, as one would expect the most noticeable effects to occur closer to the metal due to the second-shell nature of the mutated residue. It is also possible that this group is an amino acid that lies near the active site, as this rate is dependent on proton-transfer to the Mn-bound hydroxide. However, pinpointing this location would require concurrent

mutational analysis at other positions in the active site, such as Tyr34 and Gln143, for example. This property was not observed in E162A, which had a spectroscopically titrated pK_a of around 10.1. It may very well be that there is an equivalent kinetic (k_1) pK_a , though this pH value is above the range utilized in the kinetic measurements.

As was previously mentioned, the mutant E170A in *E. coli* MnSOD is equivalent to the E162A mutant of human MnSOD. Interestingly, the properties of these two mutants showed some dramatic differences. The E170A *E. coli* MnSOD mutant resulted in an enzyme that preferentially bound iron, was catalytically dead, and had greatly weakened dimeric stability in solution. In contrast, E162A human MnSOD retained apparent dimeric stability and its preference for manganese though with substantially reduced activity relative to wild-type. Not surprisingly, the enzyme appeared to retain its tetrameric structure in solution and this tetramerization may keep the protein stable despite the weakened dimeric interface. The reason for the differences in the properties of these two mutants is not immediately apparent upon structural alignment of their structures. The dimeric interfaces of the two enzymes are nearly identical, as are all other amino acids (not including position 162) throughout the protein. However, analyzing the area at the mouth of the active site reveals that there exists an interaction between a phenylalanine and glutamine that is flip-flopped between the two enzymes. The role of this interaction will be discussed in the next chapter.

Another feature of catalysis that is prominent in human MnSOD is the large extent of product inhibition relative to the prokaryotic enzymes (Hearn *et al.*, 2001, Hsu *et al.*, 1996). The value of $k_0/[E]$, a measure of the zero-order rate constant for superoxide turnover in the product inhibited pathway at steady state was lower for E162D (270 s^{-1})

and E162A (190 s^{-1}) than that for wild-type (500 s^{-1}). Furthermore, the rate of formation (k_3) and release (k_4) of the product-inhibited state were diminished in both mutants (Table 2-1). Yet another measure of the extent of product inhibition is obtained by comparing the values of k_2 and k_3 , known as the gating ratio (k_2/k_3). The value of this ratio obtained for both mutants is roughly 0.6, indicating enhanced flux through the pathway of formation of the product-inhibited complex (eq 1-3). These data indicate that the extent of product inhibition was greater for the two mutants due to a preferential entrance into the product-inhibited state (k_3) and a slow rate of release of the product-inhibited state (k_4). These results suggest that Glu162 plays a role not only in the tuning of the pK_a and redox state of the active site environment, but also in the release of the product-inhibited state.

Conclusions

The dimeric interface of human MnSOD plays a role in several aspects of the enzyme's structure and function. Glu162 at the dimeric interface interacts directly with His163 on a neighboring monomer, a direct ligand of the Mn. Mutational analysis (E162D and E162A) showed that this interaction is important in determining the stability of the tetrameric complex as evidenced by a decrease in the temperature of the major unfolding transition that was dependent on the degree of interaction between residue 162^B and His163^A. Kinetic analysis showed that there was also a substantial loss of catalytic activity in the mutants and that there was a greater degree of product inhibition exhibited. These results illustrate the need to understand the role of the dimeric interface as the development of novel antiproliferative forms of MnSOD is undertaken (Davis *et al.*, 2004), as mutations may cause unexpected, undesirable effects. The

dimeric interface must also be examined to further understand its role in altering the properties of the eukaryotic MnSODs as compared to their prokaryotic counterparts.

Table 2-1. Rate constants for catalysis by wild-type and mutant human MnSOD

Enzyme	k_1 ($\mu\text{M}^{-1} \text{s}^{-1}$)	k_2 ($\mu\text{M}^{-1} \text{s}^{-1}$)	k_3 ($\mu\text{M}^{-1} \text{s}^{-1}$)	k_4 (s^{-1})
wild type ^a	1500	1100	1100	120
E162D ^b	355 ± 33	133 ± 16	215 ± 20	40 ± 4
E162A ^b	63 ± 4	50 ± 4	87 ± 8	30 ± 3

^a From Quint *et al.*, 2006. ^b In 2 mM TAPS (pH 7.7), 50 mM EDTA, and 30 mM formate at 25 °C

Table 2-2. X-ray diffraction data processing and structure refinement statistics for E162D and E162A human MnSOD

Parameter	E162D	E162A
Space group	<i>P6₁22</i>	<i>P6₁22</i>
Unit cell parameters (Å)	<i>a</i> = 81.3, <i>c</i> = 241.7	<i>a</i> = 81.3, <i>c</i> = 242.5
Resolution (Å)	20-2.2 (2.28-2.20) ^a	20-2.5 (2.59-2.50)
No. of unique reflections	23358	15609
Completeness (%)	93.5 (90.7)	90.1 (92.7)
R _{sym} ^b (%)	11.2 (19.6)	11.4 (21.0)
I/σ(I)	28.2	22.2
R _{cryst} ^c (%)	17.58	17.7
R _{free} ^d (%)	20.09	22.2
No. of protein atoms	3106	3100
No. of water molecules	175	103
rmsd for bond lengths (Å)	0.006	0.006
rmsd for bond angles (°)	1.248	1.325
Average B-factors (main/side/solvent)	21.7/24.4/35.3	26.8/28.2/33.4
Ramachandran Plot (%) (favored/additional/generous)	91.2/1.2/7.6	91.8/7.0/1.2

^a Data in parentheses are for the highest resolution shell. ^b $R_{\text{sym}} = (\sum |I - \langle I \rangle| / \sum \langle I \rangle) \times 100$. ^c $R_{\text{cryst}} = (\sum ||F_o| - |F_c|| / \sum |F_o|) \times 100$. ^d R_{free} is calculated the same as R_{cryst}, except with 5% of the data omitted from refinement.

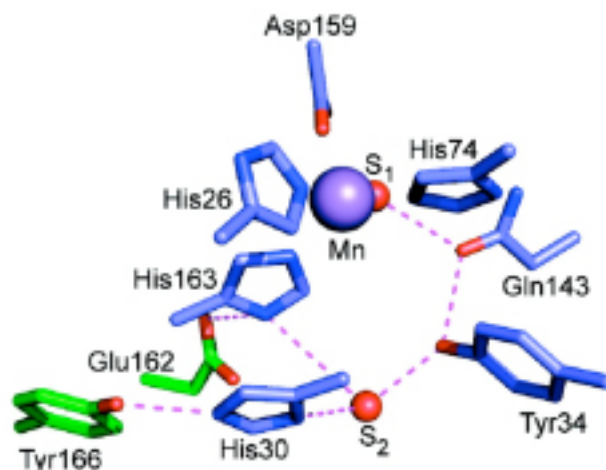


Figure 2-1. The active site structure of wild-type human manganese superoxide dismutase shows an intricate interaction network. The active site is made mostly of amino acids from one monomer (blue) coordinating the manganese (purple sphere) with two solvent waters (red spheres). Second shell ligands of the Mn are contributed by a neighboring monomer (green).

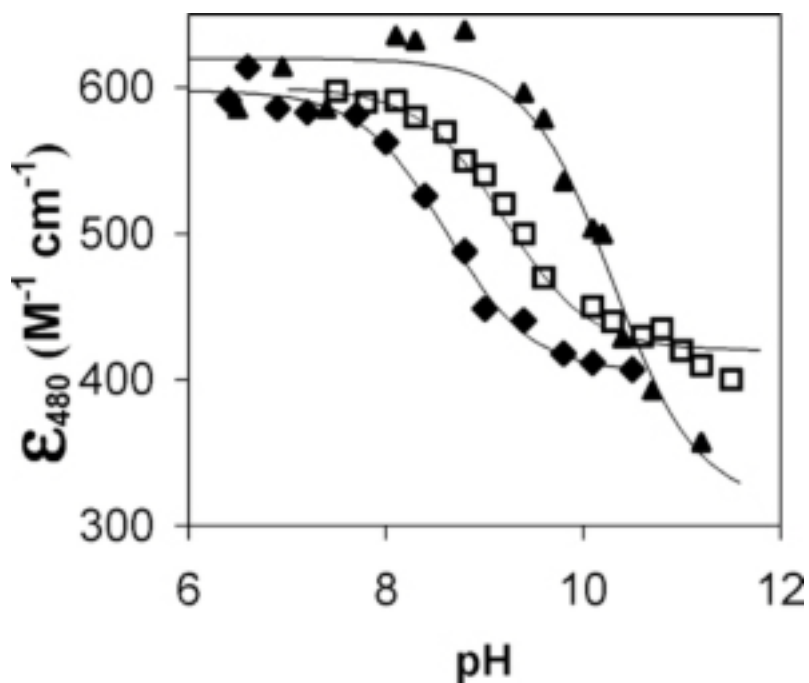


Figure 2-2. The pH profile for molar absorptivity at 480 nm for hMn³⁺SOD, wild-type and mutants. Data for wild-type (□), E162D (◆), and E162A (▲) were fit to a single ionization with pKa values of 9.2 ± 0.1 , 8.7 ± 0.2 , and 10.1 ± 0.1 , respectively. Measurements were made in solutions buffered with 200 mM MES and TAPS at 25 °C.

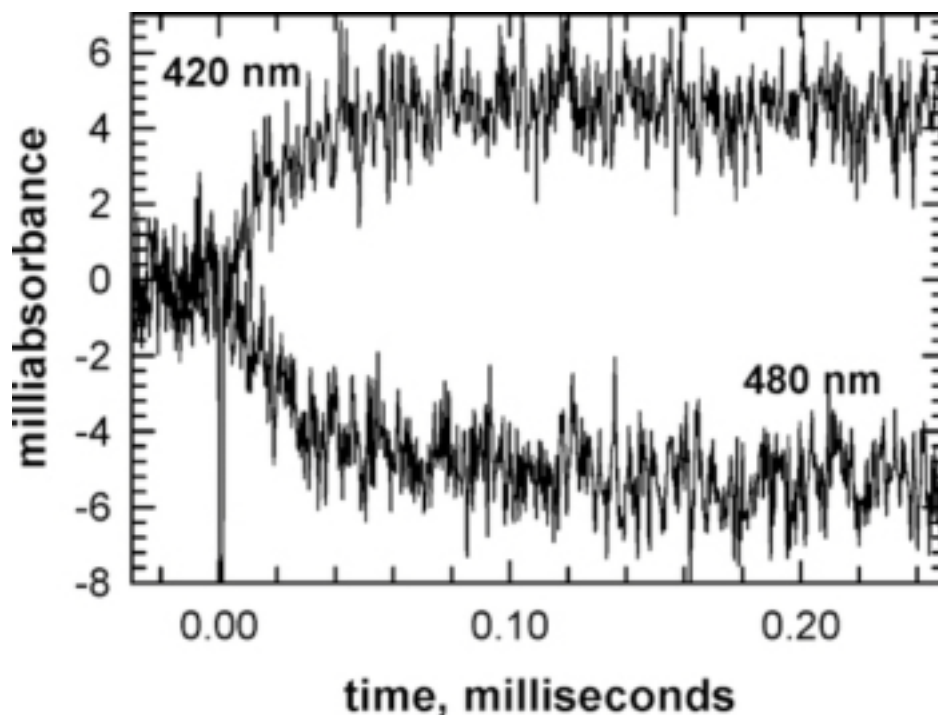


Figure 2-3. Change in absorbance at 420 and 480 nm over a 0.25 ms time scale after generation of superoxide by pulse radiolysis in a solution containing E162D human MnSOD. The decrease in the 480 nm reading is due to the reduction of the active site manganese after the first round of catalysis. The increase in the 420 nm reading is due to the formation of the product-inhibited complex. This is achieved by first reducing the Mn with H_2O_2 , followed by generation of superoxide by pulse radiolysis. Both changes in absorbance were fit to first-order processes to give k_3 .

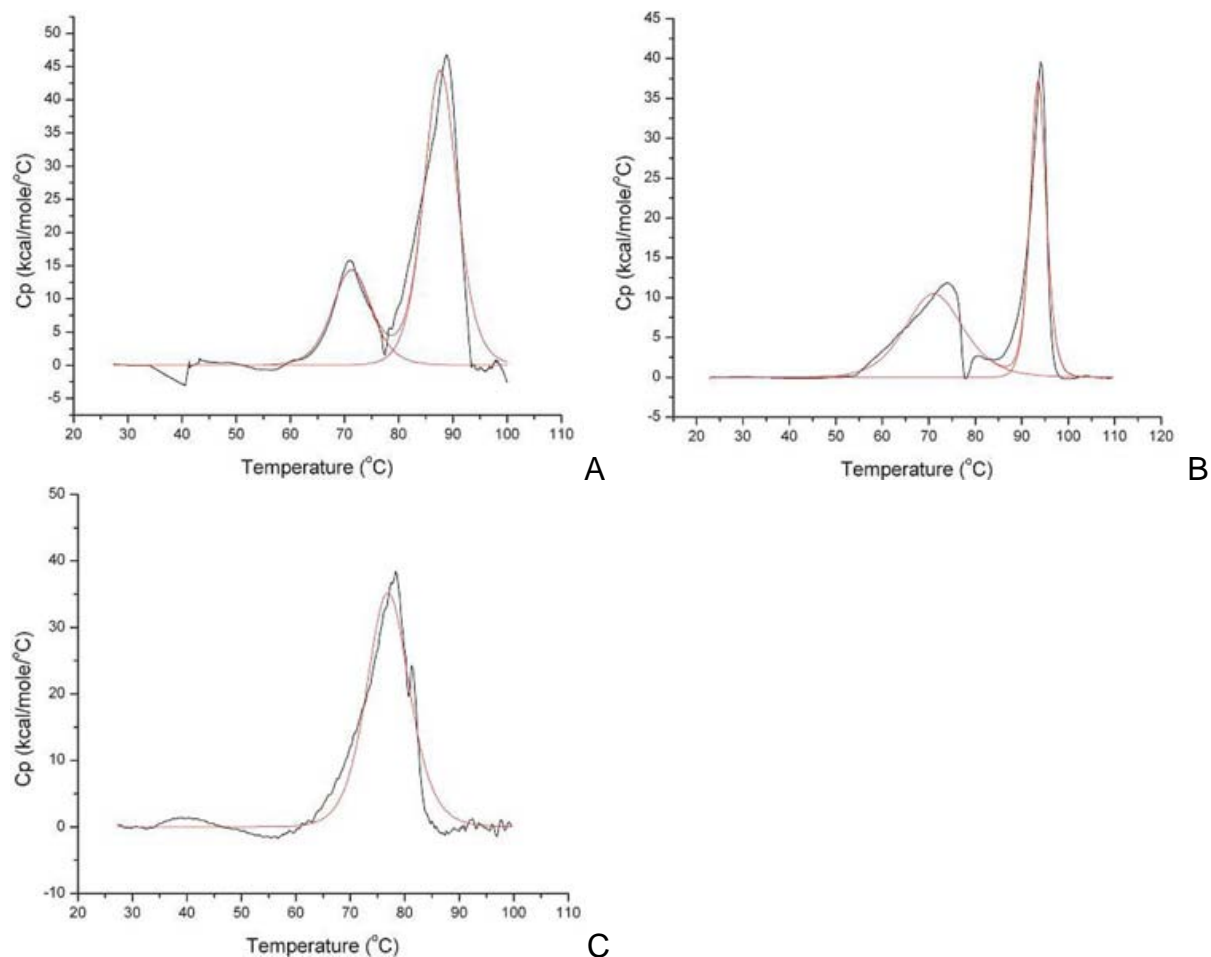


Figure 2-4. Normalized transitions for E162D (A), wild-type (B), and E162A (C) human MnSOD as determined by differential scanning calorimetry. Enzyme concentrations for each enzyme were 1.0 mg/mL. The data was fit with a non-two-state model. The normalized calorimetric trace is in black and the red line is a fit to the model, assuming non-cooperative transitions. The average temperatures for inactivation and melting are listed in the text. Each experiment is the average of three scans with the subtraction of the reference buffer.

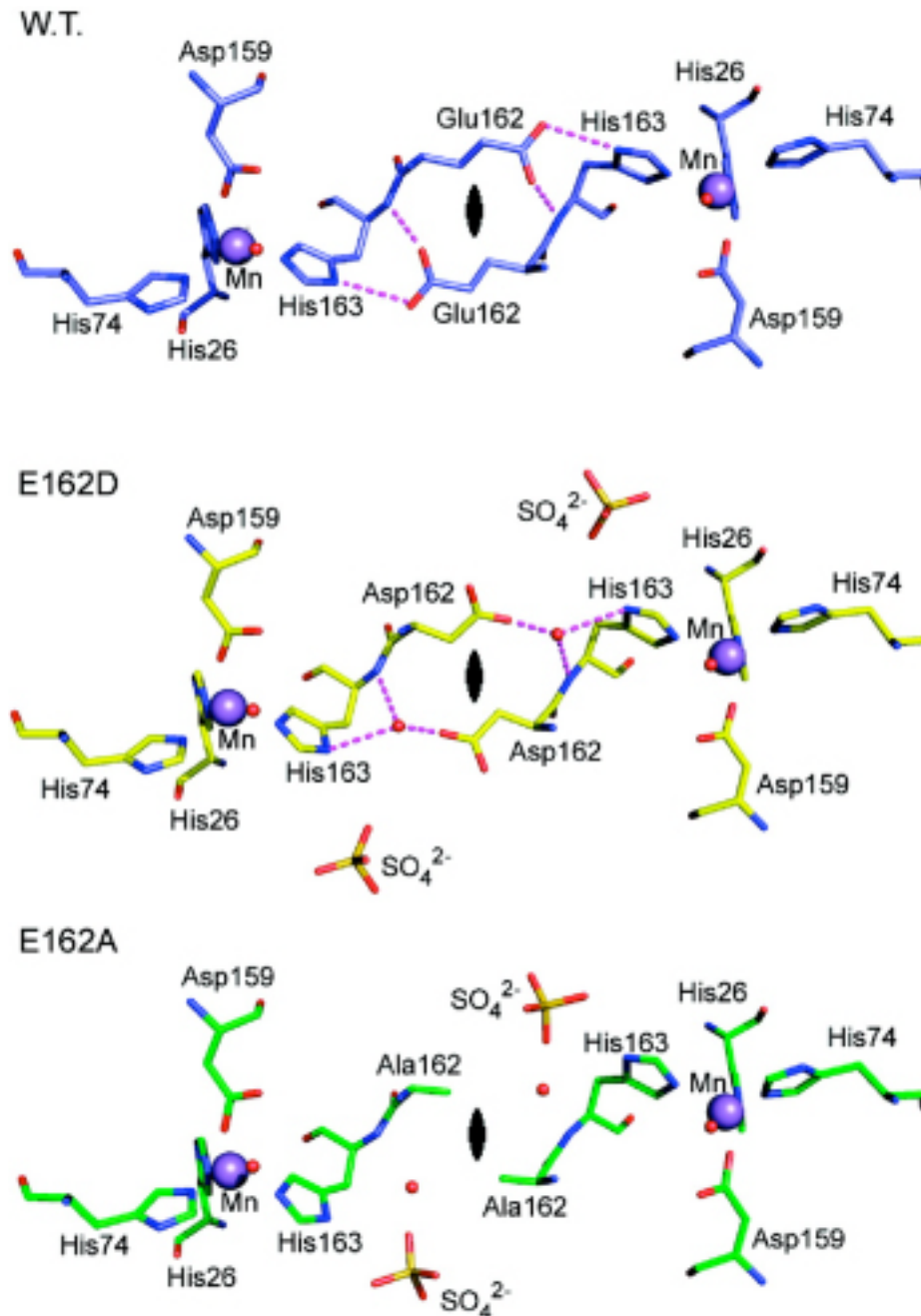


Figure 2-5. Structures of the dimeric interface of wild-type (top), E162D (middle), and E162A (bottom) human MnSOD. The active site manganese ions are shown as a purple spheres, waters as small, red spheres, and putative hydrogen bonds as magenta dashes. The black ellipsoids illustrate the two-fold axis of symmetry that separates one chain from the other. A solvent molecule was observed to bridge the interaction between Asp162 and His163 in E162D, while no interaction was observed in E162A.

CHAPTER 3

COMPARATIVE STUDY OF HUMAN AND *ESCHERICHIA COLI* MANGANESE SUPEROXIDE DISMUTASE: KINETIC AND STRUCTURAL INSIGHTS

As was discussed in the previous chapter, the dimeric interface of the manganese superoxide dismutases plays an important role in the catalytic and structural properties of the enzyme. Mutagenic analysis of a second shell ligand, Glu162, in human MnSOD resulted in an enzyme, E162A, which had very different properties from its *E. coli* MnSOD counterpart, E170A. In chapter 3, further mutagenic analysis at the dimeric interface of human MnSOD is performed in order to create an enzyme that is more *E. coli*-like. That is, an enzyme with a lesser degree of product inhibition.

Introduction

Manganese superoxide dismutases catalyzes a two-step reaction in which the active site Mn cycles between +2 and +3 oxidation states and the manganese-bound solvent is protonated and subsequently deprotonated (eq 1-1 – 1-4). As is measured by pulse radiolysis the catalytic cycle begins with an ultrafast neutralization of superoxide anion. However, during the second step of the catalytic cycle, a product-inhibited form of the enzyme appears. This complex involves the binding of oxidized manganese (Mn^{3+}) to superoxide in the absence of a proton, forming an $Mn^{3+}-O_2^{2-}$ intermediate. The structure of this inhibited-state has not been visualized directly, but there is evidence for two conformations. The first theory is based on spectroscopic evidence and suggests that the inhibited state is a side-on peroxo complex with the manganese (Bull *et al.*, 1991; McAdam *et al.*, 1977; Abreu *et al.*, 2007). Computational calculations, on the other hand, suggest an end-on complex in which the peroxo compound is coordinated by the manganese and the hydroxyl of Tyr34 (Abreu *et al.*, 2005). In order for the enzyme to continue, a proton must be transferred into the active site. Evidence

for this proton transfer event is demonstrated by an observed solvent hydrogen isotope effect of 3.1. It has further been suggested that this proton transfer is the limiting step in release of the product-inhibited state, and therefore catalysis (Hsu *et al.*, 1996).

Analysis of the human MnSOD active site hints at how the proton would be transferred into (or out of) the active site. At the core, the manganese ion is coordinated by three histidines, an aspartate, and a solvent molecule (water or hydroxide).

Extending out of the active site is an apparent hydrogen bonded network of amino acid side chains and waters (Figure 2-1). This network is present in both human and *E. coli* MnSODs as well as in iron SODs (Miller *et al.*, 2004; Borgstahl *et al.*, 1992; Lah *et al.*, 1995; Smith & Doolittle, 1992) (Figure 3-1). Despite the similarities at the core of the active site, the human and *E. coli* MnSODs exhibit one major catalytic difference: the *E. coli* enzyme, as well as most other bacterial MnSODs, has a reduced level of product inhibition (Bull *et al.*, 1991; McAdam *et al.*, 1977; Hsu *et al.*, 1996; Abreu *et al.*, 2007). Prior efforts have attempted to lower the magnitude of product inhibition of human MnSOD (Hearn *et al.*, 2001). This work was motivated by the observation that the lower product inhibition of an H30N mutant of human MnSOD is anti-proliferative when over-expressed in human cancer cells (Davis *et al.*, 2004). The theory is that there is an increase in H₂O₂ production in the lesser product inhibited forms. It has been shown previously that H₂O₂ is a potent regulator of various cellular processes and that increased H₂O₂ levels lead to an arrest of cellular growth (Sundaresan *et al.*, 1995; Rodriguez *et al.*, 2000; Davis *et al.*, 2004). The problem with identifying lesser product inhibited forms of human MnSOD is that mutation typically results in enzymes that have lower catalytic efficiencies, as demonstrated in Chapter 2 (Quint *et al.*, 2008).

Therefore, rational design of an enzyme with wild-type efficiency and lower product inhibition requires an understanding of the mechanism of product inhibition.

A large amount of research has been devoted to understand the role of Tyr34 in the catalytic mechanism of human MnSOD (Maliekal *et al.*, 2002; Whittaker & Whittaker, 1997; Guan *et al.*, 1998; Edwards *et al.*, 2001). Mutation of the tyrosine to phenylalanine (Y34F) resulted in an enzyme that had a significantly increased level of product inhibition (Guan *et al.*, 1998). Thus, Tyr34 is indispensable for catalysis, and it may be that its environment is an important determinant of this role. In fact, this environment differs between the human and *E. coli* enzymes and represents one of the very few active site differences between the two enzymes. This region exists at the dimeric interface and involves the interaction between a phenylalanine and a glutamine (human) or asparagine (*E. coli*) (Figure 3-1). In the human enzyme, Phe66^A lies near Gln119^B. In *E. coli* MnSOD, this interaction is flip-flopped, with Gln73^A neighboring Phe124^B.

To better understand the catalytic differences between *E. coli* and human MnSODs, mutagenic analysis was performed at residue Phe66 of human MnSOD. (Zheng *et al.*, 2007). Two mutants were created, F66A and F66L, with the F66L enzyme closely resembling the *E. coli* enzyme in terms of catalytic activity (reduced product inhibition), thus identifying a region of the active site that affects product inhibition.

Materials and Methods

Enzymes

Mutant enzymes were created by site-directed mutagenesis of the cDNA encoding human MnSOD in a pTrc99A vector using the QuikChange kit (Stratagene, La Jolla,

CA). Successful mutagenesis was confirmed with DNA sequencing (ICBR, University of Florida). Mutation-containing plasmids were then transformed into a strain of *E. coli* that lacked the genes encoding FeSOD (*SodB*) and MnSOD (*SodA*) (Carloz *et al.*, 1986). The protein was then expressed and purified as discussed in Chapter 2. Manganese concentrations were checked by inductively coupled plasma mass spectrometry with the active enzyme concentration taken as the manganese concentration.

Pulse Radiolysis

Kinetic rate constants were determined via pulse radiolysis performed by Diane Cabelli at Brookhaven National Lab. A more detailed version of the reaction conditions can be found in Chapter 2.

Crystallization

The enzymes both crystallized in normal human MnSOD conditions (2.5 M ammonium sulfate, 100 mM imidazole, 100 mM malic acid) using the hanging drop vapor diffusion technique.

Data Collection and Refinement

X-ray diffraction data were collected using a Rigaku RU-H3R CU rotating anode generator running at 50 kV and 100 mA, with Osmic mirrors, a 0.3 mm collimator and R-AXIS IV⁺⁺ image plates. Due to the large unit cell vector along the *c* axis, the crystal-to-detector distance was set at 190 mm with an oscillation of 0.3° per image over 45° total collection. One crystal was used for the F66L structure whereas two crystal data sets were merged for F66A. X-ray data processing was performed using *DENZO* and the data were scaled (and merged) with *SCALEPACK* (Otwinowski & Minor, 1997).

Initial attempts at direct phasing using the structure of wild-type human MnSOD (PDB ID 1luv, Hearn *et al.*, 2003) were unsuccessful. Molecular replacement was then

performed with the program *MOLREP* from the *CCP4* suite of software (Collaborative Computational Project, Number 4, 1994; Vagin & Teplyakov, 1997). This showed that the tetrameric interfacial 2-fold coincided with one of the crystallographic 2-folds.

Normally the dimeric interfacial 2-fold is coincident for this space group.

To avoid phase bias, prior to refinement the side chains of residue 66 and Gln119 were mutated to alanines and all solvent atoms and the Mn were removed. Both structures were refined using the *CNS* suite of programs with initial rounds of rigid body refinement and simulated annealing to 3000 K (Brunger *et al.*, 1998). Iterative rounds of energy minimization and B-factor were then performed with an intervening round of manual model building and automated water picking in the graphics program *COOT* (Emsley & Cowtan, 2004). The F66A structure was refined to 2.2 Å resolution with a final R_{cryst} of 19.5%. Similarly the F66L structure was refined to 2.3 Å resolution with a final R_{cryst} of 19.9%. Complete data processing and model refinement statistics are given in Table 3-1. The atomic coordinates and structure factors for F66A and F66L were deposited in the Protein Data Bank with PDB IDs 2qka and 2qkc, respectively.

Results

Catalysis

Rate constants for the catalytic pathway described in Chapter 1 (eq 1-1 – 1-4) were determined using pulse radiolysis to generate superoxide and monitoring the decrease in absorbance and 260 nm, the peak absorbance for superoxide ($\epsilon_{260} = 2000 \text{ M}^{-1} \text{ cm}^{-1}$) (Rabani *et al.*, 1969). For a detailed explanation of the procedures used to determine the rate constants, see Results in Chapter 2. The F66L mutant showed a more rapid initial catalytic rate than F66A, however both enzymes were impaired as compared to wild-type (complete kinetic data are given in Table 3-2). F66A, but not

F66L, showed a region of zero-order catalysis corresponding to the product-inhibited form of the enzyme that is predominant in catalysis by human MnSOD (Figure 3-2). The rate of superoxide decay in this zero-order region, $k_0/[E]$, for F66A was 1740 s^{-1} . This value is about three times greater than that for wild-type human MnSOD (500 s^{-1}), indicating a lower degree of product inhibition in F66A. Due to the lack of a zero-order region in catalysis by F66L, k_2 - k_4 were determined using the Numerical Integration of Chemical Kinetics program in *PRWIN* (H. Schwartz, Brookhaven National Laboratory), fitting to the data shown in Figure 3-2.

The rate constants for k_1 - k_4 were virtually pH independent over the pH range 6.5-8.5 for both F66L and wild-type human MnSOD. There was a small decrease in rate at pH greater than pH 8.5, however the data could not be fit with a single ionization. F66A exhibited similar traits for k_1 - k_3 , however k_4 showed an increasing value with increasing pH (Figure 3-3) (from 65 s^{-1} to 150 s^{-1}). It should be noted, though, that there is an increase in experimental error as pH increases.

The product inhibition of F66L as well as wild-type human MnSOD and wild-type *E. coli* MnSOD were examined in greater detail by examining the extinction coefficients of the enzymes over a range of wavelengths, on short (0.2-1.0 ms, all) and long (>50 ms, wild-type human) time scales (Figure 3-4). Wild-type human MnSOD showed signs of the formation of a reversible intermediate on short time scales, as evidenced by the drop in absorbance at 480 nm. On longer time scales, the spectrum returned to that of Mn^{3+}SOD , with a peak at 480 nm. Examination of both time scales for F66L human MnSOD and wild-type *E. coli* MnSOD did not reveal the formation of this reversible state (data for short time scale shown in Figure 3-4).

Structural Analysis

Mutation of Phe66 to alanine and leucine showed no global effects on the structure of human MnSOD. There were effects on the positions of two amino acids near residue 66^A, Tyr34^A and Gln119^B. In the F66L structure, Leu66 was positioned similar to Phe66 in the wild-type enzyme, with the γ and δ_1 carbons of Leu66 nearly superimposing on the same atoms of Phe66. This positioning caused the δ_2 carbon of the leucine to extend towards the surface of the enzyme and Gln119B, thereby shifting the side chain of the glutamine towards the surface of the enzyme to maintain the distance between the two residues (Figure 3-5). The loss of the phenyl group in the mutation F66A allowed for the side chain of Gln119^B to face into the active site with a bend of about 90° at the γ carbon (Figure 3-5). In both mutants, the position of Tyr34 was shifted towards the surface of the enzyme by about 0.5 Å. This position of Tyr34 is more similar to that seen in *E. coli* MnSOD. In addition to the effects on amino acids, the positions of two water molecules were affected (Figure 3-6). W_{2A} connects the side chains of Tyr34 and His30 and W_{2B} is positioned between residues 66 and 119 and the hydroxyl of Tyr34. The distances between the two waters and Tyr34 remain relatively unchanged in the mutant structures. However, the two waters are further apart from each other in the mutants relative to wild-type human MnSOD (Figure 3-7, Table 3-3).

Further structural analysis was undertaken to examine the changes in the mobility in the residues surrounding the mutation site. This is accomplished by looking at the B-factors of these atoms. A B-factor is a crystallographic measure of the thermal motion associated with a given atom. To make this comparison, the B-factors had to be normalized across all structures (F66A, F66L, wild-type human MnSOD, and wild-type *E. coli* MnSOD). This was especially important because the *E. coli* MnSOD structure

was solved at 100 K, while all of the human structures were determined at room temperature (Borgstahl *et al.*, 2000). Normalization was performed for each atom individually the equation:

$$B_{\text{norm}} = B_{\text{atom}} \times [\langle B_{\text{cons protein}} \rangle / \langle B_{\text{cons total}} \rangle] \quad (3-1)$$

Where B_{atom} is the calculated B-factor for the atom and $\langle B_{\text{cons protein}} \rangle$ and $\langle B_{\text{cons total}} \rangle$ are the average B-factors for the given protein and all four proteins over a conserved region, respectively. This conserved region is the main chain atoms (C, N, O, and C $^{\alpha}$) of residues in regions of conserved tertiary structure between the human and *E. coli* MnSODs (human residues 21-34, 120-126, 157-175; *E. coli* residues 21-34, 125-131, and 165-178). This selection of normalization residues (rmsd 0.2 Å) was chosen due to the high degree of structural variation between human and *E. coli* MnSODs, outside of the core of the enzyme. The error bars shown in Figure 3-8 were calculated by comparing the normalized B-factors for identical residues in the A and B monomers, where A and B were solved independently (i.e. without the use of a non-crystallographic symmetry operator).

This B-factor analysis showed that the manganese ion, solvent W_1 , Tyr34 and His30 were well ordered in all four enzymes (Figure 3-8). Solvent molecule W_{2B} was relatively more disordered in F66A, F66L, and *E. coli* MnSOD compared to wild-type human MnSOD. Interestingly, solvent molecule W_{2A} was more disordered in the two enzymes that exhibited a lower level of product inhibition, F66L and *E. coli* MnSOD, while it was relatively equally ordered in wild-type and F66A human MnSOD.

Discussion

Despite the high degree of structural similarity between the monomers of eukaryotic and prokaryotic MnSODs, there are substantial catalytic differences between

the classes, most notably in the level of observed product inhibition. A comparison of human and *E. coli* MnSODs reveals one significant difference at the mouth of the active site. This is the interaction between a phenylalanine on one monomer and a glutamine (human) or asparagine (*E. coli*) on a neighboring monomer. Phe66 in human MnSOD lies near the catalytically important residue Tyr34, a residue that has been extensively studied in human (Greenleaf *et al.*, 2004, Guan *et al.*, 1998) and *E. coli* MnSODs (Maliekal *et al.*, 2002; Whittaker & Whittaker, 1997; Edwards *et al.*, 2001). It therefore can be hypothesized that Phe66 exerts effects, indirectly, on Tyr34. To understand the role of this region, site-specific mutants of human MnSOD were made at residue 66 (F66A and F66L).

Catalysis

Initial kinetic analysis of F66A and F66L human MnSODs demonstrated that Phe66 is not vital for catalytic activity of the enzyme, as both mutants exhibited only minor decreases in catalytic rates when compared to wild-type (compare to the large decreases seen in Table 2-1 for E162D and E162A human MnSOD). Despite the small change in rate constants, it is very obvious from Figure 3-2 that there are differences in the progress curves of the enzymes. The zero-order catalysis seen in F66A is similar to that of wild-type human MnSOD, indicating that this mutant retains a similar level of product inhibition (Bull *et al.*, 1991; McAdam *et al.*, 1977). Interestingly, there is virtually no zero-order catalysis seen in F66L human MnSOD, which is similar to the properties of *E. coli* MnSOD, indicative of a low level of product inhibition. Similarly, spectroscopic evidence shows that wild-type human MnSOD forms a short-lived intermediate that is not seen in *E. coli* or F66L human MnSOD (Figure3-4).

Further analysis of the degree of product inhibition is provided by analysis of the gating ratio, k_2/k_3 . A value of 1, as seen in wild-type human MnSOD, indicates that there is an equal transition of this enzyme into an uninhibited second step as well as into a stage of product-inhibition. In *E. coli* MnSOD this ratio is 4, which means that this enzyme favors an uninhibited route of catalysis during the second step (Table 3-2). The mutant F66A has a gating ratio that is nearly equal to that of wild-type human MnSOD, whereas F66L has a gating ratio that is very similar to that of *E. coli* MnSOD, thus providing additional evidence that F66L has a low level of product inhibition. One may note that k_4 is also part of the inhibited step of catalysis and therefore could be included in analysis of product inhibition. In fact, analysis of k_4 of these mutants shows that k_4 is decreased in both enzymes, making each more similar to the *E. coli* enzyme. However, it should be noted that the lower rate of k_3 in these enzymes lowers the level of inhibited state and, therefore, could directly lower the rate of release from the inhibited state. In other words, the number of cycles of release from the product inhibition is lower in F66L, as there is a lower concentration of the product-inhibited state available (increase k_2 , decreased k_3). This is what is seen in F66L, as this enzyme exhibits the lowest rate for k_4 (Table 3-2), but also demonstrates a nearly undetectable level of product inhibition (Figure 3-2).

Previous mutagenic analysis of human MnSOD has provided another mutant that exhibits a lower level of product inhibition, H30N (Hearn *et al.*, 2001; Greenleaf *et al.*, 2004). The reason for the decreased inhibition is not the same in H30N as it is in F66L. In H30N, there is a greatly increased rate, k_4 (480 s^{-1}), and no change in the gating ratio k_2/k_3 , as compared to wild-type. Therefore, the product-inhibited state forms just as

readily, possibly due to impaired proton transfer, however it is released much more rapidly (Ramilo *et al.*, 1999). This is in contrast to the lower rate of entry into the product-inhibited state (k_3) by F66L.

Active Site Environment

An examination and comparison of the crystal structures of these enzymes provides some rationalization of these results. Among the most obvious structural differences is the conformation of the amino acids surrounding the site of mutation. In wild-type human MnSOD Phe66^A neighbors Gln119^B at the dimeric interface. Mutation of phenylalanine to alanine results in a conformational change in Gln119. The loss of the bulk of the side chain at residue 66 allows the side chain of Gln119 to bury itself into the active site, occupying space that would normally sterically clash with Phe66 (Figure 3-5). This rotation allows the polar side chain of residue 119^A to interact with solvent molecule W_{2B} , which normally only interacts directly with Tyr34^A. This novel interaction does not alter the interaction distance between W_{2B} and Tyr34^A, however the position of W_{2B} moves outward, away from the active site Mn (Figure 3-6, Table 3-3). Associated with this movement is an increase in the inherent mobility of W_{2B} as measured by the normalized atomic B-factor (Figure 3-8). This increased mobility is also associated with *E. coli* and F66L MnSOD when compared with wild-type human MnSOD. Even more notable is the change in mobility of solvent molecule W_{2A} , which mediates an interaction between Tyr34 and His30. There is no apparent change in the normalized B-factor of W_{2B} in F66A compared to wild-type human MnSOD (Figure 3-8). However, both F66L and *E. coli* MnSOD show an increased level of mobility for W_{2B} relative to wild-type human MnSOD. Additionally, solvent molecule W_{2A} is more dynamic in both mutants as well as the *E. coli* enzyme.

This increased mobility of the solvent in the active site correlates to the level of product inhibition; that is, the higher the mobility, the lower the level of product inhibition. It is possible that the high degree of product inhibition seen in human MnSOD is due to the rigidity of the active site environment. One can envision a state of catalysis in which the product-inhibiting moiety is bound in the active site, possibly in an end-on state as is observed for the MnSOD inhibitor azide (Lah *et al.*, 1995). In this position the Mn and the hydroxyl of Tyr34 would coordinate this moiety. A more static environment may lead to the stabilization of this intermediate, which kinetically would be observed as an decrease in the gating ratio ($k_3 > k_2$) and/or a decrease in k_4 . The converse, therefore, would be true for a more dynamic active site, as is observed in the lesser product inhibited enzymes, *E. coli* and F66L human MnSOD. Recall that the major difference between these two wild-type enzymes is the level of quaternary structure. It has been shown that the tetrameric organization of human MnSOD acts to stabilize the enzyme. This stabilization can be correlated to a more rigid protein, suggesting that part of the reason for the increased product inhibition of human MnSOD is due to the higher level of quaternary organization.

Additional evidence for the effects of changes in the solvent network on catalysis is provided by previous studies examining solvent hydrogen isotopes effects (SHIE). In a study by Hearn *et al.* (2001), it was shown that the rate of formation of H_2O_2 along the inhibited pathway (k_4) has a very large SHIE, indicating a role for proton transfer during this step. Compared to wild-type human MnSOD, the two mutants and *E. coli* enzyme have a significantly decreased rate, k_4 (Table 3-2). The higher degree of disorder in the

active sites of these three enzymes agrees with this, in that there would be a loss of support for proton transfer in a disordered system.

Conclusions

The active site environment of the MnSODs has been shown to be vital for efficient catalysis. Mutational analysis of Phe66 in human MnSOD has demonstrated a possibility to alter the kinetic properties of the enzyme, particularly in the formation and release of the product-inhibited state. Both F66A and F66L mutants demonstrated lower rates of activity at all stages of catalysis. Additionally, F66L provided an enzyme with a significant decrease in the extent of product inhibition with only a minor decrease in the rate of the first stage of the reaction. Thus, this enzyme has characteristics more similar to the *E. coli* enzyme. Through crystallographic B-factor analysis, it was also shown that both enzymes, as well as *E. coli* MnSOD, have a more dynamic solvent structure in the active site pocket. Proton transfer in these enzymes may be impeded as a result of the increased mobility of solvent molecules along the proposed proton wire. Also, this dynamic nature leads to the conclusion that the mobility of the active site solvent correlates directly with the extent of product inhibition, with less dynamic enzymes stabilizing the product-inhibited intermediate state.

Table 3-1. X-ray diffraction data processing and structure refinement statistics for F66A and F66L human MnSOD

Parameter	F66A	F66L
Space group	<i>P6₁22</i>	<i>P6₁22</i>
Unit cell parameters (Å)	<i>a</i> = 81.2, <i>c</i> = 242.8	<i>a</i> = 81.1, <i>c</i> = 242.5
Resolution (Å)	20-2.2 (2.28-2.20) ^a	20-2.5 (2.59-2.50)
Redundancy	5.2 (3.7)	3.1 (2.8)
Completeness (%)	93.5 (90.7)	92.6 (90.4)
R _{sym} ^b (%)	8.0 (17.0)	7.3 (13.1)
I/σ(I)	31.2	38.4
R _{cryst} ^c (%)	19.5	19.9
R _{free} ^d (%)	21.7	20.6

No. of protein atoms	3097	3103
No. of water molecules	136	142
rmsd for bond lengths (Å)	0.008	0.007
rmsd for bond angles (°)	1.4	1.3
Average B-factors (main/side/solvent)	24.5/27.7/33.1	22.8/25.5/24.1

^a Data in parentheses are for the highest resolution shell. ^b $R_{\text{sym}} = (\sum |I - \langle I \rangle| / \sum \langle I \rangle) \times 100$. ^c $R_{\text{cryst}} = (\sum ||F_o| - |F_c|| / \sum |F_o|) \times 100$. ^d R_{free} is calculated the same as R_{cryst} , except with 5% of the data omitted from refinement.

Table 3-2. Rate constants for catalysis by wild-type and mutant human and *E. coli* MnSOD obtained by pulse radiolysis

Enzyme	k_1 ($\mu\text{M}^{-1} \text{s}^{-1}$)	k_2 ($\mu\text{M}^{-1} \text{s}^{-1}$)	k_3 ($\mu\text{M}^{-1} \text{s}^{-1}$)	k_4 (s^{-1})
Wild-type human ^a	1500	1100	1100	120
F66A ^b	600	500	700	82
F66L ^b	700	800	200	40
Wild-type <i>E. coli</i> ^c	1100	900	200	60

^a From Hearn *et al.*, 2001. ^b In 2 mM HEPES (pH 8.0), 50 μM EDTA, and 30 mM formate at 25 °C. Experimental uncertainties in rate constants are no greater than 15%. ^c From Abreu *et al.*, 2007.

Table 3-3. Geometric distances with the active site of wild-type, F66A, and F66L human and wild-type *E. coli* MnSOD as illustrated in Figure 3-7.

distance	wild-type human	F66A	F66L	wild-type <i>E. coli</i>
d _{2A}	2.8 ^a	3.0	3.0	3.2
d _{2B}	2.9	2.7	3.3	2.6
d _{2AB}	2.9	4.0	3.8	2.7
d ₃₀	2.6	2.9	2.9	2.8
d ₁₆₆	2.7	2.6	2.6	2.6

^a Distances are in angstroms.

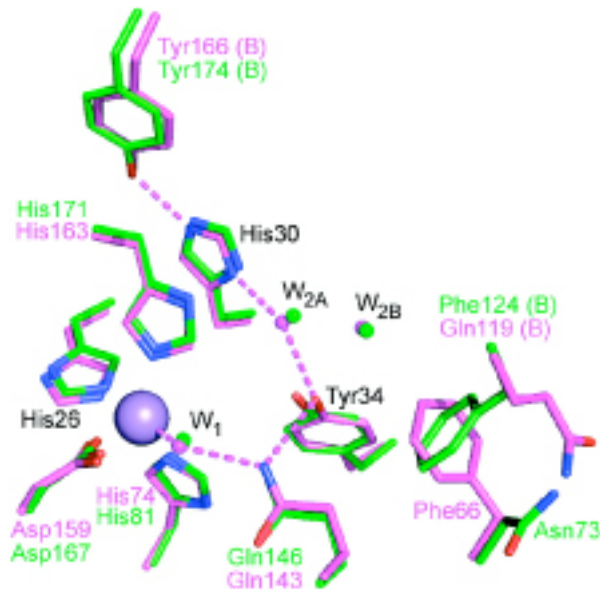


Figure 3-1. Superposition of the active sites of human (magenta) (Hearn *et al.*, 2003) and *E. coli* MnSOD (green) (Borgstahl *et al.*, 2000) shows the high degree of similarity in the active site. The manganese is shown as a purple sphere with the ordered solvent molecules shown as small spheres. A “(B)” following the residue label indicates that the residue belongs to the neighboring monomer. Text color correspond to the enzyme color, black text indicates that the residue type and number is the same in both enzymes.

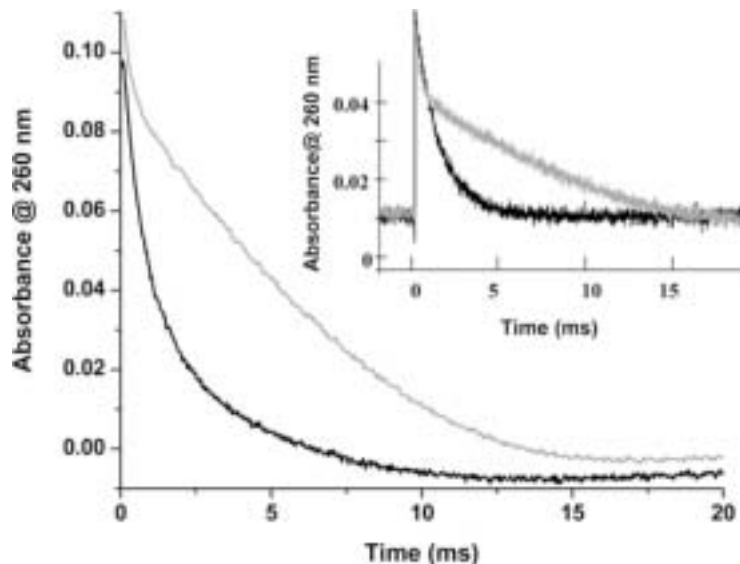


Figure 3-2. Output from pulse radiolysis studies shows the decrease in absorbance at 260 nm over the course of the reaction demonstrating the zero-order phase of catalysis seen in F66A and wild-type human MnSOD. In the foreground is shown F66A (gray) and F66L (black) catalytic progressions. The inset shows the same reaction for wild-type human (gray) and *E. coli* (black). The zero-order (linear) phase is clearly seen in F66A and wild-type human MnSOD after about 1 ms. The initial superoxide concentration was 10 μM and enzyme was at 1 μM .

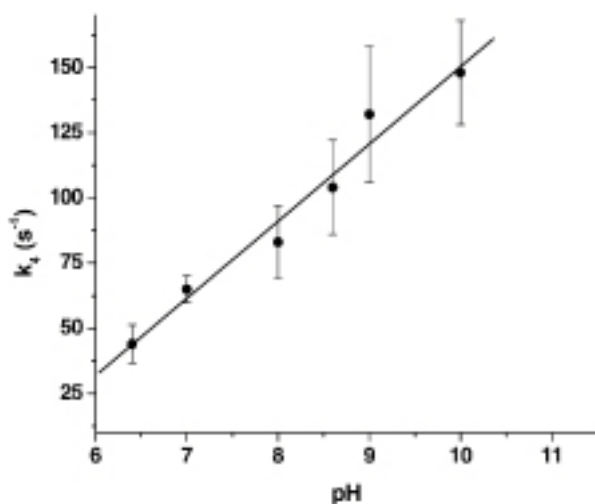


Figure 3-3. The pH dependence of k_4 in catalysis by F66A human MnSOD. The data shown are the average of between 3 and 5 experiments. The reaction conditions were 30 mM sodium formate, 50 μ M EDTA, and buffer at 2 mM (HEPES at pH 6.4-7.9, TAPS at pH 8.0-8.8, CHES at pH 8.9-10.9). Note that the error in measurement increases with pH.

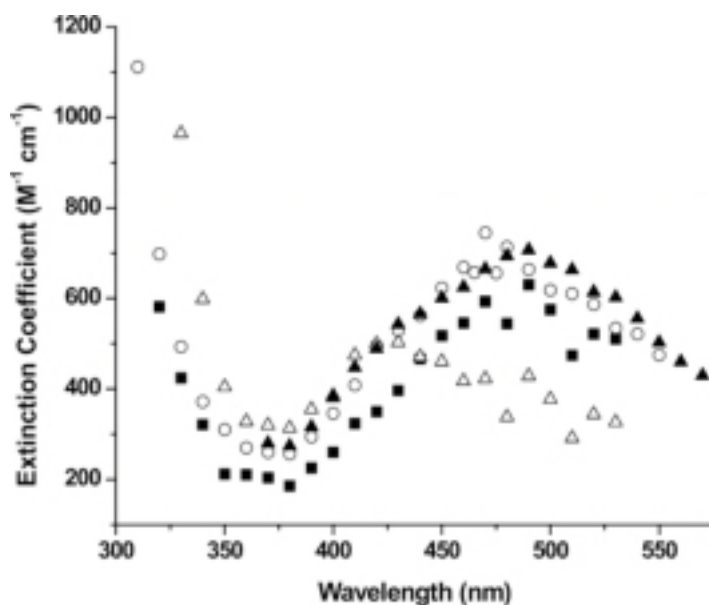


Figure 3-4. Spectroscopic evidence of the formation of an inhibited complex in wild-type human MnSOD. The formation of the product-inhibited state occurs over short time scales (0.2-1.0 ms) in human MnSOD (Δ) as illustrated by the decrease in extinction coefficient at 480 nm. This inhibited state was not seen on longer time scales in the same enzyme (>50 ms) (\blacksquare) indicating a return to the Mn^{3+} state. There was no distinguishable formation of the product-inhibited state observed in either E. coli (\circ) or F66L (\blacktriangle) human MnSOD on the short time scale.

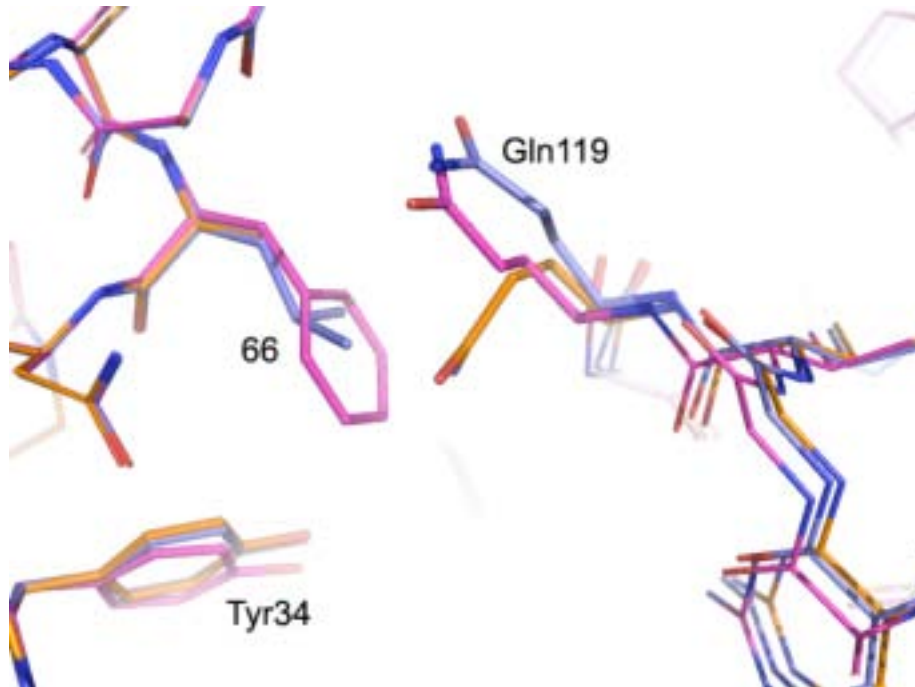


Figure 3-5. The effects of mutations at Phe66 in human MnSOD are clearly visible at position 119 when compared to wild-type (magenta) (Hearn *et al.*, 2003). The glutamine at this position shifts outward in the F66L mutant (blue), due to a steric clash with the $\delta 1$ carbon of the leucine. Removal of the phenyl ring by mutation to alanine (F66A, orange) allows the side chain of Gln119 to rotate towards the active site, bending by about 90° at the γ carbon. Also notice the slight outward movement of Tyr34 observed in both mutant structures.

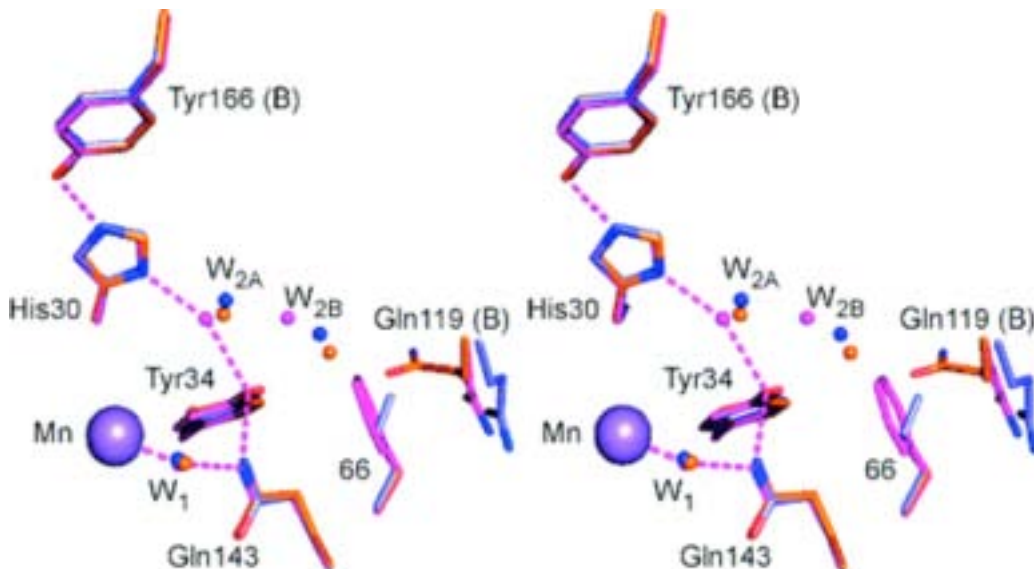


Figure 3-6. A stereoscopic view of the active site environment of human MnSOD and its mutants F66A and F66L. The manganese ion is shown as a purple sphere and the water molecules as small spheres colored according to the structure to which they belong (wild-type = magenta, F66A = orange, F66L = blue). Notice the change in the positions of the water molecules W2A and W2B.

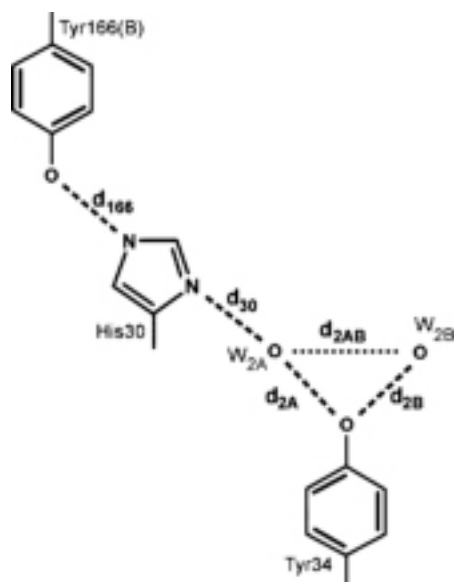


Figure 3-7. A diagrammatic representation of the geometry of the active site of the MnSODs with the distances presented in Table 3-3 defined with dashed lines. The finely dashed line for d_{2AB} indicates that this is most likely not a hydrogen bonding interaction, as the distance is generally too long.

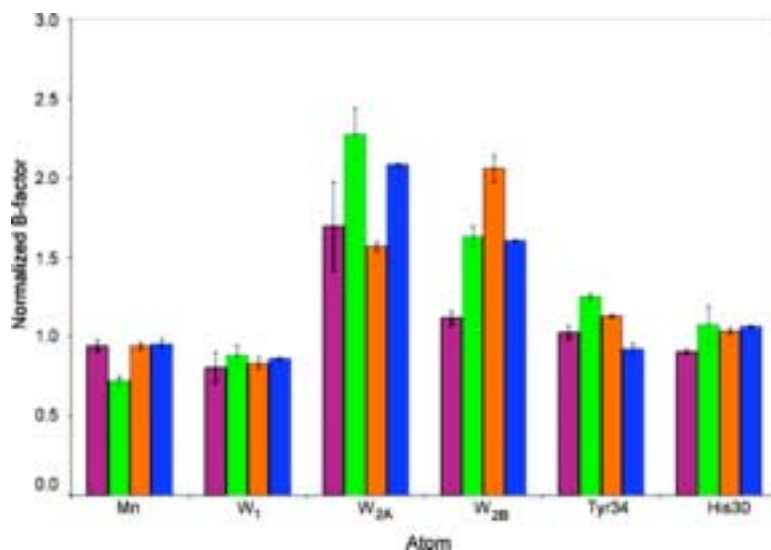


Figure 3-8. A histogram showing the normalized B-factors of the atoms located in the active site of MnSOD. Shown here are the B-factors for wild-type human (magenta) (Hearn *et al.*, 2003), wild-type *E. coli* (green) (Borgstahl *et al.*, 2000), F66A (orange), and F66L (blue). The values given for Tyr34 and His30 are those of the average normalized B-factor for the entire side chain. Normalization was performed against the average B-factor for a selection of main chain atoms as described in the Results section. Error bars represent the normalized standard deviations across independently refined monomers from the same structure.

CHAPTER 4 SEQUESTRATION OF SUBSTRATE CARBON DIOXIDE IN THE ACTIVE SITE OF HUMAN CARBONIC ANHYDRASE II

The previous two chapters have focused on the enzyme manganese superoxide dismutase and the role of amino acids near the active site in modulating the enzyme's activity. It was shown that the manganese ion at the active site center is finely tuned by second shell ligands and that product inhibition may be lessened by a more mobile active site. The following chapters will extend active site analysis to another class of enzymes, the carbonic anhydrases (CA). The CAs utilize a mechanism that does not involve a redox reaction, as the metal at the center is typically a zinc. This chapter examines the binding of substrate in the active site of human CA II (HCA II), and it is shown that the active site residues are very static and that this is beneficial for rapid catalysis (Domsic *et al.*, 2008; Domsic & McKenna, 2009).

Introduction

HCA II is a very efficient enzyme, with rates approaching the diffusion-controlled limit ($k_{\text{cat}} \sim 10^6 \text{ s}^{-1}$, $k_{\text{cat}}/K_M \sim 10^8 \text{ M}^{-1} \text{ s}^{-1}$). The reaction catalyzed is the reversible hydration of carbon dioxide to form bicarbonate and a proton. As discussed in Chapter 1, the reaction is two-step with the hydration occurring in the first step, resulting in a zinc-bound water. The transfer of a proton in the second step regenerates a catalytically ready zinc-bound hydroxide. It is the active site make up of HCA II that allows it to accept a hydrophobic substrate on one side and form a solvent-mediated proton wire on the other side. The entrance to the active site is about 15 Å wide at the surface of the protein, tapering down in a roughly conical fashion to the zinc ion. It is the cavity formed by this cone that provides both hydrophobic and hydrophilic environments, divided nearly in half at the zinc (Figure 4-1). The atoms of the

hydrophilic half are responsible for forming the proton wire and include Tyr7, Asn62, His64, Asn67, Thr199-O^{Y1}, and Thr200-O^{Y1} (Figure 4-1) (Tu *et al.*, 1989; Jackman *et al.*, 1996; Fisher *et al.*, 2005). Direct structural analysis of hydrophobic substitutions at positions 62 and 67 (N62L and N67L) have shown that these mutations affect the ability of the protein to form an active proton wire, resulting in drastically reduced rates of proton transfer (Fisher *et al.*, 2007).

The hydrophobic half is made up of atoms including Val121, Val143, Leu198, Thr199-CH₃, Val207, and Trp209. It has been suggested by molecular dynamics studies that this half is important for binding carbon dioxide (Liang & Lipscomb, 1990; Merz, 1991). Also, mutational analysis has shown that increasing the bulk of the side chain at position 143 has a deleterious effect on catalytic activity (Fierke *et al.*, 1991; Alexander *et al.*, 1991). However, there has been little direct structural evidence for the mechanics of the first part of the reaction, specifically the binding of substrate. It has been stated that the low solubility of CO₂ in aqueous solution and the extremely rapid turnover of HCA II-catalyzed CO₂ hydration preclude any structural studies of substrate binding in HCA II (Liang & Lipscomb, 1990). These limitations were overcome by utilizing a high-pressure environment, however, and the structure of CO₂-bound HCA II was solved. The results suggest that the CO₂ passively binds to the hydrophobic half of the active site cavity and that the zinc plays no role in substrate binding, allowing for rapid catalytic turnover (Domsic *et al.*, 2008).

Materials and Methods

Enzymes

Human CA II was expressed in *E. coli* BL21(DE3)pLysS cells by induction with 0.1 mM IPTG for four hours. Following induction, cells were harvested via centrifugation,

frozen overnight, and then lysed in 100 mM Tris, 200 mM sodium sulfate, pH 9.0 with ~1 mg/mL lysozyme. The lysate was clarified and the protein was purified using affinity chromatography on agarose resin coupled with *p*-(aminomethyl)-benzene-sulfonamide (Sigma-Aldrich, St. Louis, MO). Elution was performed with 100 mM Tris, 400 mM sodium azide, pH 7.0. The azide was then removed by extensive dialysis against 10 mM Tris, pH 8.0 and the protein concentrated using centrifugal ultrafiltration.

To test the effects of the zinc on CO₂ binding, a zinc-free, or apo, enzyme was prepared by Balendu Avvaru in the McKenna lab. Briefly, the enzyme was incubated at 20 °C in the presence of the strong zinc chelator, pyridine 2,6 dicarboxylic acid, (100 mM in 25 mM MOPS, pH 7.0). The chelator was then removed by dialysis against 50 mM Tris, pH 8.0 and removal of the zinc was verified by a complete loss of catalytic activity of the sample.

Crystallization

Crystals of the apo and holo enzymes were both obtained using the hanging drop vapor diffusion technique. The reservoir contained 1.3 M sodium citrate and 100 mM Tris pH 8, and trays were placed at room temperature. Crystals appeared within 7 days and grew to approximately .2 mm³.

Carbon Dioxide Trapping

Several considerations had to be made with regards to trapping the CO₂ in the crystals. First, it was necessary that the CO₂ remain in the crystal after treatment and that the catalytic reaction did not take place. Secondly, the low solubility of CO₂ in aqueous solutions precluded the use of CO₂ saturated solutions, as the molarity of CO₂ would be too low to saturate the binding sites in all molecules of the crystal. These issues were solved by utilizing a technique developed in Sol Gruner's laboratory in

which protein crystals were placed under high-pressure helium to “freeze” the crystals without the use of cryoprotectant (Kim *et al.*, 2005). This method involves putting the crystals on loops, ready for data collection, and putting them in high-pressure tubes. The tubes are then filled with helium gas at pressures >100 atm. Once the pressure is reached, the crystals are dropped into a liquid nitrogen bath to prevent boiling of the trapped helium gas. All of this is done remotely with the entire device placed in carbon steel box. This method was modified and performed at much lower pressures for these experiments.

Protein crystals have a very high solvent content (~50% on average), so prior to exposure to CO₂, the crystals were coated with mineral oil. As with the helium method, the crystals were mounted onto nylon loops and placed in the high-pressure tubing. Previous attempts at rapidly plunging the crystals into liquid nitrogen were unsuccessful. Therefore, the crystals were left under 15 atm of CO₂ for 25 minutes at room temperature. After this incubation, the end of the metal tubing was dipped slowly into a liquid nitrogen bath over a 2 min. time course. (The slow cooling required that the crystals be treated with 20% glycerol + reservoir solution prior to treatment.) This allowed for the solidification of the CO₂ gas, as evidenced by a drop to 1 atm in the internal pressure of the tubing. The presence of CO₂ in the crystal on the loop was confirmed by placement of the crystals at room temperature (by blocking the 100 K cryostream) resulting in a “bubbling” of the crystal.

Data Collection and Processing

The crystals were transferred under liquid nitrogen to the goniometer and data was collected at a wavelength of 0.9772 Å on the A1 beamline at Cornell High Energy Synchrotron Source. The crystal to detector distance was set at 65 mm with an

oscillation angle of 1°. To ensure completeness and data validity, a large number of images were collected for both holo and apo enzyme (624 and 360 images, respectively). Diffraction data were then indexed, integrated, and scaled using the program HKL2000 (Otwinowski & Minor, 1997). Crystals of both enzymes diffracted to 1.1 Å resolution with completeness = 99.9% and $R_{\text{sym}} = 8.8\%$ for holo and completeness = 93.1% and $R_{\text{sym}} 8.0\%$ for apo. Complete data reduction statistics are given in Table 4-1.

Structure Refinement

To ensure acceptable structure comparison, both the apo and holo enzyme-CO₂ complex structures were solved in the same manner using the program *SHELXL* (Sheldrick, 2008). Prior to refinement a random 5% of data were flagged for R_{free} analysis (Brunger, 1992). A previously determined HCA II structure was used as the initial model (PDB ID: 2cba, Hakansson *et al.*, 1992). Before any fitting, though, all heteroatoms and alternate conformations were deleted from the structure.

The initial round of refinement was least squares, rigid-body fitting at 2.5 Å resolution. This resulted in $R_{\text{factor}}/R_{\text{free}}$ of 33.3/33.2% for holo and 28.0/28.6% for apo. The resolution was then extended to 1.5 Å and refinement was switched to the conjugant gradient least squares (CGLS) method. After 20 cycles, the protein model and σ -weighted electron density maps were read into the graphics program *Coot* (Emsley & Cowtan, 2004). All side chain positions were verified manually and the zinc was built into the appropriate density in the holo structure. In the next cycle of CGLS refinement, water molecules were added and then checked manually against the generated electron density maps. Data was then extended to 1.1 Å resolution and more water molecules were added. After all waters were satisfactorily added the carbon

dioxide molecule(s) were added in the appropriate density. Leaving the CO₂ molecules out ensured that any density observed was not an artifact of model bias, but rather was due to the unaccounted presence of substrate. All alternate conformations were then modeled in followed by the addition of riding hydrogens (at all positions except histidines). The final round involved increasing the weighting factor to 0.2. The final $R_{\text{factor}}/R_{\text{free}}$ was 10.9/12.9% for holo and 10.4/13.9% for apo. Complete refinement statistics can be found in Table 4-1. Geometries of the structures were then analyzed in *PROCHECK* (Laskowski *et al.*, 1993).

Results

Carbon Dioxide in the Active Site

Carbon dioxide was found bound in both the holo and apo HCA II structures, located on the hydrophobic half of the active site (Figure 4-2). The high-pressure environment and binding of CO₂ had negligible effects on the overall structure of the enzyme as compared to wild-type (PDB ID: 2ili; Fisher *et al.*, 2007), with an overall C^α rmsd of 0.21 Å for holo and 0.15 Å for apo. It was assumed that the CO₂ molecules in the holo and apo structures were at full occupancy and, as such, refined with average B-factors of 10.90 and 10.35 Å², respectively (comparable with neighboring protein atoms) (Table 4-1).

The CO₂ molecule lies within 4 Å of residues Val121, Val143, Leu198, and Trp209 (Figure 4-2, Table 4-2). The location of CO₂ displaces an ordered water molecule termed the “deep water” (W_{DW}) that has been observed in many other HCA II structures. In the holo structure, one of the CO₂ oxygens, O(1), interacts with the amide of Thr199 with a distance of 3.5 Å between the atoms. The other CO₂ oxygen, O(2), is positioned between the zinc ion and the side chain of Val121. Due to these interactions, the CO₂

molecule is placed in a side-on orientation with respect to the zinc, with both CO₂ oxygens nearly equidistant from the zinc-bound solvent (~3.1 Å). This positions the carbon 2.8 Å from the zinc-bound solvent. There is also a new, well-ordered water molecule observed in a position that has not been observed in crystal structures of HCA II, which was termed the intermediate water (W_I). W_I is located between Thr200-O^{Y1} and the O(2) oxygen of CO₂. A list of interactions and the associated distances can be found in Table 4-2.

Despite the absence of zinc, the geometry of the CO₂ molecule in the apo structure is nearly identical to that of CO₂ in the holo structure. The position that would normally be occupied by zinc is occupied by a water molecule, with the atom center shifted ~0.6 Å closer to the histidine ligands (Figure 4-2 B). The distance between this water and the CO₂ oxygens is still ~3.1 Å. Therefore the CO₂ has shifted position slightly, pivoting about its O(2) oxygen, into a closer interaction with the amide nitrogen of Thr199. Its interaction distance is now 3.15 Å versus a distance of 3.5 Å observed in the holo structure (Figure 4-2).

A Second Carbon Dioxide Binding Site

Electron density corresponding to a carbon dioxide molecule was also found in another portion of the protein. This location is a hydrophobic pocket situated roughly 11 Å away from the active site (Figure 4-3). The binding of CO₂ in this location displaces the phenyl ring of Phe226, causing the ring to tilt approximately 30°. An additional residue in this pocket, Trp97, has been shown to act as a nucleation site for protein folding (Jonasson *et al.*, 1997).

Additional Protein Structural Features

The tilting of the side chain of Phe226 was the largest change observed in the CO₂-bound structures, when compared to wild-type HCA II. A large number of alternate conformations were observed in the holo and apo structures, a common feature of high-resolution crystal structures. In the holo structure alternate conformations were seen for Ile22, Leu47, Ser50, Asp52, His64, Ser152, Ser217, and Val223. For the apo structure, alternate conformations were seen at Ile22, His64, Gln103, Asp162, Lys172, Glu214, Ser217, and Val223. The two conformations seen for His64 have been observed before and are termed the “in” and “out” conformations, with the “in” conformation being the typically preferred orientation (Silverman & McKenna, 2007; Fisher *et al.*, 2007). In the CO₂-bound holo and apo structures, the “out” conformation was favored. The presence of a glycerol molecule adjacent to His64 caused this preference, with the oxygens of the glycerol positioned where the ordered proton wire would normally be observed (Figure 4-4 A). Glycerol was also observed in both structures near residues 243-245 on the surface of the protein (Figure 4-4 B).

Discussion

Trapping Carbon Dioxide

The rate of CO₂ hydration catalyzed by HCA II ($10^8 \text{ M}^{-1} \text{ s}^{-1}$) approaches the diffusion-controlled limit, with a rate-limiting proton transfer step that brings the maximal turnover to 10^6 s^{-1} . This high level of catalysis dictates that the substrate be bound loosely and is reflected by the K_M of HCA II, 10 mM. Infrared spectroscopic measurements also suggest that HCA II has a weak affinity for CO₂, with a calculated K_D of 100 mM (Krebs *et al.*, 1993). Overall, the weak binding of CO₂ coupled to the high turnover rate of HCA II suggests that trapping substrate would be nearly impossible.

The success of these experiments can be explained by the physical and chemical properties of this substrate and enzyme. Firstly, the large hydrophobic pocket in HCA II provides an excellent environment for CO₂ solvation, allowing for the selective solubilization of CO₂. Also, the constant of Henry's Law, for CO₂ solubility, confirms that the concentration of CO₂ in the high-pressure experiments (15 atm) is 450 mM, nearly 5 times the K_D (Butler, 1982). Additionally, the catalytic activity of the enzyme was hindered by two factors. Firstly, by lowering the temperature to 100 K, catalysis was negligible because the energy barrier for HCA II-driven catalysis is 10 kcal mol⁻¹. Secondly, the CO₂ pressurization at room temperature likely acidified the crystal, thereby protonating the zinc-bound hydroxide, effectively negating any enzymatic activity towards CO₂. Taken together, this information suggests that, under these conditions, complete occupancy in the holo and apo HCA II crystals would be expected.

Physiological Relevance

Previous biochemical studies suggest that the CO₂ binding site described in these crystal structures is physiologically relevant, and not an artifact of the pressurization used for substrate trapping. Mutational analysis of the hydrophobic pocket, specifically at Val143, indicated that bulky side chain substitutions at this position led to drastically reduced catalytic activities (Fierke *et al.*, 1991, Alexander *et al.*, 1991). For example, mutation to tyrosine (V143Y) resulted in an enzyme that had only 0.02% of the activity of wild-type HCA II (Fierke *et al.*, 1991). The crystal structure of V143Y HCA II showed that the side chain of Tyr143 juts into the active site, effectively removing the hydrophobic pocket. Structural superposition of CO₂-bound holo-HCA II with the V143Y structure (overall C^α rmsd = 0.26 Å) clearly shows that the side chain of Tyr143 would

directly block the observed CO₂ binding site, thereby negating any catalytic activity (Figure 4-5).

Further evidence is provided by structural analysis of CO₂-analog inhibitors of HCA II. In one study, the binding of the potent, isoelectronic HCA II inhibitor thiocyanate (NCO⁻) was observed crystallographically (Lindahl *et al.*, 1993). In this case, NCO⁻ binds in the hydrophobic pocket, and does not displace the zinc-bound solvent. The inhibitor also displaces the solvent molecule W_{DW}, forming a hydrogen bond with the amide nitrogen of Thr199. The distances between atoms in the active site and the inhibitor are very similar to those observed in the CO₂-bound structures. The carbon of NCO⁻ is 2.4 Å from the zinc-bound solvent, similar to the CO₂ carbon's distance from the zinc-bound solvent (2.8 Å).

NMR and IR studies of CO₂ binding have, previously suggested the lack of a role for the zinc ion in CO₂ binding, as suggested by a comparison of the CO₂-bound holo and apo structures (Bertini *et al.*, 1987; Williams & Henkens, 1985). It should be noted that, in these studies, the zinc was replaced with either copper or cobalt, since zinc is not paramagnetic. As will be discussed later, these studies also suggested that the product, bicarbonate, is coordinated directly to the metal.

Implications For the Catalytic Mechanism

The position of the CO₂ molecule in the hydrophobic pocket and its direct interaction with the amide nitrogen of Thr199 optimally orient the CO₂ carbon for nucleophilic attack by the zinc-bound hydroxide. The subsequent formation of bicarbonate results in the formation of a bidentate Zn-HCO₃⁻ complex as was proposed by Lindskog (1983) (Figure 4-6). The structure of bicarbonate-bound HCA II was obtained previously by creating a mutation, T200H, which resulted in a greater affinity

for bicarbonate (Xue *et al.*, 1993). A comparison of this structure with that of CO₂-bound holo HCA II shows that the CO₂ lies nearly in plane with the bicarbonate (Figure 4-7). This suggests that these structures represent the beginning and end points of CO₂ hydration.

The release of bicarbonate is facilitated by the diffusion of a water molecule into the active site. The presence of a never before seen water, W_I, in close proximity to the zinc suggests that W_I may be a bicarbonate-displacing water. W_I may not be a new water, but rather the location of W_{DW} when substrate is bound. The binding of CO₂ may have local electrostatic effects, therefore allowing the displaced W_{DW} to occupy a previously unfavorable position. However, the presence of a glycerol at the proton wire obfuscates this analysis.

Conclusions

The challenges of trapping substrate carbon dioxide in the active sites of one of the fastest enzymes known were overcome by a combination of pressurization and low temperatures. X-ray crystal structures of both holo (with zinc) and apo (without zinc) HCA II in complex with CO₂ revealed that the hydrophobic pocket on one side of the active site is responsible for substrate capture due to a more favorable CO₂ solvating environment. The binding of substrate occurs in a passive manner, with no changes in local protein conformation, and the rearrangement of only one water molecule. The lack of change illustrates the ephemeral nature of substrate binding, which allows for rapid turnover (10⁸ s⁻¹). Despite the apparent static nature of the hydrophobic pocket, it still plays a role in placing the substrate for efficient catalysis. Optimal orientation of CO₂ is provided by the amide nitrogen of Thr199, allowing for subsequent nucleophilic attack by the zinc-bound hydroxide. Furthermore, the observation of a second, non-productive

CO₂ binding site in another hydrophobic pocket suggests that this method may be used to probe hydrophobic structures in other proteins, providing insights into protein folding and catalytic mechanisms.

Table 4-1. Data collection and refinement statistics for the CO₂-bound holo and apo HCA II structures.

Parameter	Holo	Apo
Space group	P 2 ₁	P 2 ₁
Cell dimensions		
a, b, c (Å)	42.4, 41.5, 72.4	42.2, 41.5, 72.3
α, β, γ (°)	90.0, 104.1, 90.0	90.0, 104.2, 90.0
Resolution (Å)	20-1.1 (1.12-1.10) ^a	20-1.1 (1.12-1.10)
R _{sym} ^b (%)	8.8 (51.9)	8.0 (50.6)
I/(σ)I	21.0 (4.1)	35.6 (4.3)
Completeness	99.9 (100.0)	93.1 (89.7)
Redundancy	11.4 (10.8)	7.0 (5.8)
No. reflections	98,494	86,919
R _{factor} ^c /R _{free} ^d (%)	10.90/12.89	10.35/13.87
No. atoms		
Protein	2096	2121
Zinc/CO ₂ /glycerol	1/6/12	0/6/6
Water	404	352
B-factors		
Protein (main/side)	10.4/15.2	11.1/15.6
Zinc/CO ₂ ^e /glycerol	5.1/14.0, 39.5/20.1	NA/15.7, 59.7/19.1
Water	31.7	29.4
Ramachandran plot (%)		
Allowed	89.4	88.9
Additionally allowed	10.2	10.6
Generously allowed	0.5	0.5
rmsd ^f	0.192	0.144

^a Values in parentheses are for the highest resolution shell. ^b $R_{sym} = (\sum |I - \langle I \rangle| / \sum \langle I \rangle) \times 100$. ^c $R_{cryst} = (\sum ||F_o| - |F_c|| / \sum |F_o|) \times 100$. ^d R_{free} is calculated the same as R_{cryst} , except with 5% of the data omitted from refinement. ^e The first number is for the active site CO₂, the second is for the CO₂ in the non-catalytic site. ^f The root mean square deviation when the respective structure is superimposed on the 1.1 Å structure of wild-type HCA II (Fisher *et al.*, 2007), using only C^α positions.

Table 4-2. Distances between atoms in the structures of CO₂-bound holo and apo HCA II. The distances shown are only for those atoms that lie within 3.9 Å of the CO₂ molecule. The second atom in each row corresponds to the CO₂ molecule. For information on CO₂ atom naming, refer to Figure 4-7.

Interaction	Holo	Apo
Zn-bound H ₂ O – C	2.8	N/A
H ₂ O – C ‡	N/A	2.9
Zn-bound H ₂ O – O(1)	3	N/A
H ₂ O – O(1)	N/A	3.1
Zn-bound H ₂ O – O(2)	3.1	N/A
H ₂ O – O(2)	N/A	3.1
Zn ²⁺ – O(1)	3.2	N/A
His94(C ^{ε1}) – O(1)	3.3	3.2
Leu198(C ^α) – O(2)	3.4	3.5
His119(N ^{δ1}) – O(1)	3.4	3.5
Thr199(N) – O(2)	3.5	3.2
W ₁ – O(2)	3.5	3.2
His119(C ^β) – O(1)	3.5	3.6
Val121(C ^{γ2}) – O(1)	3.5	3.4
Trp209(C ^{ζ2}) – O(2)	3.5	3.3
W ₁ – C	3.6	3.2
His94(N ^{ε2}) – O(1)	3.6	3.5
His119(C ^{γ1}) – O(1)	3.7	3.8
Leu198(C ^{δ2}) – O(2)	3.7	4.1
Zn ²⁺ – C	3.7	N/A
Val143(C ^{γ1}) – O(1)	3.7	3.8
Trp209(C ^{η2}) – C	3.9	3.9
Trp209(C ^{ζ2}) – C	3.9	3.9

‡ H₂O is the water molecule that occupies the site of the zinc ion in CO₂-bound apo HCA II

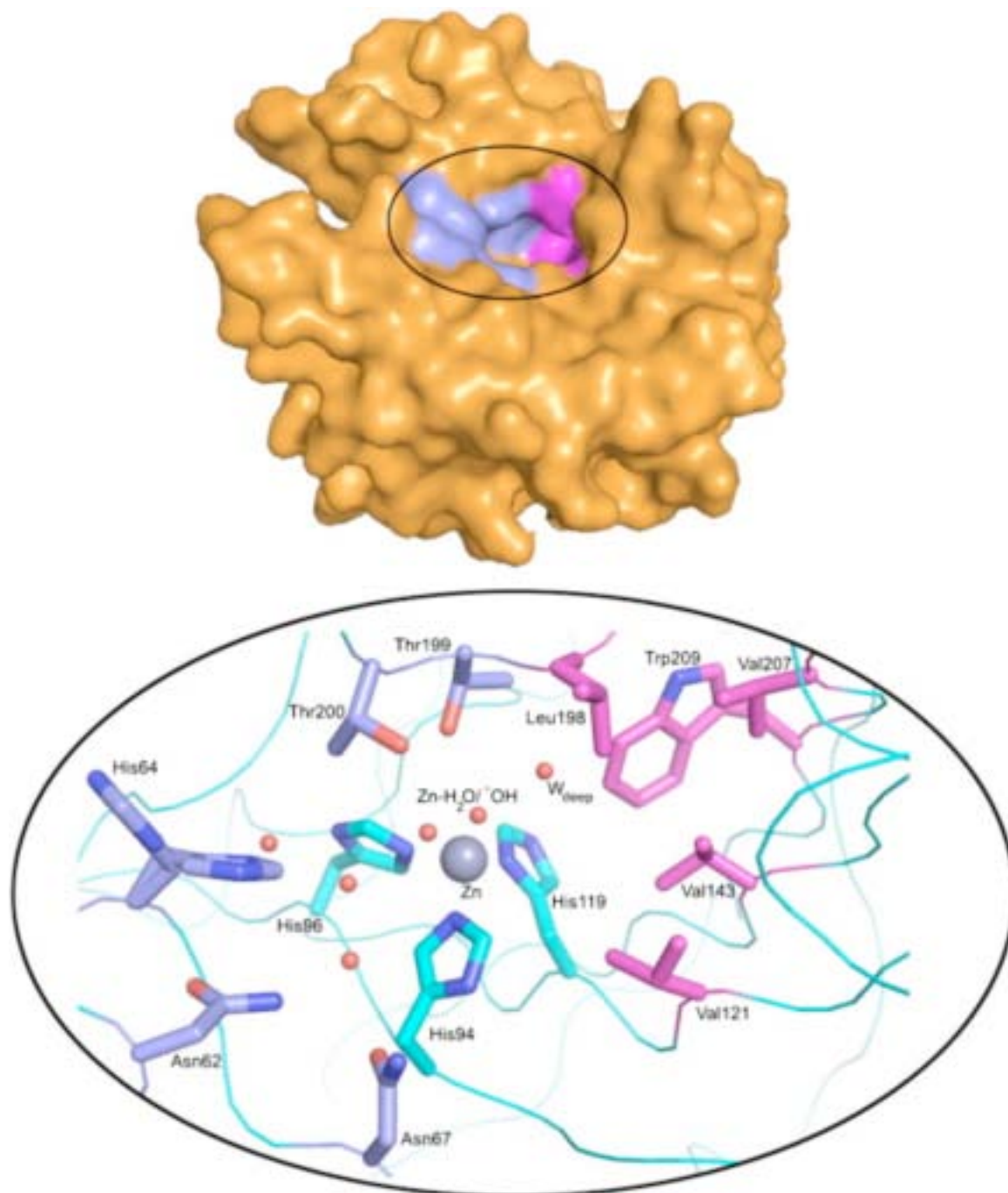
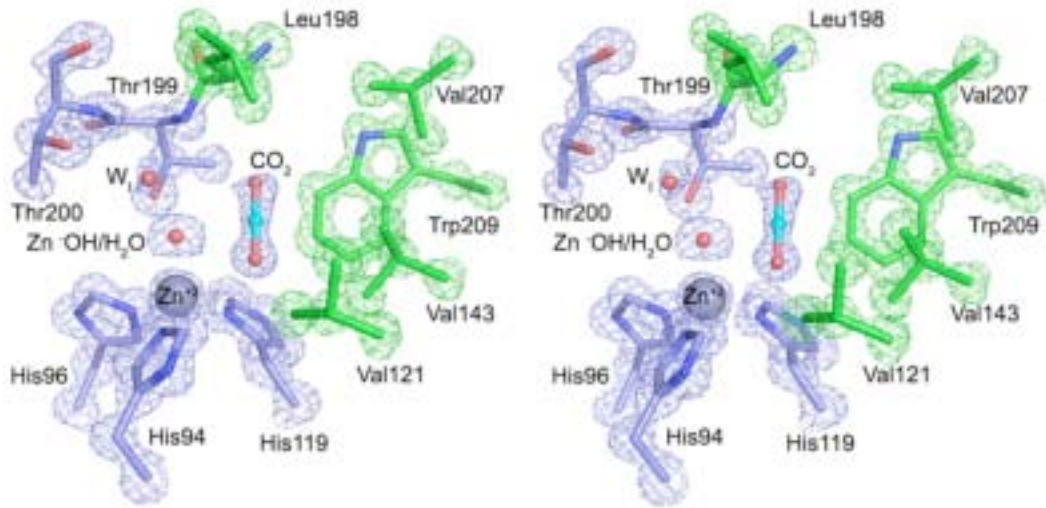
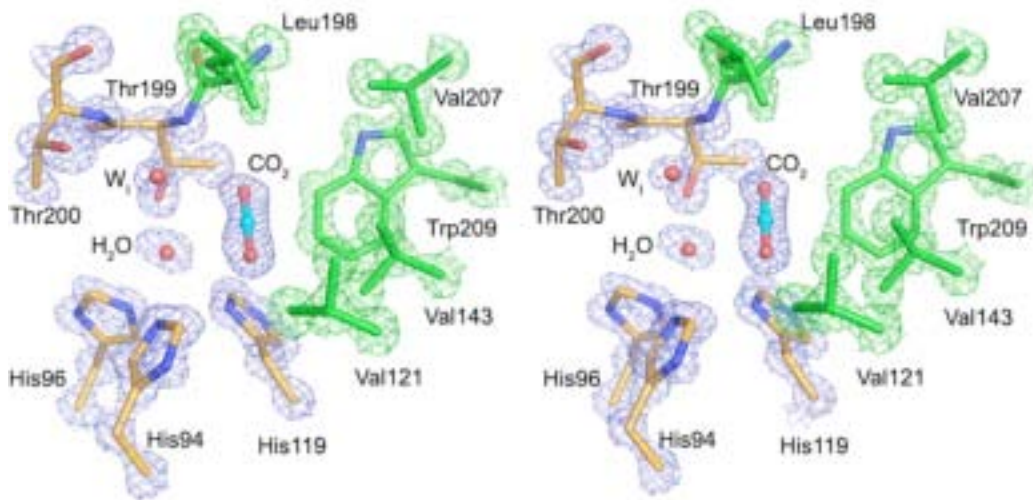


Figure 4-1. The active site of human carbonic anhydrase II is located at the bottom of a conical cavity. On one side is a hydrophilic patch (blue surface, top; blue sticks, bottom) that forms the solvent-mediated proton wire (red spheres, bottom). The other side is lined with hydrophobic residues (magenta surface, top; magenta sticks, bottom). Three histidines (cyan sticks, bottom) and a solvent molecule coordinate the zinc.



A



B

Figure 4-2. The electron density for the carbon dioxide molecule in both holo (top) and apo (bottom) HCA II is clearly observed in the hydrophobic patch (green mesh and sticks). The electron density shown for the protein and waters is a σ -weighted $2F_o - F_c$ Fourier map. The density for the CO_2 is a σ -weighted $2F_o - F_c$ Fourier map made prior to the modeling of the CO_2 coordinates. Both maps are contoured to 2.25σ .

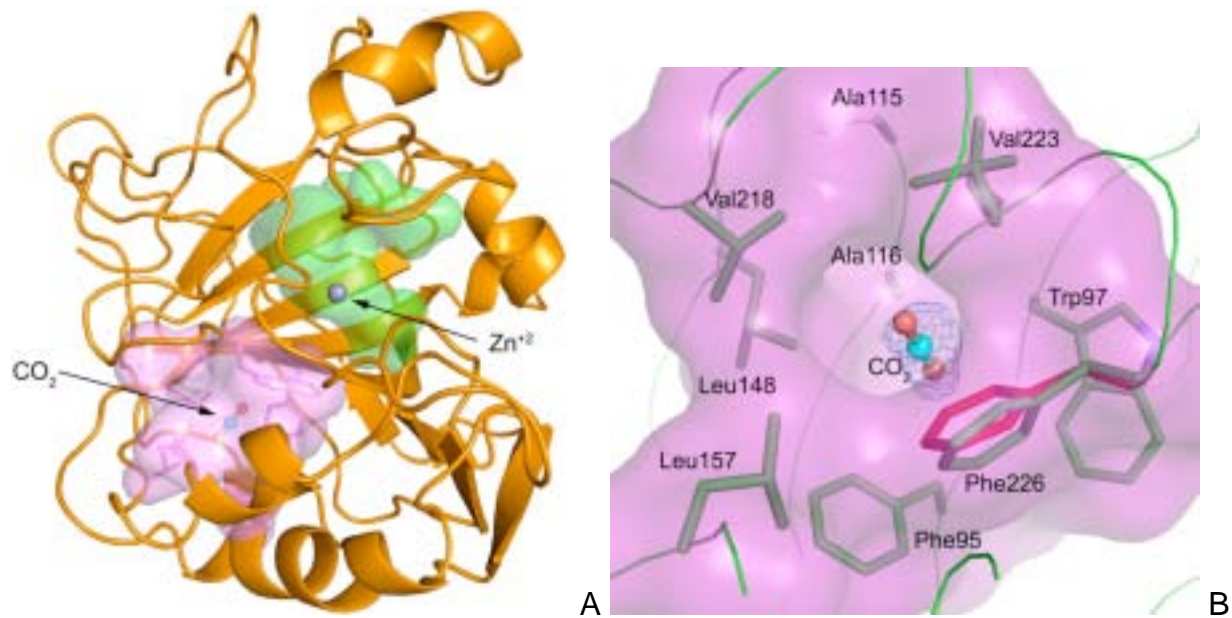


Figure 4-3. The non-catalytic carbon dioxide binding site was found in a hydrophobic patch (magenta surface) on the side of the enzyme opposite the hydrophobic patch (green surface) (A). (B) A close-up of this site clearly shows the CO₂ density (σ -weighted $2F_O-F_C$ at 1.5σ) and the tilting of the side chain of Phe226 (green) compared to its position in wild-type HCA II (red).

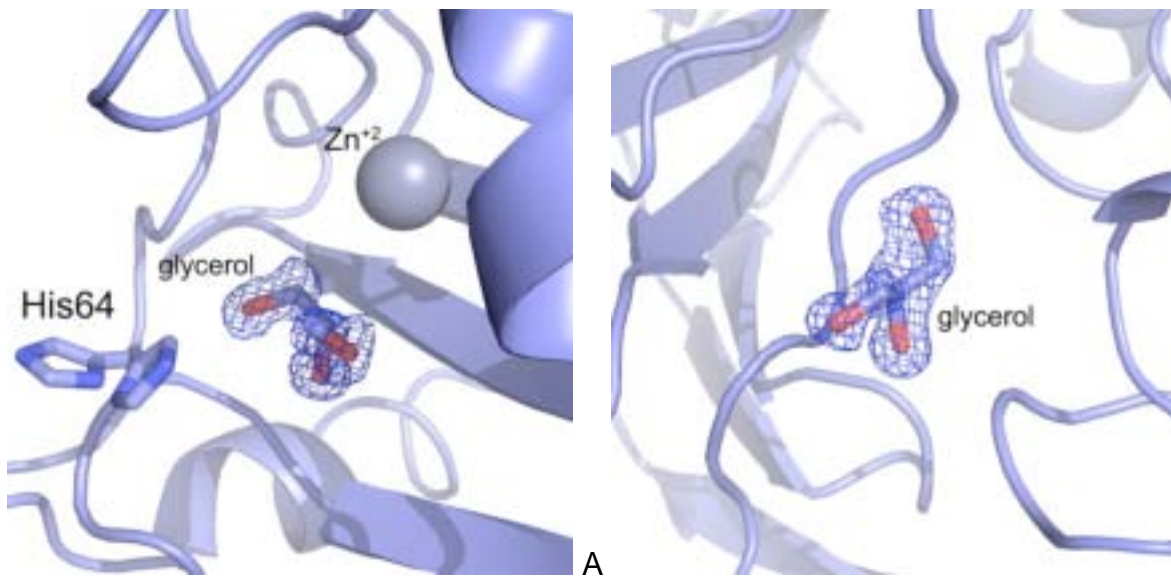


Figure 4-4. Two glycerol molecules were found in the structures of CO₂-bound holo and apo HCA II. (A) A glycerol molecule in the active site of CO₂-bound holo enzyme displaced the proton wire waters. (B) A second glycerol binding site was observed on the surface of CO₂-bound holo enzyme. Both electron density maps are σ -weighted $2F_O-F_C$ at 1.0σ . The structures shown are of the bound holo enzyme, however glycerol molecules were found in the same locations in the bound apo enzyme structure.

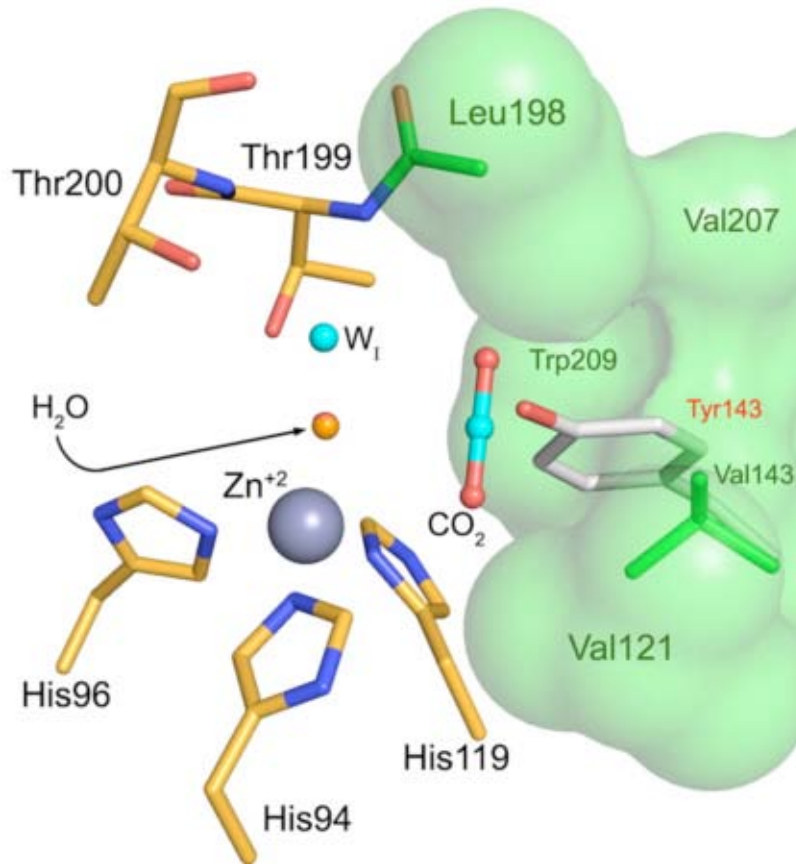


Figure 4-5. A superposition of the CO₂-bound holo HCA II structure with that of V143Y HCA II (Alexander *et al.*, 1991) clearly shows that the side chain of Tyr143 (white sticks) would directly interfere with CO₂ binding (cyan sticks). The hydrophobic patch is shown as a green surface.

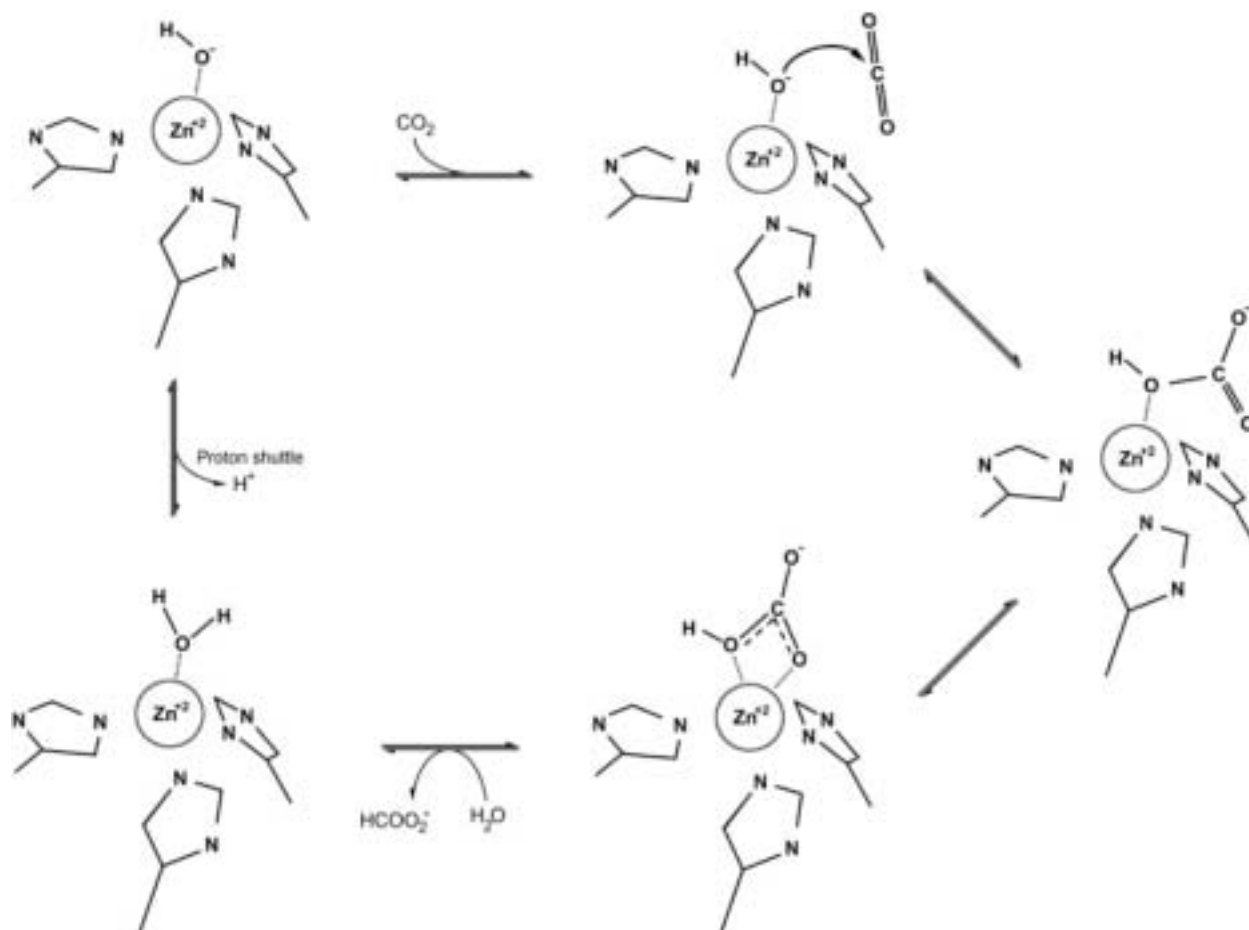


Figure 4-6. The catalytic mechanism of CO₂ hydration as catalyzed by HCA II, as proposed by Lindskog (1983). The enzyme begins with a zinc-bound hydroxide, with an optimally oriented lone electron pair (top left). The binding of CO₂ is followed by nucleophilic attack of the CO₂ carbon by the zinc-bound hydroxide (top middle). This leads to formation of a monodentate bicarbonate-zinc transition state (right). A bidentate zinc-bicarbonate state then forms (bottom right) with the complex dissociating when a water molecule diffuses into the active site and coordinates with the zinc (bottom left). The regeneration of the active zinc-bound hydroxide occurs with the transfer of a proton out of the active site (left).

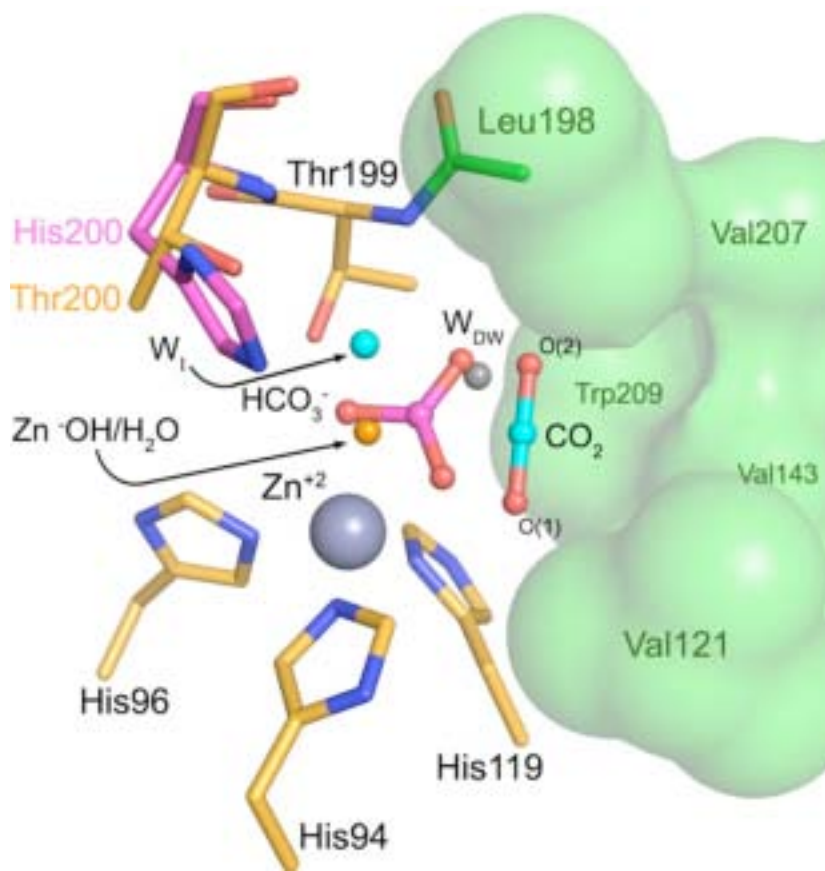


Figure 4-7. The structure of bicarbonate-bound T200H HCA II reveals that the binding site of CO₂ observed in this study is the catalytic site. The CO₂ (cyan sticks) lies nearly in plane with the bicarbonate in the T200H structure (magenta sticks) (Xue *et al.*, 1993). Additionally, it can be seen that the transition of W_I, a water molecule never before seen in HCA2, may in fact be W_{DW} displaced upon CO₂ binding.

CHAPTER 5 THE ROLE OF SURFACE RESIDUES IN PROTON TRANSFER BY HUMAN CARBONIC ANHYDRASE II

The previous chapter discussed the mechanism by which human carbonic anhydrase II (HCA II) captures substrate, carbon dioxide (CO₂). The crystal structures of CO₂-bound holo and apo HCA II demonstrated that the hydrophobic patch on one half of the active site is responsible for this process and that binding of substrate is passive, allowing for rapid turnover. This chapter will discuss the second stage of the reaction, the regeneration of zinc-bound hydroxide by proton transfer. Specifically, the roles of residues forming acidic and basic patches on the surface of HCA II will be examined in terms of their effects on tuning the pK_a of the proton acceptor, His64.

Introduction

As was discussed previously, the reaction catalyzed by HCA II is a two-step cycle. The first step, in the hydration direction, is the hydration of CO₂ to form bicarbonate (eq 1-5). The bicarbonate is then displaced from the zinc when a water molecule diffuses into the active site. A zinc-bound water is inactive for catalysis, so a proton must be transferred off of this water molecule to regenerate a zinc-bound hydroxide, a step that is rate limiting for the overall catalytic cycle (eq 1-6). This is accomplished by an ordered network of solvent molecules that form a hydrogen-bonded wire (Figure 1-5). The end point of this proton wire is His64, which transfers the proton to buffer in bulk solvent. The importance of His64 was revealed by mutational analysis, which showed that an H64A mutation results in a dramatically reduced rate of proton transfer (Tu *et al.*, 1989).

As was discussed in Chapter 1, His64 is known to occupy two conformations: an “in” conformation in which the side chain points toward the zinc and is flanked by two

water molecules of the proton wire (W_{2A} and W_{2B}) with $N^{\epsilon 2}$ 7.5 Å from the zinc, and an “out” conformation with the side chain facing bulk solvent and pi-stacking with the indole ring of Trp5, with $N^{\epsilon 2}$ 12.0 Å from the zinc (Figure 5-1). An earlier x-ray crystallographic study examined the effect of pH on the conformation of His64 (Nair & Christianson, 1991). It was observed that the transition from “in” to “out” occurs as the pH is decreased, indicating that the conformation of His64 is pH sensitive. The sensitivity of His64 to its environment has also been demonstrated by mutational analysis of residues located in other areas of the active site. One study showed that mutation of Asn62 to leucine caused His64 to be in the “in” conformation at pH 6.0 and 8.2 (Fisher *et al.*, 2007). However, in the mutant N67L, His64 was observed in the “out” conformation, independent of pH. Another mutant, Y7F, resulted in an enzyme with a greatly increased rate of proton transfer, and His64 always in the “in” conformation. Interestingly, the pK_a of His64 was determined to be lower when His64 was in the “in” conformation ($pK_a = 6.0$ in Y7F) and was higher when in the “out” conformation ($pK_a = 7.5$ in N67L). Mutation of Thr200, a residue on the opposite end of the hydrophilic pocket, to serine resulted in the observation that His64 was solely in the “out” conformation (Krebs *et al.*, 1991). Interestingly, there were no observed kinetic changes in this enzyme variant as compared to wild-type.

This chapter will discuss the role of an amino acid on the surface of the protein, Lys170, which is situated 4.4 Å from the $N^{\epsilon 2}$ of His64 and 15 Å from the zinc (Figure 5-2). Interestingly, Lys170 shows a high level of conservation across CAs from various species, including rat, chicken, bovine, and turtle. Mutations at Lys170 are shown to

effect the side chain orientation and pK_a of His64. An increased rate of proton transfer is observed in the dehydration direction because of these effects.

Materials and Methods

Enzymes

Mutations at residue 170 (to alanine, aspartate, glutamate, and histidine) were made by site-directed mutagenesis of a plasmid containing the cDNA encoding the human CA II gene using the QuikChange mutagenesis kit (Stratagene, La Jolla, CA). Successful mutagenesis was verified by DNA sequencing (ICBR, University of Florida). Mutated plasmids were then transformed into BL21(DE3)pLysS cells and protein expression was induced by addition of IPTG and zinc sulfate (1 mM final concentration each). The protein was then purified as described in Chapter 4. Purity analysis was performed using SDS-PAGE (data not shown).

Crystallization and Data Collection

All four mutants were successfully purified and crystallized. Crystallization was accomplished using the hanging drop vapor diffusion with a reservoir solution of 1.3 M sodium citrate, 100 mM Tris pH 8. Crystals grew to 0.2 mm^3 within one week. The crystals were then sealed in quartz capillaries and x-ray diffraction data was collected at room temperature using the system discussed in Chapter 2. An oscillation angle of 1° was used with a crystal to detector distance of 100 mm.

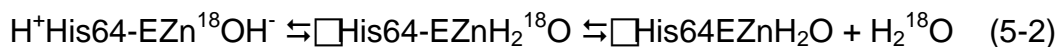
Data Processing and Refinement

Diffraction data were indexed, integrated and scaled using program *HKL2000* (Otwinowski & Minor, 1997). All crystals diffracted to $\sim 1.7 \text{ \AA}$ with isomorphous unit cells (Table 5-1). Model refinement was performed using the program *REFMAC5* in the *CCP4* suite of programs (Collaborative Computational Project, Number 4, 1994;

Murshudov *et al.*, 1997) with the starting model derived from the 1.54 Å structure of wild-type HCA II (PDB ID 2cba, Hakansson *et al.*, 1992), with all hetero atoms removed and Lys170 and His64 mutated to alanine. Refinement was carried out using an initial round of rigid-body fitting, followed by placement of the zinc using the molecular graphics program *COOT* (Emsley & Cowtan, 2004). After a round of restrained refinement, the side chains of residues 170 and 64 as well as waters were placed manually *COOT*. Any difference map density present was modeled appropriately and the structure was refined with *REFMAC5* followed by manual model building in *COOT*. This iterative process was performed until R_{factor} reached convergence. The final R_{factor} for each structure was around 17%. Complete data processing and refinement statistics can be found in Table 5-1.

¹⁸O Exchange

This technique measures the depletion of ¹⁸O from species of CO₂ measured via membrane inlet mass spectrometry (Silverman, 1982). The CO₂ species passing across the membrane enter a mass spectrometer (Extrel EXM-200) thus providing a measure of the isotopic content of the CO₂ species. The dehydration of the labeled bicarbonate has a probability of transiently labeling the active site zinc with ¹⁸O (eq 5-1). The subsequent protonation the zinc-bound hydroxide produces H₂¹⁸O, which is then released into bulk solvent (eq 5-2).



This method provides two rates for CA-catalyzed ¹⁸O exchange. The first is R_1 , the rate of exchange of CO₂ and HCO₃⁻ at chemical equilibrium.

$$R_1/[E] = k^{\text{ex}}_{\text{cat}}[\text{S}]/(K^{\text{S}}_{\text{eff}} + [\text{S}]) \quad (5-3)$$

Here, $k_{\text{cat}}^{\text{ex}}$ is the rate constant for the maximal interconversion of substrate and product, $K_{\text{eff}}^{\text{S}}$ is the apparent binding constant for substrate to enzyme and [S] is the concentration of substrate, either carbon dioxide or bicarbonate. The ratio $k_{\text{cat}}^{\text{ex}} / K_{\text{eff}}^{\text{S}}$ is, in theory and in practice, equal to $k_{\text{cat}}/K_{\text{M}}$ obtained by steady-state methods.

The second rate obtained, $R_{\text{H}_2\text{O}}$, is the rate of release of water that bears ^{18}O from the enzyme. It is this component of ^{18}O exchange that is dependent on the donation of protons to the ^{18}O -labeled zinc-bound hydroxide.

$$R_{\text{H}_2\text{O}}/[E] = k_{\text{B}}^{\text{obs}} [\text{B}]/(K_{\text{eff}}^{\text{B}} + [\text{B}]) + R_{\text{H}_2\text{O}}^0/[E] \quad (5-4)$$

The value of this rate can be interpreted in terms of the rate constant for proton transfer from the proton donor to the zinc-bound hydroxide according to eq 7. In this equation, k_{B} is the rate constant for proton transfer and $(K_{\text{a}})_{\text{donor}}$ and $(K_{\text{a}})_{\text{ZnH}_2\text{O}}$ are the ionization constants of the proton donor and zinc-bound water. To determine the kinetic constant k_{B} and the ionization constants, nonlinear least-squares methods were used in the program Enzfitter (Elsevier-Biosoft, Cambridge, U.K.)

$$k_{\text{B}}^{\text{obs}} = k_{\text{B}}/\{[1 + (K_{\text{a}})_{\text{donor}}/[\text{H}^+]][1 + [\text{H}^+]/(K_{\text{a}})_{\text{ZnH}_2\text{O}}]\} \quad (5-5)$$

The measurement for CA-catalyzed and uncatalyzed ^{18}O exchange were measured at 25°C in the presence of a total substrate concentration of 25mM by Dr. Chingkuang Tu in the Silverman lab. Additionally, the total ionic strength of the solution was kept at 0.2 M by the addition of sodium sulfate.

Esterase Activity

To correctly assign $\text{p}K_{\text{a}}$'s obtained from ^{18}O -exchange, another kinetic assay was performed, which allows assignment of the zinc-bound solvent $\text{p}K_{\text{a}}$. The α -CAs also possess the ability to hydrolyze ester linkages, with no known physiological relevance for this activity (Gould & Tawfik, 2005). To measure this activity, the hydrolysis of 4-

nitrophenol acetate was monitored by UV spectroscopy at 348 nm, the isosbestic point of nitrophenol and its conjugate, nitrophenolate ($\epsilon = 5000 \text{ M}^{-1} \text{ cm}^{-1}$) (Verpoorte *et al.*, 1967).

Results

Catalysis

Mutations at residue 170 in HCA II had little effect on $k_{\text{cat}}/K_{\text{M}}$ of the enzyme, as the pH profiles of all four mutants were nearly superimposable on that of wild-type enzyme (Figure 5-3). It was also found that the $\text{p}K_{\text{a}}$ of the zinc-bound water was approximately 7 in each of the mutants, thus unchanged with respect to wild-type (Table 5-2). This value was also confirmed by independent measurement using the esterase activity assay (Table 5-3).

The catalytic effects of mutation at residue 170 were much more notable for the proton transfer stage of catalysis. As can be seen from the superimposed pH profiles of $R_{\text{H}_2\text{O}}/[\text{E}]$ in Figure 5-4, there is a clear change in this proton transfer dependent rate constant. In this figure, the solid lines represent fits of the data to eq 5-4, with previous knowledge of the $\text{p}K_{\text{a}}$ of the zinc-bound water available from the determination of $k_{\text{cat}}/K_{\text{M}}$ discussed above. This fit provides values for the $\text{p}K_{\text{a}}$ of the proton donor, His64, and the rate constant for proton transfer, k_{B} . One apparent effect of mutation and residue 170 is that the $\text{p}K_{\text{a}}$ of the proton donor, His64, is lowered relative to wild-type. This change is not very dramatic, with values between 6.3 and 6.7 as compared to a value of 7.2 for wild-type. Interestingly, the rate of proton transfer, k_{B} , was increased in all four mutants with values ranging from 1.5 to 5 times greater than wild-type (800 ms^{-1}) (Fisher *et al.*, 2007b; Duda *et al.*, 2001). The final values for the four mutants and wild-type are presented in table Table 5-2.

Structure

The structures of all four mutants were solved to $\sim 1.7 \text{ \AA}$ with final $R_{\text{factor}}/R_{\text{free}}$ of $\sim 17/20 \%$. Overall, no major structural perturbations were observed with C^α rmsd of approximately 0.09 \AA for all four mutants when compared to wild-type. The solvent network that constitutes the proton wire was conserved in all four structures, indicating that the enzyme was structurally capable of proton transfer. A volume of density corresponding to an atom with more electron density than oxygen was observed near the side chains of His64, Asn62, and Asn67 and was modeled as a sodium ion, though the exact identity of this atom is not clear from crystallographic analysis. However, the resolution of the structures and the possibility of partial occupancy of this atom convolute an absolute determination of the atom type.

The proton shuttle residue, His64, which normally occupies two conformations, was observed only in the “in” conformation in all four mutants. Additionally, there was a change in the position of residues His3 and His4. Typically at this resolution, electron density for His3 and His4 are not observed due to the inherent disorder of the N-terminus of HCA II. In these four mutants, distinct electron density is observed for His3 and His4, showing that this residue occupies a conformation that is distinct from structures that have reported coordinates for this residue (Fisher *et al.*, 2005; Fisher *et al.*, 2007a) (Figure 5-5). The position of these residues is such that the side chain of His3 is located near the “out” conformation of His64 (Figure 5-6). A small amount of additional density can be observed extending off of the backbone of His3, however it was not modeled into, as it does not cover an entire residue.

Discussion

Despite its position near the surface of the protein, Lys170 may play a role in fine-tuning the properties of His64, the proton shuttle residue. Mutation of Lys170 to alanine, aspartate, glutamate, or histidine resulted in alterations of the conformation and pK_a of His64 as well as the rate of proton transfer. The crystal structures of the four mutants reveal that His64 is always located in the “in” conformation. Also, it was observed that two N-terminal histidines, His3 and His4 have distinct electron density, indicating an ordering of the N-terminus. The location of His3 is such that the “out” conformation of His64 is blocked, with the side chain of His3 located in an apparent pi-stacking interaction with Trp5 (Figure 5-6). It cannot be said for certain whether the ordering of these two residues is a result of or a cause of the conformational “locking” of His64. Although support for the former is provided by the structure of K170D, in which the side chain of Asp170 interacts with the carbonyl oxygen of Asn62 (distance = 3.2 Å). In turn, the carbonyl oxygen appears to interact with the N^{δ1} atom of His64 (Figure 5-7). Interestingly, the density for His3 appears to be the strongest for this mutant.

Regardless of this cause/effect relationship, distinct changes in the kinetic properties of proton transfer were observed that are attributable to the orientation of His64. The pK_a of His64, as described by ¹⁸O-exchange, was decreased in all four mutants, with values ranging from 6.3 – 6.7, compared to 7.2 for wild-type. Such a decrease is likely due to the hydrophobic environment occupied by His64 in this conformation. In fact, a decrease in pK_a to a value of 6 was observed in the structure of Y7F HCA II, a mutant in which His64 was also seen to occupy only the “in” conformation (Fisher *et al.*, 2007b).

The decrease in pK_a allows His64 to become a better proton donor, an effect of which is an increase in the rate of proton transfer, k_B , in the dehydration direction (Table 5-2). This effect is reversed, however, when considering the opposite direction, the hydration of CO_2 . As an example, the value of k_{cat} in the hydration direction is $1 \times 10^6 \text{ s}^{-1}$ for wild-type HCA II (Khalifah, 1971), but is decreased to about $0.5 \times 10^6 \text{ s}^{-1}$ in K170A. This difference reflects evolution of the enzyme to have no preference for one direction of the catalytic cycle, thus allowing for a tight regulation of intracellular pH. This is due to a nearly equal pK_a for both the zinc-bound water and His64. However, this work does suggest that Lys170 plays a role in tuning the pK_a of His64, allowing for equal enzymatic efficiency in both directions.

Conclusions

These results highlight the role of a residue located very distant from the active site core in fine-tuning the acid-base properties of HCA II. Lys170 is located approximately 15 Å away from the zinc, near the location of His64. The results presented in this chapter show that mutation at Lys170 results in a decrease in the pK_a of His64, a residue that is vital for efficient proton transfer. This decrease allows for His64 to be a more efficient proton donor, which is its role in the dehydration direction of catalysis. Therefore, in the dehydration direction, the mutant enzymes, particularly K170E, offer an enzyme that has a higher rate of proton transfer. The cost of this, however, is a decrease in the catalytic efficiency of the enzyme in the hydration direction. Taken together with previous mutagenic analyses, it is apparent that the active site environment is finely tuned by several residues near the proton wire to allow for efficient proton transfer in both the hydration and dehydration directions (Fisher *et al.*, 2007b). It can also be concluded from these studies that certain areas of the protein

are intolerant to mutation, even though, at first glance, these areas may be hypothesized to have only minute effects. It is thus not surprising that these mutations in HCA II have not been observed in nature, as the enzyme would be less effective in maintaining pH homeostasis. These studies also suggest that further analysis should be carried out in these regions to identify other residues that may be vital for proper catalysis.

Table 5-1. Data collection and refinement statistics for the Lys170 variant structures of HCA II.

Parameter	K170A	K170D	K170E	K170H
Space group	$P 2_1$	$P 2_1$	$P 2_1$	$P 2_1$
Cell dimensions				
a, b, c (Å)	42.6, 41.6, 72.8	42.6, 41.6, 72.8	42.6, 41.5, 72.7	42.7, 41.6, 72.8
β (°)	104.5	104.4	104.4	104.5
Resolution (Å)	50-1.65 (1.71-1.65) ^a	50-1.75 (1.81-1.75)	50-1.75 (1.81-1.75)	50-1.75 (1.81-1.75)
R_{sym} ^b (%)	6.9 (41.4)	6.2 (38.7)	6.7 (38.8)	5.4 (32.3)
$I/(\sigma)I$	12.5 (2.1)	20.7 (2.4)	16.4 (2.3)	19.0 (3.3)
Completeness	98.4 (98.1)	92.2 (80.9)	93.1 (80.4)	92.7 (80.9)
Redundancy	2.7 (2.6)	3.2 (3.0)	3.1 (2.8)	3.2 (3.1)
$R_{\text{factor}}^c/R_{\text{free}}^d$ (%)	16.8/19.7	16.6 (19.8)	16.9 (20.3)	16.3 (19.5)
No. atoms				
Protein	2076	2071	2075	2081
Water	139	101	84	102
B-factors				
Protein	14.9/17.5	14.8/17.4	15.7/17.1	15.3/18.1
Water	29.2	26.7	26.4	27.3
rmsd	0.011/1.299	0.012/1.361	0.013/1.388	0.012/1.334
(bond/angle)				
Ramachandran plot (%)				
Allowed	89.4	88.9	88.9	88.9
Additionally allowed	10.1	10.6	10.6	10.6
Generously allowed	0.5	0.5	0.5	0.5

^a Values in parentheses are for the highest resolution shell. ^b $R_{\text{sym}} = (\sum |I - \langle I \rangle| / \sum \langle I \rangle) \times 100$. ^c $R_{\text{cryst}} = (\sum ||F_o| - |F_c|| / \sum |F_o|) \times 100$. ^d R_{free} is calculated the same as R_{cryst} , except with 5% of the data omitted from refinement.

Table 5-2. Apparent values of pK_a and maximal rate constants for kinetic measurements of catalysis by wild type and site-specific mutants of HCA II at residue 170 obtained by ^{18}O exchange at 25 °C.^a

Enzyme	pK_a (His64) ^b	k_B (μs^{-1}) ^b	pK_a (ZnH_2O)	k_{cat}/K_M ($\mu\text{M}^{-1} \text{s}^{-1}$)
Wild-type	7.2 ± 0.1	0.8 ± 0.1	6.9	100
K170A	6.7 ± 0.1	1.2 ± 0.1	7.0	110
K170D	6.7 ± 0.1	1.5 ± 0.2	7.0	120
K170E	6.3 ± 0.1	4.0 ± 0.4	7.1	150
K170H	6.7 ± 0.1	1.6 ± 0.1	6.9	120

^a Solutions contained 25 mM of all species of CO_2 at sufficient sodium sulfate to maintain ionic strength at 0.2 M, without any added buffers. ^b These values were obtained by a least-squares fit of the data of Figure 5-3 to eq 5-4 in which the value of pK_a (ZnH_2O) was fixed at the value determined from R_1 shown in the fourth column of this Table.

Table 5-3. Values of the pK_a for the zinc-bound water and the maximal value of k_{cat}/K_M for the catalysis of the hydration of 4-nitrophenylacetate by variants of HCA II at 25 °C.

Enzyme	pK_a (ZnH_2O)	k_{cat}/K_M ($\text{M}^{-1} \text{s}^{-1}$)
Wild-type	7.0	2800
K170A	7.0	1600
K170D	7.1	1850
K170E	6.9	1890
K170H	6.9	1760

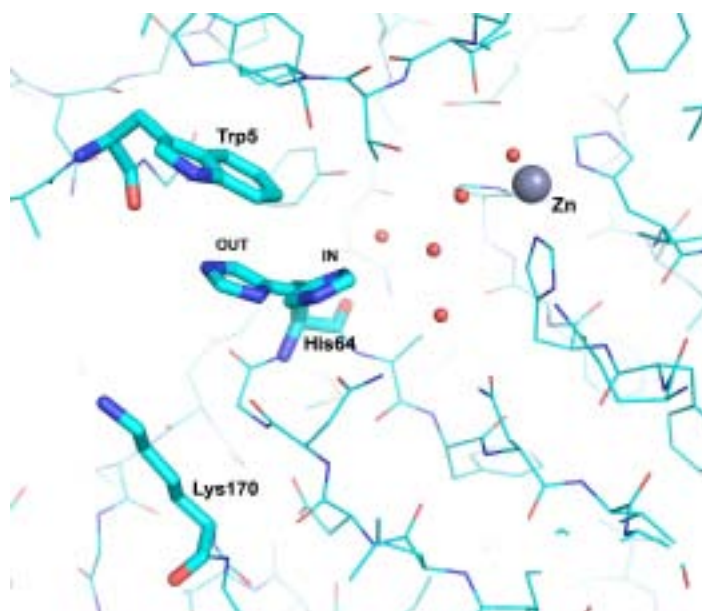


Figure 5-1. The protein environment around the proton shuttle residue His64 includes residues Trp5 and Lys170. The “out” conformation of His64 is in a near pi-stacking interaction with Trp5. On the opposite side, His64 is neighbored by the solvent-mediated proton wire (red spheres), which connects it to the zinc (purple sphere).

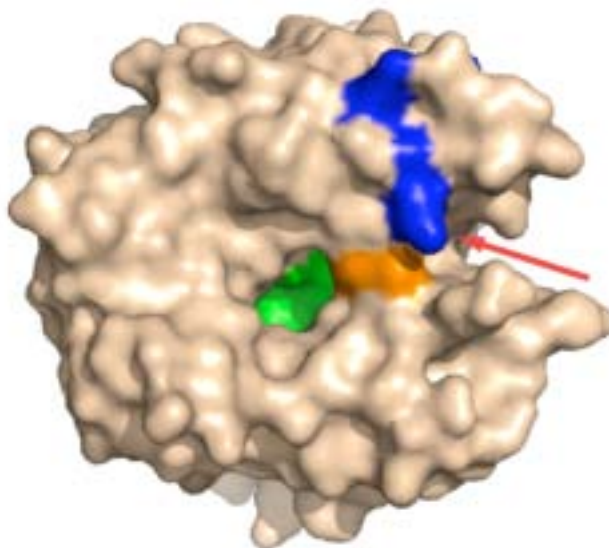


Figure 5-2. A surface representation of HCA II shows the location of Lys170 relative to the active site core. Shown in green is the base of the active site pocket, located at the center of the enzyme. Adjacent to this is the proton shuttle residue His64, shown in orange. Directly adjacent to His64 is a basic patch, composed of Lys168, Lys170 and Lys172 (blue). Of these three, Lys170 lies the closest to His64 (4.4 Å), as indicated by the red arrow.

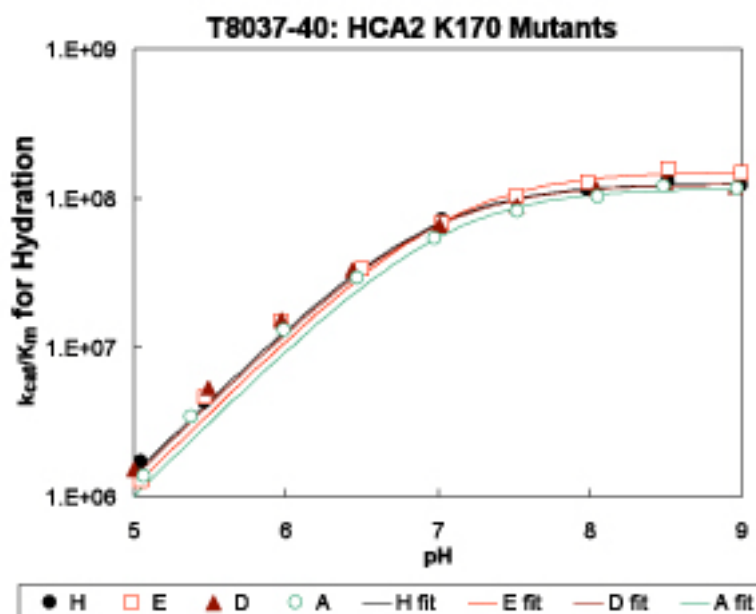


Figure 5-3. The pH dependence of $k_{\text{cat}}/K_{\text{M}}$ is apparently unchanged in the four Lys170 mutants. The data shown are measured for the dehydration reaction using the ^{18}O -exchange method. All measurements were taken at 25 °C with a total CO_2 concentration of 25 mM and an ionic strength of 200 mM and no buffer.

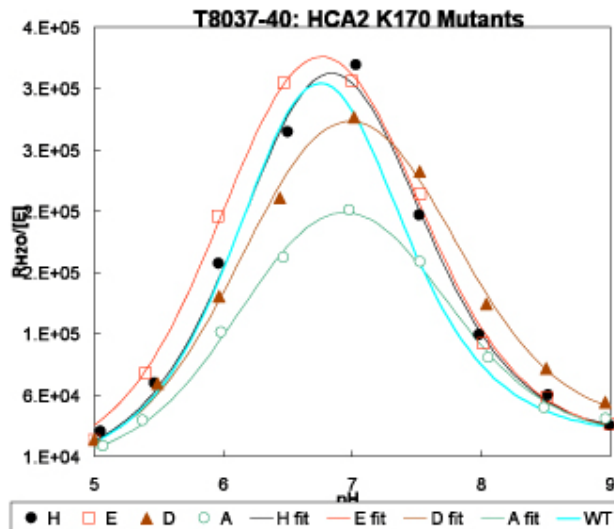


Figure 5-4. Mutation of Lys170 results in a change in the rate and pH dependence of the proton transfer controlled value of $R_{H_2O}/[E]$. Measurements were made using the same conditions described in Figure 5-3.

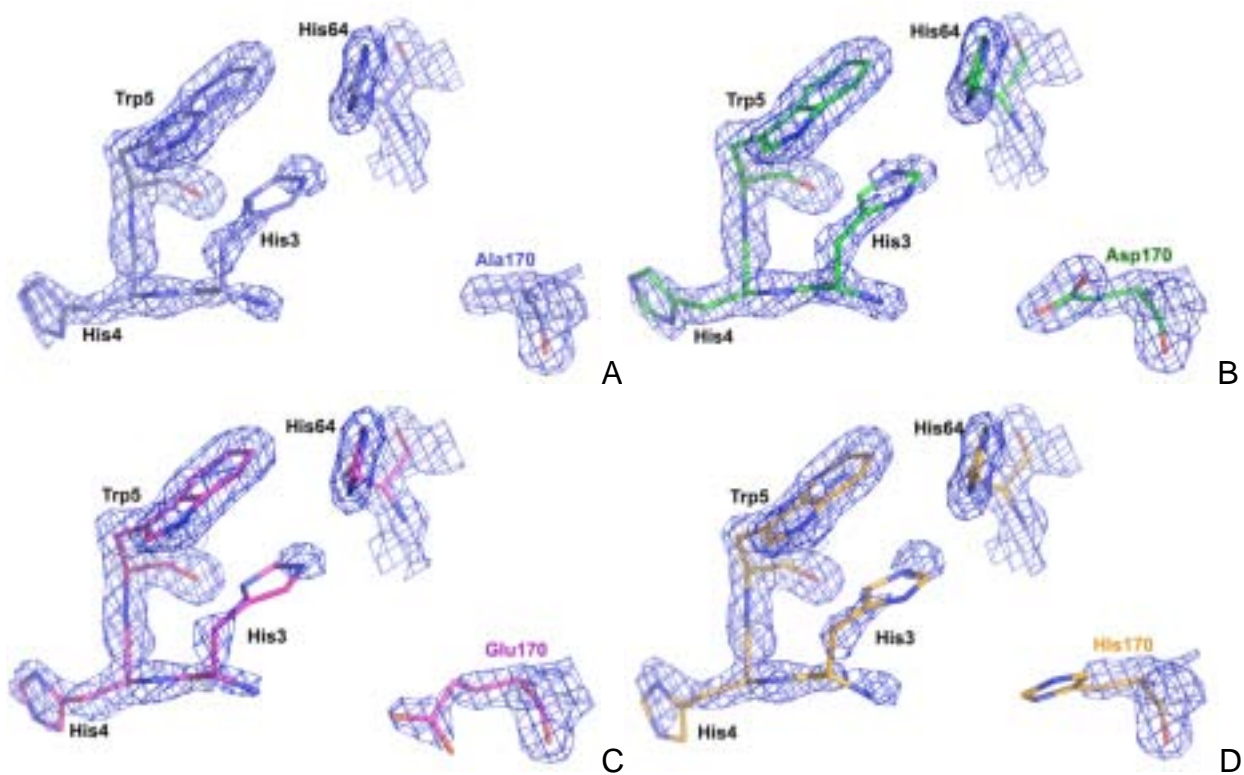


Figure 5-5. The electron density corresponding to His3 is visible in all four Lys170 HCA II mutants, although to varying degrees. The density shown for the four mutants [(A) K170A, (B) K170D, (C) K170E, (D) K170H] is a $2F_O - F_C$ Fourier map contoured to 1.5σ . The density is also shown for residues His4, Trp5 and His64. The density around Trp5 serves as a comparison for the four panels.

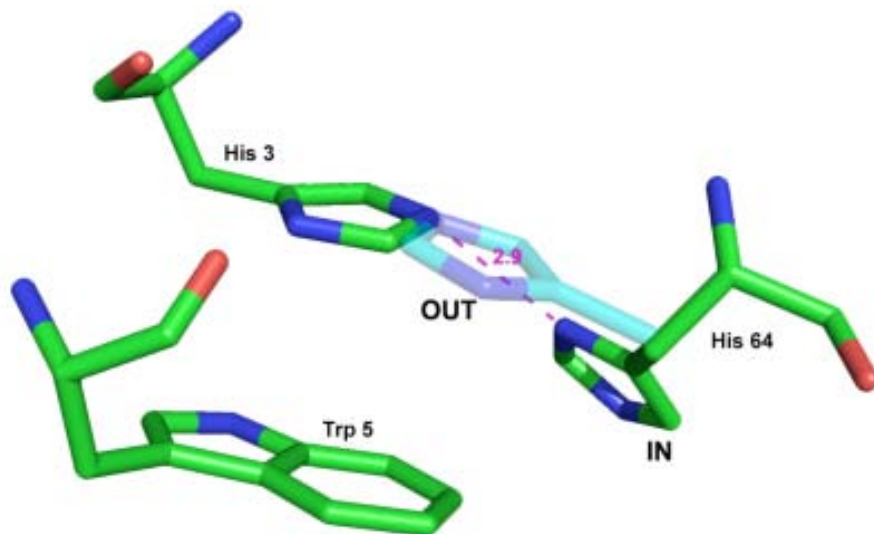


Figure 5-6. The location of His3 in all four mutants is roughly the same, apparently pi-stacking with the side chain of Trp5. In this location, the side chain of His3 directly interferes with His64 in its “out” conformation, with less than 3 Å between His3 and the “in” conformation of His64 (magenta dashes).

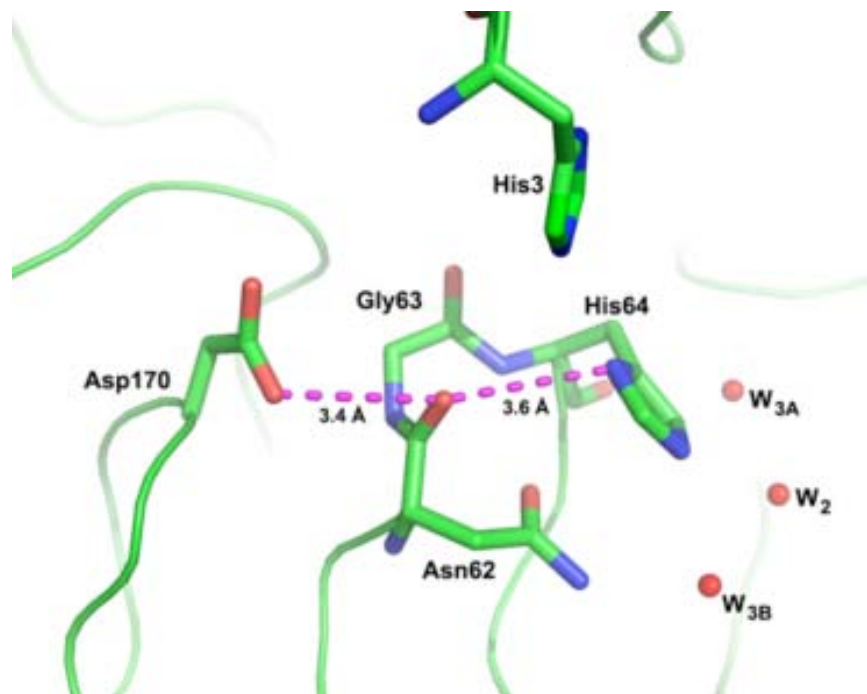


Figure 5-7. A novel interaction is observed between residues 64 and 170 in the structure of K170D HCA II. This is an indirect interaction mediated by the carbonyl oxygen of Asn62. The distances of the interactions Asp170-Asn62 and Asn62-His64 are approximately 3.4 Å and 3.6 Å, respectively (magenta dashes). As a reference, the proton wire solvent molecules are shown (red sphere).

CHAPTER 6
UNDERSTANDING THE MECHANISM OF γ -CA FROM *METHANOSARCINA*
THERMOPHILA: A COMPARISON WITH THE α -CA, HUMAN CARBONIC
ANHYDRASE II

As was discussed in Chapter 1, despite the catalysis of the same reaction, there is virtually no structural homology among the classes of CA, an indication of the physiological importance of this enzyme in all forms of life. The proposed mechanism for all classes involves a metal-bound hydroxide nucleophilically attacking the carbon of CO₂, resulting in bicarbonate. Chapters 4 and 5 discussed catalysis from a structural point of view for the α -CA, HCA II. Myriad other studies have been done on the α -CAs, with relatively few studies dealing with any of the other classes. Not surprisingly, a large majority of the crystal structures available are of the α -CAs, with only a handful of β -CA structures and only two unique structures of γ -CAs (Rowlett, 2009; Ferry, 2009). This chapter will look at the active site of the archetypal γ -CA from *Methanosarcina thermophila*, particularly as compared to the active site organization of HCA II, in order to help elucidate the structural basis for catalysis.

Introduction

The reaction catalyzed by the carbonic anhydrases is vital for the survival of nearly every known organism, as evidenced by the occurrence of at least one CA in nearly every organism, with the exception of *Mycoplasma genitalium* (Fraser *et al.*, 1995). Despite the wide occurrence of CAs and the population size of the *Archaea* domain of life, only two unique CAs have been characterized from organisms in this domain. The first was a β -CA from *Methanobacterium thermoautotrophicum* (Smith & Ferry, 1999; Strop *et al.*, 2001). The other was the γ -CA from *M. thermophila* (Cam), the first structurally characterized enzyme from this class (Kisker *et al.*, 1996).

Sequence-based database searches have revealed the existence of γ -CA-like genes in plants, green algae, proteobacteria, archaea, and cyanobacteria (Parisi *et al.*, 2004). Alignment of these sequences suggests that there are two distinct classes of γ -CA, based on the presence (Cam) or absence (CamH) (*Pyrococcus horikoshii* γ -CA, for example) of an acidic loop that lies directly adjacent to the active site (Figure 6-1). The metal coordinating histidines appear to occur in nearly all of these sequences, indicating metal-binding competence. Interestingly, previous biochemical studies suggest that this acidic loop and another residue, Cam-Glu62 (not present in the CamH class), are important for the presence of CA activity (Tripp & Ferry, 2000). The lack of these two features in CamH may indicate a different function, although two CamH enzymes have been shown to have some carbonic anhydrase activity (Ferry, 2009).

Cam is a trimeric enzyme with three active sites, each situated at the interface between two monomers (Figure 6-2). Unless purposely replaced with cobalt, the active site contains zinc coordinated by three histidines and a solvent molecule. Two of the histidines are from one monomer while one is contributed by the neighboring monomer. The physiological relevance of zinc is debatable, however, as the preparation of Cam anaerobically in either *E. coli* or *M. acetivorans*, produces an iron enzyme that is more active than Zn-Cam (MacAuley *et al.*, 2009). The aquatic environment of these archaea suggests that iron is the relevant metal, as zinc is limiting in these environments. In any case, the active site is flanked by two surface loops, one of which is the previously mentioned acidic loop (Figure 6-3).

This chapter presents structural data on mutations at two sites in Cam, Trp19 and Tyr200. A comparison of Cam with HCA II shows that these two residues may have

catalytic implications that were previously deduced for similar residues in HCA II. Trp19 in Cam is positioned adjacent to the proton shuttle residue Glu84 (Tu *et al.*, 2002). Similarly, in HCA II, Trp5 apparently π -stacks with the proton shuttle residue His64. The importance of this tryptophan is highlighted by the interaction of the proton rescue agent 4-methylimidazole (4-MI) with HCA II in the proton transfer deficient mutant H64A (Duda *et al.*, 2003). 4-MI sits in a location similar to the His64 “out” conformation, stacking with the side chain of Trp5. Another HCA II residue that has been shown to effect catalysis is Tyr7. A mutation to phenylalanine resulted in a mutant that had a greatly increased rate of proton transfer, as discussed in the previous chapter (Fisher *et al.*, 2007b). Tyr200 in Cam appears to be positioned in an equivalent location and is therefore hypothesized to play a similar role. The structures of four mutants, W19A, W19F, W19N, and Y200A are presented.

Materials and Methods

Enzymes

Site-directed mutagenesis of the Cam gene-containing plasmid was performed to create mutations at residues 19 and 200. The proteins were over-expressed in *E. coli*, and the cells were harvested by centrifugation. The pellet was suspended in 50 mM potassium phosphate, pH 6.8, supplemented with zinc sulfate and passed twice through a French pressure cell at 20000 lb/in². DNase I and RNase A were added after the first pass to reduce lysate viscosity. The lysate was clarified by centrifugation at 20000 *xg* and the protein was purified as follows by Sabrina Zimmerman in James G. Ferry's laboratory at Penn St. University. First, the supernatant was applied to a Q-Sepharose column (GE Healthcare) and the protein was eluted by a linear gradient of 0→1 M sodium chloride with elution occurring at about 0.5 M NaCl. Further purification was

accomplished by adding ammonium sulfate to the fractions (1.5 M final) and running the sample on a phenyl-Sepharose column (GE Healthcare) equilibrated with 100 mM potassium phosphate, pH 7 and 1.5 M ammonium sulfate. The protein was eluted with a 1.5→0 M ammonium sulfate gradient with a peak around 0.75 M. Protein purity was assessed by SDS-PAGE analysis and the protein concentration was determined by Bradford assay.

Crystallization and Data Collection

All mutants were crystallized using the hanging-drop vapor diffusion technique with a reservoir solution of 5% PEG 8000 and 250 mM ammonium sulfate. After sitting overnight, a heavy amount of precipitation was observed. Despite this, crystals were observed after approximately 4 weeks, with a size of ~1 mm³. Two of the mutants, Y200S and Y200F crystallized, however there was no observed diffraction, despite multiple attempts.

Diffraction data were collected using the in-house set up described in Chapter 2. The crystal-detector distance was set at 100 mm with an oscillation angle of 1° per image. A total of 90° of data were collected for each crystal. The data were then indexed, integrated, and scaled using *HKL2000* (Otwinowski & Minor, 1997). All four mutants were solved to comparable resolution (1.6-1.8 Å) in the space group P 2₁3 with isomorphous unit cells (*a* ~83.5). The R_{sym} for each mutant were: 4.6 for W19A, 6.4 for W19F, 3.4 for W19N, and 5.7 for Y200A. The high symmetry of the unit cell allowed for nearly 100% completeness in all cases with high redundancy, though only about 50 images were used for each structure. Complete data processing statistics are presented in Table 6-1.

Refinement

All structures were refined using the program *REFMAC5* in the *CCP4* suite of programs (Collaborative Computational Project, Number 4, 1994; Murshudov *et al.*, 1997). Structures were refined until the R_{factor} reached convergence, with a final $R_{\text{factor}}/R_{\text{free}}$ of approximately 17/20% for all mutants. One residue, Met65, refined to a position with unfavorable ϕ and ψ angles. The electron density was clear for this residue, so it was left in this conformation. Final refinement statistics are given in Table 6-1.

Results

Overall, the structures of the four mutants were identical to that of wild-type Cam (PDB ID 1qrg, Iverson *et al.*, 2000). The largest difference between the mutant and wild-type structures was the conformation of a loop composed of residues Glu62, Gly63, and Met64 (62-63-64 loop) (Figure 6-4). This conformation was observed in all four mutants and does not occur in any of the other Cam structures currently available in the PDB. To ensure a lack of model bias in the electron density maps, the loop was removed prior to refinement. The $F_{\text{O}}-F_{\text{C}}$ density map clearly shows the position of the loop, indicating that this is the correct conformation, despite the unfavorable nature of the ϕ and ψ angles of Met65 (Figure 6-5). There was some evidence that this loop occupied both conformations in the W19F structure, so both conformations were built in this structure. There was a large electron density peak observed adjacent to the zinc ion, indicating that something electron rich was coordinated to the metal. Two previous structures of Zn and Co-Cam have been solved with a sulfate molecule in this exact position. Therefore, this density was modeled as a sulfate in all four structures, though the occupancy of the sulfate was adjusted so that there were no large, negative $F_{\text{O}}-F_{\text{C}}$

density peaks at the sulfate. Additionally a metal was found at the 3-fold symmetry axis in Y200A Cam. This metal was modeled as an iron, which left no residual F_O-F_C electron density (negative or positive). The iron is coordinated by three methionines, Met55, one from all three monomers. It should be noted that the analysis of this density is convoluted due its overlap with the 3-fold crystallographic symmetry axis.

Discussion

The structures of four mutants of Cam have been solved using x-ray crystallography and have revealed a previously unseen structural feature. The loop composed of residues 62-64 occupies a distinctly different conformation than that reported in previous Cam structures. In this conformation the side chain of Met64 is shifted by nearly 11 Å as measured at the S^δ atoms. In wild-type Cam the Met64 side chain buries itself into the core of the protein. The observed rotation of the loop seen in the mutant Cam structures results in the side chain of Met64 pointing out towards the surface of the protein, almost completely solvent exposed. No role for this has been postulated and kinetic profiles will need to be completed before a complete understanding is reached.

One effect of this conformational change is that the proton shuttle residue Glu84 is observed almost solely in one conformation. In the previously reported Cam structures this residue occupies at least two distinct positions, analogous to the “in” and “out” conformations of His64 in HCA II. The side chain of Glu84 points towards the zinc in the structure of Zn-Cam with a water bound at the zinc (PDB ID 1qrg) (Iverson *et al.*, 2000). In the structures of Zn-Cam bound with either bicarbonate or sulfate, the side chain of Glu84 points away from the zinc ion. In its inward orientation, Glu84 appears to hydrogen bond to a water molecule that is within hydrogen bonding distance of the zinc-

bound solvent or compound. This indicates that there may be a pH effect on the orientation of Glu84, as has been observed many times for His64 (for example, Nair & Christianson, 1991).

Preliminary kinetic analysis suggests that the Trp19 mutants are catalytically deficient, while the Tyr200 mutants are more catalytically efficient (J. G. Ferry, personal communication). However, a complete kinetic work-up will be required before any conclusions are drawn about the mutational effects on catalysis.

Table 6-1. Data processing and refinement statistics for the structures of the Cam mutants.

Parameter	W19A	W19F	W19N	Y200A
Space group	<i>P</i> 2 ₁ 3	<i>P</i> 2 ₁ 3	<i>P</i> 2 ₁ 3	<i>P</i> 2 ₁ 3
Cell dimensions (a) (Å)	83.492	83.621	83.580	83.498
Resolution (Å)	20-1.6 (1.66-1.6) ^a	20-1.8 (1.86-1.8)	50-1.65 (1.71-1.65)	25-1.8 (1.86-1.8)
R _{sym} ^b (%)	4.6 (46.0)	6.4 (48.4)	3.4 (24.9)	5.7 (34.9)
I/(σ)I	34.2 (3.6)	21.8 (2.8)	47.0 (4.7)	26.5 (4.3)
Completeness	99.8 (100.0)	99.9 (99.9)	99.6 (99.1)	100.0 (100.0)
Redundancy	6.8 (6.5)	5.6 (5.4)	7.2 (3.5)	6.5 (6.2)
R _{factor} ^c /R _{free} ^d (%)	17.5/20.8	16.5 (20.3)	16.9 (20.6)	16.0 (19.4)
No. atoms				
Protein	1612	1587	1603	1573
Water	71	62	80	59
B-factors				
Protein (main/side)	22.1/25.0	23.0/26.3	21.1/24.4	18.0/21.1
Water	36.4	37.1	35.4	30.0
RMSD (bond/angle)	0.013/1.456	0.015/1.597	0.013/1.459	0.015/1.491
Ramachandran plot (%)				
Allowed	88.4	90.7	90.2	90.7
Additionally allowed	11.0	8.7	9.2	8.7
Disallowed ^e	0.6	0.6	0.6	0.6

^a Values in parentheses are for the highest resolution shell. ^b $R_{sym} = (\sum |I - \langle I \rangle| / \sum \langle I \rangle) \times 100$. ^c $R_{cryst} = (\sum ||F_o| - |F_c|| / \sum |F_o|) \times 100$. ^d R_{free} is calculated the same as R_{cryst} , except with 5% of the data omitted from refinement. ^e The orientation of Met64 is disallowed, however the electron density for this residue clearly shows its position.

```

CanH      1  -----MNL P-----NPRKQHP
cam       1  MMFNKQIFTILILSLSLALAGSGCISEGAEDNVAQEITVDEFSHIRENPVTPMNPEPSAP
consensus 1  mmfnkqiftililslslalagsgcisegaednvaqeitvdef Nl enpvtpwNP  P

CanH     12  RYSKRAWISETAVIIGNISYADYVFGFNVLRADEFGSSITVQSGCNVQDNVVVHSLSH
cam      61  VIDPTAYIDPQASVIGEVITGANVMYSPMASIRSDE-GMPIFVGDRSNVQDGVVLALET
consensus 61  v  AWI  A iIG isIa  V V P A lR DEpG  I V  NVQD VVvH L

CanH     72  SD-----LVGKNTSLAHSCIVHGPCRIGEGCFIGFGAVVFDCHIG
cam     120  INEEGEPIEDNIVEVDGKEYAYIGNNVSLANQSQVNGPAAVGDDTFIGMQAFVFKSKVG
consensus 121  eegepiednivevdgkeyaY vG N SLAH  VHGP  iGe  FIG  A VF  iG

CanH     113  KDTLVLHRSVVRGIDIFSGRIYFDGTVITROAYANALEPITKENT--EFKRSVVVRAHIEL
cam     180  NNCVLEPRSAAGVTIPDGRYIPAGMVVTSQAEADKLPEVTDDYAYSHTEAVVYVNVHL
consensus 181  lv RS  Gi I  GR vP G ViT QA A L it e ys  VV Ni L

CanH     171  VEGYMKLREE
cam     240  AEGYKETS---
consensus 241  EGY  ees

```

Figure 6-1. An alignment of Cam (from *M. thermophila*) and CamH (from *M. acetivorans*) shows the lack of the acidic loop (black box) in CamH. Residues are numbered according to each sequence, with green indicating identical residues, cyan showing conservative mutation, and red showing insertions/deletions.

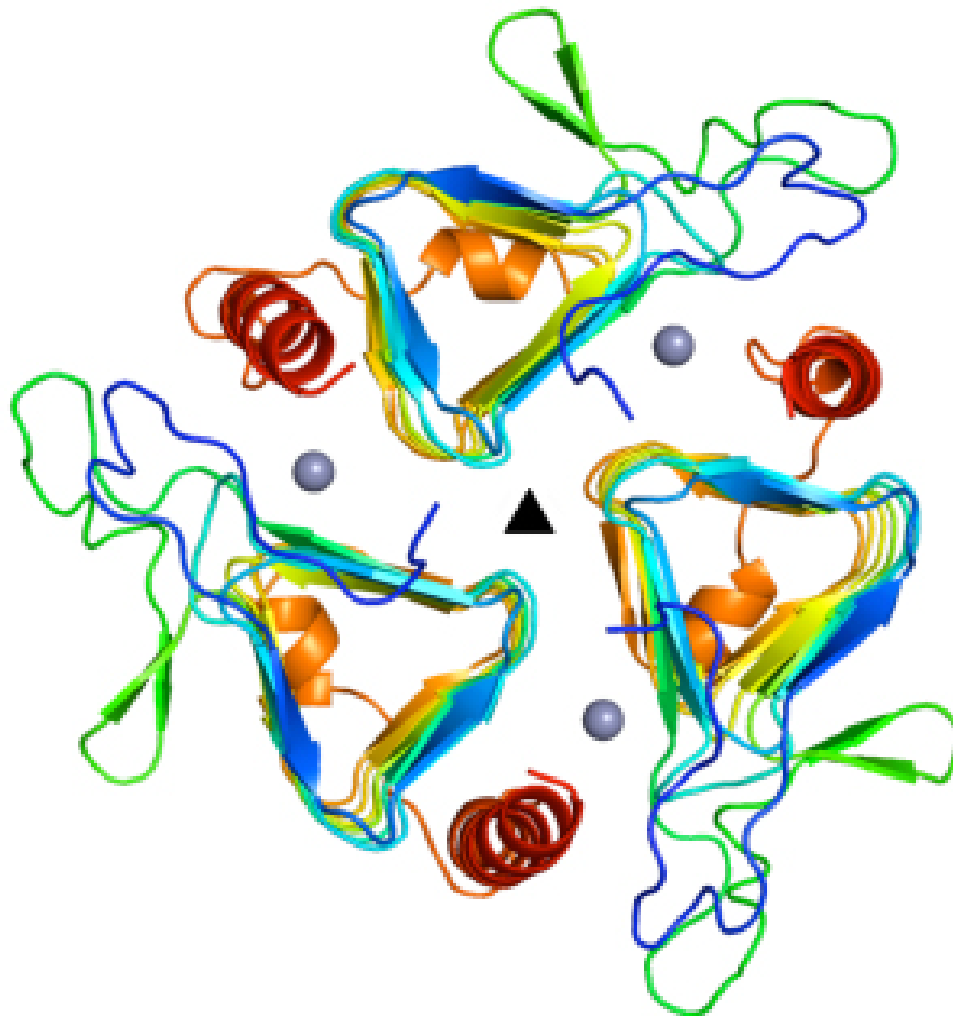


Figure 6-2. The trimeric organization of Cam yields three active sites per enzyme, each at a monomer-monomer interface. The active sites are indicated by the zinc ion at their center (purple spheres). The 3-fold axis of symmetry is readily apparent in this view (black triangle).

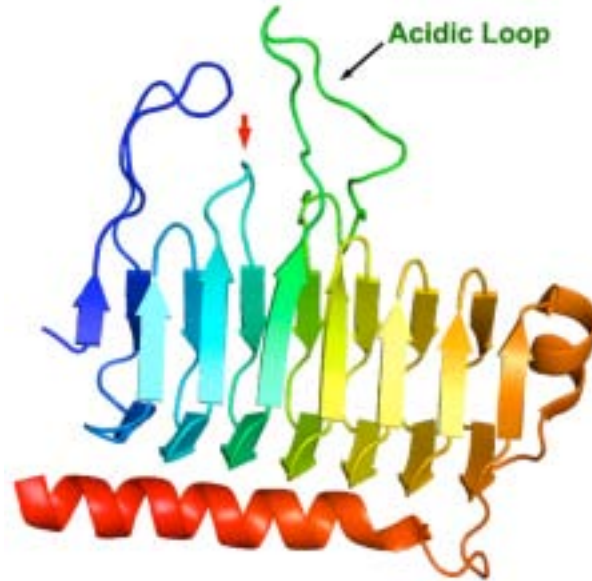


Figure 6-3. The structure of a Cam monomer shows a left-handed β -helix topology with several N-terminal (blue) surface loops and a C-terminal (red) α -helix. The acidic loop that differentiates the Cam and CamH classes is identified in green and the loop 63-64-65 loop is indicated by a red arrowhead.

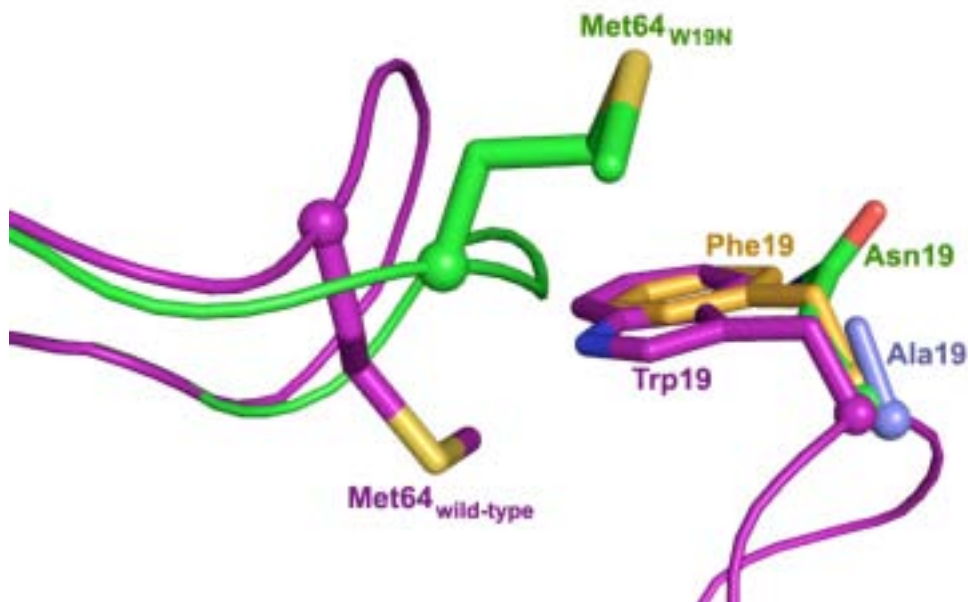


Figure 6-4. The 63-64-65 loop in the mutants of Cam occupies a different conformation than that observed in all reported Cam structures. The orientation of the side chain of Met64 is clearly different in the two structures (magenta = wild-type, green = mutants) with a maximal distance of 11 between identical atoms. The loop of W19N is shown here, however the conformation of the loop is the same for all mutants, with W19F displaying both conformations. Side chains for the W19 mutants are also shown here.

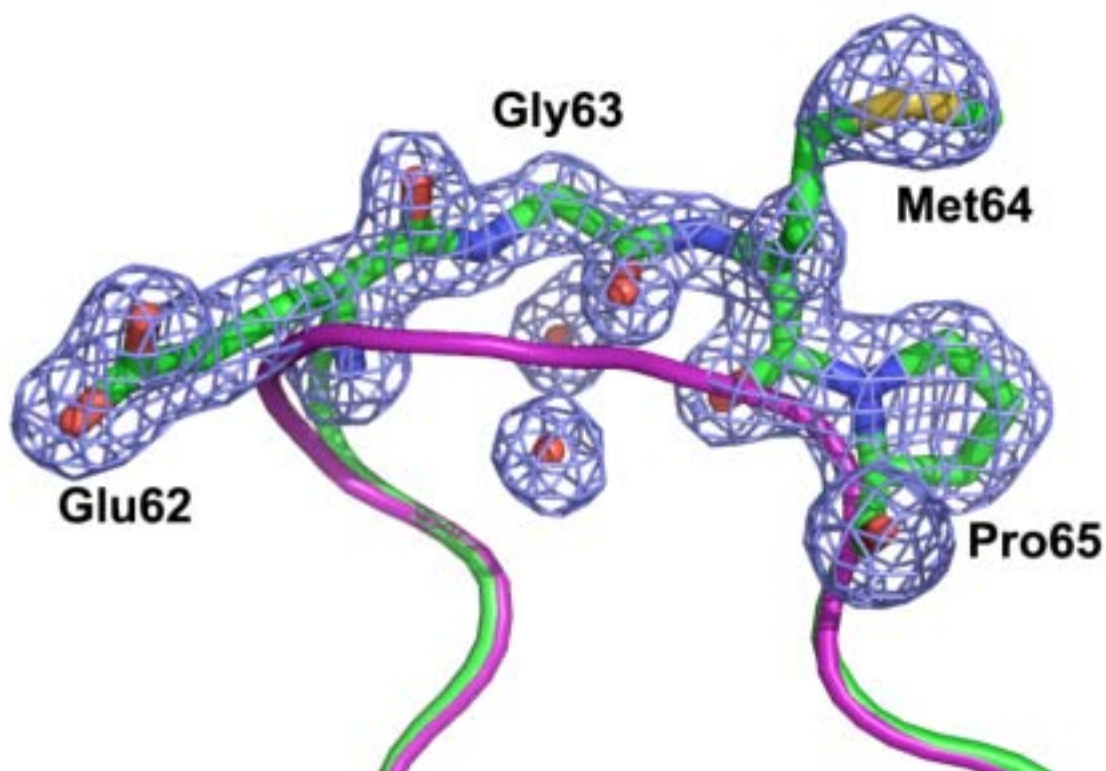


Figure 6-5. The electron density for the 62-63-64 loop clearly defines its orientation in the structure of W19N Cam. Shown as blue mesh is F_O-F_C electron density calculated with the loop removed. The side chains are built into this density (green sticks) and are in a novel conformation as compared to wild-type (magenta backbone) (PDB ID 1qrg, Iverson *et al.*, 2000). Also shown is Pro65, a residue which remains more or less unchanged between the mutant and wild-type structures.

CHAPTER 7 CONCLUSIONS AND FUTURE DIRECTIONS

Summary and Conclusions

X-ray crystallographic studies provide insight into an enzyme's structural basis of catalysis. In order to truly understand catalysis, however, one must acquire knowledge of the structural changes that underlie kinetic defects in mutant and inhibited enzymes. The trapping of substrates, products, and transition states in the enzyme's active site will provide additional knowledge. This analysis can be complicated by many factors including the ability to crystallize enzymes, the resolution of the structure, as well as the lifetime of the enzyme-substrate/product/transition state complex.

Chapters 2 and 3 presented mutational analyses of human manganese superoxide dismutase in order to understand the protein's role in catalysis. It was shown that secondary metal-coordinating ligands play a major role in finely tuning the catalytic properties of the active site metal. This was illustrated by the E162D and E162A mutants of human MnSOD, which had a fraction of the activity of the wild-type enzyme. Crystal structures revealed that this was due to a loss or weakening of the interaction between residue 162 and His163 of a neighboring monomer. His163 acts as a manganese ligand, and mutation at residue 162 is hypothesized to affect the tuning of the redox properties of the manganese. These effects were not as drastic as those observed in the equivalent mutant of *E. coli* MnSOD, E170A, which lost metal specificity and, therefore, activity. This difference highlights the importance of the entire protein in modulating the active site environment, as human and *E. coli* MnSODs are nearly identical at all atomic positions within 10 Å of the manganese.

Chapter 3 discussed mutational analysis at residue Phe66, located at the mouth of the active site, away from the Mn. The results showed that even the slightest change in the enzyme's structure could lead to drastic catalytic deficiencies. Both mutants, F66A and F66L, exhibited slightly deficient catalytic activity as compared to wild type. Analysis was extended to the role of the active site cavity was described with respect to the product-inhibited state of MnSOD. This site represents one of the only differences between *E. coli* and human MnSOD, with the human form being the more strongly product inhibited of the two. It was shown that F66L human MnSOD has a very low level of product inhibition, with a level nearly identical to that of *E. coli* MnSOD. Crystallographic analysis suggested that the mobility of the solvent in the active site pocket correlated to the level of product inhibition, with more mobility resulting in a lower level of product inhibition. These results suggest that the unique features of this product-inhibited state may be controlled by the flexibility of these active site amino acids.

In Chapter 4 the capturing of the substrate CO₂ was shown to be a rather static process in HCA II. The fast turnover of this complex was previously thought to be a severe limitation to ever achieving this complex. However, the use of high pressures and low temperatures allowed for a stoppage of catalytic activity. This demonstrated that the hydrophobic portion of the HCA II active site is responsible for providing a solvating environment for the hydrophobic CO₂ molecule. Additionally, it was shown that the zinc has virtually no role in substrate binding. All of the presented results were in agreement with previous biochemical studies, therefore supporting the role of the observed binding site as the physiologically relevant site.

The role of the protein environment in catalysis with regards to HCA II was discussed in Chapter 5, as elucidated by mutational analysis of Lys170. It was shown that despite being a long distance from the active site, Lys170 plays a role in fine-tuning the environment of the proton shuttle residue His64. Kinetic analysis indicated that the pK_a of His64 was decreased in all four mutants examined. The result is an increase in the rate of proton transfer in the dehydration direction. These variants don't occur in nature, however, as the lowering of the pK_a of the proton shuttle residue would decrease the catalytic efficiency when this residue acts as a proton acceptor, in the hydration direction. This suggests that when one is examining the structure of an enzyme that one must look beyond the obvious active site residues and consider how neighboring amino acids may effect the local electrostatic environment.

An extension of this analysis to the γ -CA from *M. thermophila* was discussed in Chapter 6. Despite a lack of overall structural homology, there may be localized similarities between the γ - and α -CAs. Mutational analysis of residues Trp19 and Tyr200 in Cam illustrated the structural role of these residues and provided insight into a unique conformation of a loop lying near the active site metal. Preliminary kinetic analysis suggests that these mutations also cause changes in the catalytic efficiency of the enzyme.

Taken together, the results presented here suggest that there is an underappreciation of the role of the total protein in tuning the catalytic efficiency of an enzyme. It is acceptable to begin analysis of the structure-based catalytic mechanism of an enzyme. However, one must extend analysis beyond the defined active site in order to truly understand how an enzyme functions. The body of the protein acts in a

way beyond simply precise placement of catalytic residues and cofactors, even in apparently static catalytic mechanisms.

Future Directions

The antiproliferative effects of weakly product-inhibited forms of human MnSOD provide a means of countering the growth of cancerous cells. The use of non-human SODs for this purpose is complicated by the possible immune response to these enzymes. Therefore further study of the product-inhibited state is required to generate efficient forms of the enzyme for this purpose. Additional mutational analyses at Phe66 offer a starting point. Combining single mutants that exhibit lower product inhibition may also yield variants with therapeutic potential. One such double mutant would be H30N/F66L, where both single mutants offer decreased product inhibition for different reasons. The double mutant may provide a weakly product-inhibited enzyme with otherwise wild-type activity.

It will also be necessary to directly visualize the product-inhibited state of the enzyme. Crystallographic analysis of this state will require high resolution as the substrate will only appear as a dioxygen species (the protons are nearly invisible to all but the highest resolution crystal structures). One method may be to initially reduce the Mn with hydrogen peroxide, as it is known that product inhibition occurs during the second stage of catalysis in which the Mn exists in the +2 state. Subsequent addition of superoxide (i.e. potassium superoxide) may allow for the trapping of the substrate if cryopreservation occurs rapidly after its addition.

The elucidation of the substrate binding site in HCA II, as presented in Chapter 4, provided a major leap forward in understanding the catalytic mechanism during the first stage of catalysis. The extension of this technique to β and γ -class enzymes, as well as

other CO₂-binding proteins, will facilitate the elucidation of how substrate binds in these enzymes, and, therefore, how the catalytic cycle proceeds.

Additionally for HCA II, the events that occur during the proton transfer step are not completely understood. The importance of this stage of catalysis in the CAs is underscored by the presumed presence of hydrogen-bonded networks across all classes of CA. Little knowledge is available on the protonation states of the atoms involved in this step. One solution is to use neutron diffraction to visualize the locations of protons. Neutrons scatter off of atomic nuclei, and the replacement of protons with deuterons provides signal levels on the same order as carbons, nitrogens, and oxygens. There has been great progress on the neutron crystal structure of HCA II (Fisher *et al.*, 2009), though a complete analysis has not yet been finished. The initial structure will only scratch the surface, though, and neutron structures at various pH's and in the presence of transition states/products (bicarbonate in T200H, for example) will provide atomic-level detail of the catalytic process.

The research presented in the Chapter 6 will also need to be completed in order to help determine the structural basis for catalysis in Cam. Kinetic studies will be completed to determine the effects of the mutations on catalysis. Additionally a complete analysis will only be possible if the crystal structures of the Tyr200 mutants are solved. Also, the crystal of iron-bound Cam will be required to visualize the positions of active site atoms and to gain an understanding of what is bound to the metal in more physiologically relevant conditions.

LIST OF REFERENCES

- Abreu, I. A., Hearn, A., An, H., Nick, H. S., Silverman, D. N. & Cabelli, D. E. (2007). *Biochemistry*, **47**, 2350-2356.
- Abreu, I. A., Rodriguez, J. A. & Cabelli, D. E. (2005). *J. Phys. Chem. B*, **109**, 24502-24509.
- Alber, B. E., Colangelo, C. M., Dong, J., Stalhandske, C. M., Baird, T. T., Tu, C., Fierke, C. A., Silverman, D. N., Scott, R. A. & Ferry, J. G. (1999). *Biochemistry*, **38**, 13119-13128.
- Alexander, R. S., Nair, S. K. & Christianson, D. W. (1991). *Biochemistry*, **30**, 11064-11072.
- Barondeau, D. P., Kassmann, C. J., Bruns, C. K., Tainer, J. A. & Getzoff, E. D. (2004). *Biochemistry*, **43**, 8038-8047.
- Becker, H. M. & Deitmer, J. W. (2007). *J. Biol. Chem.* **282**, 13508-13521.
- Bertini, I., Luchinat, C., Monnanni, R., Roelens, S. & Moratal, J. M. (1987). *J. Am. Chem. Soc.* **109**, 7855-7856.
- Borgstahl, G. E., Parge, H. E., Hickey, M. J., Beyer, W. F., Jr., Hallewell, R. A. & Tainer, J. A. (1992). *Cell*, **71**, 107-118.
- Borgstahl, G. E., Pokross, M., Chehab, R., Sekher, A. & Snell, E. H., (2000). *J. Mol. Biol.* **296**, 951-959.
- Borthwick, K. J., Kandemir, N., Topaloglu, R., Kornak, U., Bakkaloglu, A., Yordam, N., Ozen, S., Mocan, H., Shah, G. N., Sly, W. S. & Karet, F. E. (2003). *J. Med. Genet.* **40**, 115-121.
- Bowler, C., Van Kaer, L., Van Camp, W., Montagu, M. V., Inzé, D. & Dhaese, P. (1990). *J. Bacteriol.* **172**, 1539-1546.
- Breton, S. (2001). *J. Panc.* **2**, 159-164.
- Brunger, A. T. (1992). *Nature*, **355**, 472-475.
- Brunger, A. T., Adams, P. D., Clore, G. M., DeLano, W. L., Gros, P., Grosse-Kunstleve, R. W., Jiang, J. S., Kuszewski, J., Nilges, M., Pannu, N. S., Read, R. J., Rice, L. M., Simonson, T. & Warren, G. L. (1998). *Acta Crystallogr.* **D54**, 905-921.
- Bull, C., Niederhoffer, E. C., Yoshida, T. & Fee, J. A. (1991). *J. Am. Chem. Soc.* **113**, 4069-4076.
- Butler, J. N. (1982). *Carbon Dioxide Equilibria and Their Applications*. Reading, MA: Addison-Wesley.

- Cabelli, D. E., Guan, Y., Leveque, V., Hearn, A. S., Tainer, J. A., Nick, H. S. & Silverman, D. N. (1999). *Biochemistry*, **38**, 11686-11692.
- Carlioz, A. & Touati, D. (1986). *EMBO J.* **5**, 623-630.
- Chen, H. Y., Hu, R. G., Wang, B. Z., Chen, W. F., Liu, W. Y., Schröder, W., Frank, P. & Ulbrich, N. (2002). *Arch. Biochem. Biophys.* **404**, 218-226.
- Chin D. & Means A. R. (2000). *Trends Cell Biol.* **19**, 322-328.
- Coleman, J. E. (1992). *Annu. Rev. Biochem.* **61**, 897-946.
- Collaborative Computational Project, Number 4 (1994). *Acta Cryst.*, **D50**, 760-763.
- Corena, M. P., Seron, T. J., Lehman, H. K., Ochrietor, J. D., Kohn, A., Tu, C. & Linsler, P. J. (2002). *J. Exp. Biol.* **205**, 591-602.
- Davies, M. J. (2005). *Biochim. Biophys. Acta*, **170**, 93-109.
- Davis, C. A., Hearn, A. S., Fletcher, B., Bickford, J., Garcia, J. E., Leveque, V., Melendez, J. A., Silverman, D. N., Zucali, J., Agarwal, A. & Nick, H. S. (2004). *J. Biol. Chem.* **279**, 12769-12776.
- Domsic, J. F., Avvaru, B. S., Kim, C. U., Gruner, S. M., Agbandje-McKenna, M., Silverman, D. N. & McKenna, R. (2008). *J. Biol. Chem.* **283**, 30766-30771.
- Domsic, J. F. & McKenna, R. (2009). *Biochim. Biophys. Acta*, In the press.
- Duda, D., Govindasamy, L., Agbandje-McKenna, M., Tu, C, Silverman, D. N., McKenna, R. (2003). *Acta Cryst.* **D59**, 93-104.
- Duda, D. & McKenna, R. (2004). *Handbook of Metalloproteins*, edited by A. Messerschmidt, W. Bode & M. Cygler, pp. 249-263. West Sussex, England: John Wiley & Sons, Ltd.
- Duda, D., Tu, C. K., Qian, M. Z., Laipis, P., Agbandje-McKenna, M., Silverman, D. N. & McKenna, R. (2001). *Biochemistry*, **40**, 1741-1748.
- Edwards, R. A., Baker, H. M., Whittaker, M. M., Whittaker, J. W., Jameson, G. B. & Baker, E. N. (1998). *J. Biol. Inorg. Chem.* **3**, 161-171.
- Edwards, R. A., Whittaker, M. M., Whittaker, J. W., Baker, E. N. & Jameson, G. B. (2001). *Biochemistry*, **40**, 15-27.
- Elleuche, S. & Pöggeler, S. (2009). *Curr. Genet.* **55**, 211-222.
- Emsley, P. & Cowtan, K. (2004). *Acta Crystallogr.* **D60**, 2126-2132.

- Farin, F. M., Hitosis, Y., Hallagan, S. E., Kushleika, J., Woods, J. S., Janssen, P. S., Smith-Weller, T., Franklin, G. M., Swanson, P. D., Checkoway, H. (2001). *Mov. Disord.*, **16**, 707-707.
- Farr, S. B., D'Ari, R. & Touati, D. (1986). *Proc. Natl. Acad. Sci. USA*, **83**, 8268-8272.
- Ferry, J. G. (2009). *Biochim. Biophys. Acta*, In the press.
- Fierke, C. A., Calderone, T. L. & Krebs, J. F. (1991). *Biochemistry*, **30**, 11054-11063.
- Fink, R. C. & Scandalios, J. G. (2002). *Arch. Biochem. Biophys.* **399**, 19-36.
- Fisher, S. Z., Kovalevsky, A. Y., Domsic, J. F., Mustyakimov, M., Silverman, D. N., McKenna, R. & Langan, P. (2009). *Acta Cryst.* **F65**, 495-498.
- Fisher, S. Z., Maupin, C. M., Budayova-Spano, M., Govindasamy, L., Tu, C. K., Agbandje-McKenna, M., Silverman, D. N., Voth, G. A. & McKenna, R. (2007a). *Biochemistry*, **46**, 2930-2937.
- Fisher, S. Z., Prada, J. A. H., Tu, C., Duda, D., Yoshioka, C., An, H. Q., Govindasamy, L., Silverman, D. N. & McKenna, R. (2005). *Biochemistry*, **44**, 1097-1105.
- Fisher, S. Z., Tu, C., Bhatt, D., Govindasamy, L., Agbandje-McKenna, M, McKenna, R. & Silverman, D. N. (2007b). *Biochemistry*, **46**, 3803-3813.
- Fraser, C. M., Gocayne, J. D., White, O., Adams, M. D., Clayton, R. A., Fleischmann, R. D., Bult, C. J., Kerlavage, A. R., Sutton, G. G. & Kelley, J. M. *et al.* (1995). *Science*, **270**, 397-403.
- Gould, S. M. & Tawfis, D. S. (2005). *Biochemistry*, **44**, 5444-5452
- Greenleaf, W. B., Perry, J. J., Hearn, A. S., Cabelli, D. E., Lepock, J. R., Stroupe, M. E., Tainer, J. A., Nick, H. S. & Silverman, D. N. (2004). *Biochemistry*, **43**, 7038-7045.
- Guan, Y., Hickey, M. J., Borgstahl, G. E., Hallewell, R. A., Lepock, J. R., O'Connor, D., Hsieh, Y., Nick, H. S., Silverman, D. N. & Tainer, J. A. (1998). *Biochemistry*, **37**, 4722-4730.
- Gupta, A. S., Webb, R. P., Holaday, A. S. & Allen, R. D. (1993). *Plant Physiol.* **103**, 1067-1073.
- Hakansson, K., Carlsson, M., Svensson, L. A. & Liljas, A. (1992). *J. Mol. Biol.* **227**, 1192-1204.
- Harman, D., (1956). *J. Gerontol.* **11**, 298-300.
- Hearn, A. S., Fan, L., Lepock, J. R., Luba, J. P., Greenleaf, W. B., Cabelli, D. E., Tainer, J. A., Nick, H. S. & Silverman, D. N. (2004). *J. Biol. Chem.* **279**, 5861-5866.

- Hearn, A. S., Stroupe, M. E., Cabelli, D. E., Lepock, J. R., Tainer, J. A., Nick, H. S. & Silverman, D. N. (2001). *Biochemistry*, **40**, 12051-12058.
- Hearn, A. S., Stroupe, M. E., Cabelli, D. E., Ramilo, C. A., Luba, J. P., Tainer, J. A., Nick, H. S. & Silverman, D. N. (2003). *Biochemistry*, **42**, 2781-2789.
- Henry, R. P. (1996). *Annu. Rev. Physiol.* **58**, 523-538.
- Hovnik, T., Dolzan, V., Ursic, B. N., Podkrajsek, K. T. & Battelino, T. (2009). *Diab. Care*, In the press.
- Hsieh, Y., Guan, Y., Tu, C., Bratt, P. J., Angerhofer, A., Lepock, J. R., Hickey, M. J., Tainer, J. A., Nick, H. S. & Silverman, D. N. (1998). *Biochemistry*, **37**, 4731-4739.
- Hsu, J. L., Hsieh, Y., Tu, C., O'Connor, D., Nick, H. S. & Silverman, D. N. (1996). *J. Biol. Chem.* **271**, 17687-17691.
- Hu, P. Y., Lim, E. J., Ciccolella, J., Strisciuglio, P. & Sly, W. S. (1997). *Human Mut.* **9**, 383-387.
- Iverson, T. M., Alber, B. E., Kisker, C., Ferry, J. G. & Rees, D. C. (2000). *Biochemistry*, **39**, 9222-9231.
- Jackman, J. E., Merz, K. M., Jr. & Fierke, C. A. (1996). *Biochemistry*, **35**, 16421-16428.
- Jeyakanthan, J., Rangarajan, S., Mridula, P., Kanaujia, S. P., Shiro, Y., Kuramitsu, S., Yokoyama, S. & Sekar, K. (2008). *Acta Cryst.* **D64**, 1012-1029.
- Jonasson, P., Aronsson, G., Carlsson, U. & Jonsson, B. H. (1997). *Biochemistry*, **36**, 5142-5148.
- Karlsson, J., Hitonen, T., Husic, H.D., Ramazanov, Z. & Samuelsson, G. (1995). *Plant Physiol.* **109**, 533-539.
- Khalifah, R. G. (1971). *J. Biol. Chem.* **246**, 2561-2573.
- Kim, C. U., Kapfer, R. & Gruner, S. M. (2005). *Acta Crystallogr.* **D61**, 881-890.
- Kim, G., Lee, T.-H., Wetzel, P., Geers, C., Robinson, M. A., Myers, T. G., Owens, J. W., Wehr, N. B., Eckhaus, M. W., Gros, G., Wynshaw-Boris, A. & Levine, R. L. (2004). *Mol. Cell. Biol.*, **24**, 9942-9947.
- Kisker, C., Schindelin, H., Alber, B. E., Ferry, J. G. & Rees, D. C. (1996). *EMBO J.* **15**, 2323-2330.
- Krebs, J. F., Fierke, C. A., Alexander, R. S. & Christianson, D. W. (1991). *Biochemistry*, **30**, 9153-9160.

- Krebs, J. F., Ippolito, J. A., Christianson, D. W. & Fierke, C. A. (1993). *Biochemistry*, **32**, 4496-4505.
- Lah, M. S., Dixon, M. M., Pattridge, K. A., Stallings, W. C., Fee, J. A. & Ludwig, M. L. (1995). *Biochemistry*, **34**, 1646-1660.
- Lane, T. W., Saito, M. A., George, G. N., Pickering, I. J., Prince, R. C. & Morel, F. M. (2005). *Nature*, **435**, 42.
- Laskowski R. A., MacArthur, M. W., Moss, D. S. & Thornton, J. M. (1993). *J. App. Cryst.* **26**, 283-291.
- Lebovitz, R. M., Zhang, H., Vogel, H., Cartwright, J., Jr., Dionne, L., Lu, N., Huang, S. & Matzuk, M. M. (1996). *Proc. Natl. Acad. Sci. USA*, **93**, 9782-9787.
- Leveque, V. J., Stroupe, M. E., Lepock, J. R., Cabelli, D. E., Tainer, J. A., Nick, H. S. & Silverman, D. N. (2000). *Biochemistry*, **39**, 7131-7137.
- Leveque, V. J., Vance, C. K., Nick, H. S. & Silverman, D. N. (2001). *Biochemistry*, **40**, 10586-10591.
- Li, Y., Huang, T. T., Carlson, E. J., Melov, S., Ursell, P. C., Olson, J. L., Noble, L. J., Yoshimura, M. P., Berger, C., Chan, P. H., Wallace, D. C. & Epstein, C. J. (1995). *Nat. Gene.* **11**, 376-381.
- Liang, J. Y. & Lipscomb, W. N. (1990). *Proc. Natl. Acad. Sci. USA*, **87**, 3675-3679.
- Lindahl, L., Svensson, L. A. & Liljas, A. (1993). *Proteins Struct. Funct. Bioinformat.* **15**, 177-182.
- Lindskog, S. (1983). *Zinc Enzymes*, edited by T. G. Spiro, pp. 78-121. West Sussex, England: John Wiley and Sons.
- Macauley, S. R., Zimmerman, S. A., Apolinario, E. E., Evilia, C., Hou, Y. M., Ferry, J. G. & Sowers, K. R. (2009). *Biochemistry*, **48**, 817-819.
- Maliekal, J., Karapetian, A., Vance, C., Yikilmaz, E., Wu, Q., Jackson, T., Brunold, T. C., Spiro, T. G. & Miller, A. F. (2002). *J. Am. Chem. Soc.* **124**, 15064-15075.
- McAdam, M. E., Fox, R. A., Lavelle, F. & Fielden, E. M. (1977). *Biochem. J.* **165**, 71-79.
- McCord, J. M. (2002). *Methods Enzymol.* **349**, 331-341.
- Meldrum, N. U. & Roughton, F. J. W. (1932). *J. Physiol. (London)*, **75**, 15-16.
- Merz, K. M., Jr. (1991). *J. Am. Chem. Soc.* **113**, 406-411.
- Miller, A. F. (2004). *Curr. Opin. Chem. Biol.* **8**, 162-168.

- Mitsuhashi, S., Mizushima, T., Yamashita, E., Yamamoto, M., Kumasaka, T., Moriyama, H., Ueki, T., Miyachi, S. & Tsukihara, T. (2000). *J. Biol. Chem.* **275**, 5521-5526.
- Möllsten A., Marklund, S. L., Wessman, M., Svensson, M., Forsblom, C., Parkkonen, M., Brismar, K., Groop, P. H. & Dahlquist, G. (2007). *Diabetes*, **56**, 265-269.
- Mizuno, K., Whittaker, M. M., Bachinger, H. P. & Whittaker, J. W. (2004). *J. Biol. Chem.* **279**, 27339-27344.
- Muñoz, I. G., Moran, J. F., Becana, M. & Montoya, G. (2005). *Protein Sci.* **14**, 387-394.
- Murshudov, G. N., Vagin, A. A. & Dodson, E. J. (1997). *Acta. Cryst.* **D53**, 240-255.
- Nair, S. K. & Christianson, D. W. (1991). *J. Am. Chem. Soc.* **113**, 9455-9458.
- Noor, R., Mittal, S. & Iqbal, J. (2002). *Med. Sci. Monit.* **8**, RA210-RA215.
- Otwinowski, Z. & Minor, W. (1997). *Methods Enzymol.* **276**, 307-326.
- Palenik, B., Brahamsha, B., Larimer, F. W., Land, M., Hauser, L., Chain, P., Lamerdin, J., Regala, W., Allen, E. E., McCarren, J., Paulsen, I., Dufresne, A., Partensky, F., Webb, E. A. & Waterbury, J. (2003). *Nature*, **424**, 1037-1042.
- Parisi, G., Perales, M., Fornasari, M., Colaneri, A., Schain, N., Casati, D., Zimmermann, S., Brennicke, A., Araya, A., Ferry, J. G., Echave, J. & Zabaleta, E. (2004). *Plant Mol. Biol.* **55**, 193-207.
- Phillips, J. P., Campbell, S. D., Michaud, D., Charbonneau, M. & Hilliker, A. J. (1989). *Proc. Natl. Acad. Sci. USA*, **86**, 2761-2765.
- Purkerson, J. M. & Schwartz, G. J. (2007). *Kidney Int.* **71**, 103-115.
- Quint, P., Ayala, I., Busby, S. A., Chalmers, M. J., Griffin, P. R., Rocca, J., Nick, H. S. & Silverman, D. N. (2006). *Biochemistry*, **45**, 8209-8215.
- Quint, P. S., Domsic, J. F., Cabelli, D. E., McKenna, R., Silverman, D. N. (2008). *Biochemistry*, **47**, 4621-4628.
- Quint, P., Reutzel, R., Mikulski, R., McKenna, R. & Silverman, D. N. (2006). *Free Radical Biol. Med.* **40**, 453-458.
- Rabani, J. & Nielsen, S. O. (1969). *J. Phys. Chem.* **73**, 3736-3744.
- Ramilo, C. A., Leveque, V., Guan, Y., Lepock, J. R., Tainer, J. A., Nick, H. S. & Silverman, D. N. (1999). *J. Biol. Chem.* **274**, 27711-27716.
- Reaume, A. G., Elliott, J. L., Hoffman, E. K., Kowall, N. W., Ferrante, R. J., Siwek, D. R., Wilcox, H. M., Flood, D. G., Beal, M. F., Brown, R. H., Jr., Scott, R. W. & Snider, W. D. (1996). *Nat. Gene.*, **13**, 43-47.

- Roberts, S. B., Lane, T. W. & Morel, F. M. M. (1997). *J. Phycol.* **33**, 845-850.
- Rodriguez, A. M., Carrico, P. M., Mazurkiewicz, J. E. & Melendez, J. A. (2000), *Free Radic. Biol. Med.* **29**, 801-813.
- Rowlett, R. S. (2009). *Biochim. Biophys. Acta*, In the press.
- Sawaya, M. R., Cannon, G. C., Heinhorst, S., Tanaka, S., Williams, E. B., Yeates, T. O. & Kerfeld, C. A. (2006). *J. Biol. Chem.* **281**, 7546-7555.
- Schwartz, H. (1981). *J. Chem. Educ.* **58**, 101-105.
- Sheldrick, G. M. (2008). *Acta Crystallogr.* **A64**, 112-122.
- Silverman, D. N. (1982). *Methods Enz.* **87**, 732-752.
- Silverman, D. N. & Lindskog, S. (1988). *Acc. Chem. Res.* **21**, 30-36.
- Silverman, D. N. & McKenna, R. (2007). *Acc. Chem. Res.* **40**, 669-675.
- Sly, W. S. & Hu, P. Y. (1995). *Annu. Rev. Biochem.* **64**, 375-401.
- Smith, M. W. & Doolittle, R. F. (1992). *J. Mol. Evol.* **34**, 175-184.
- Smith, K. S. & Ferry, J. G. (1999). *J. Bacteriol.* **181**, 6247-6253.
- Smith, R. A., Kelso, G. F., Blaikie, F. H., Proteous, C. M., Ledgerwood, E. C., Hughes, G., James, A. M., Ross, M. F., Asin-Cayueta, J., Cochemé, H. M., Filipovska, A. & Murphy, M. P. (2003). *Biochem. Soc. Trans.* **31**, 1295-1299.
- So, A. K., Espie, G. S., Williams, E. B., Shively, J. M., Heinhorst, S., Cannon, G. C. (2004). *J. Bacteriol.* **186**, 623-630.
- St-Pierre, J., Buckingham, J. A., Roebuck, S. J. & Brand, M. D. (2002). *J. Biol. Chem.* **277**, 44784-44790.
- Strange, R. W., Yong, C. W., Smith, W. & Hasnain, S. S. (2007). *Proc. Natl. Acad. Sci. USA*, **104**, 10040-10044.
- Strop, P., Smith, K. S., Iverson, T. M., Ferry, J. G. & Rees, D. C. (2001). *J. Biol. Chem.* **276**, 10299-10305.
- Sugio, S., Hiraoka, B. Y. & Yamakura, F. (2000). *Eur. J. Biochem.* **267**, 3487-3495.
- Sundaresan, M., Yu, Z., Ferrans, V. J., Irani, K. & Finkel, T. (1995), *Science*, **270**, 296-299.

- Sunderhaus, S., Dudkina, N. V., Jansch, L., Klodmann, J., Heinemeyer, J., Perales, M., Zabaleta, E., Boekema, E. J. & Braun, H. P. (2006). *J. Biol. Chem.* **281**, 6482-6488.
- Tripp, B. C. & Ferry, J. G. (2000). *Biochemistry*, **39**, 9232-9240.
- Tu, C., Rowlett, R. S., Tripp, B. C., Ferry, J. G. & Silverman, D. N. (2002). *Biochemistry*, **41**, 15429-15435
- Tu, C. K., Silverman, D. N., Forsman, C., Jonsson, B. H. & Lindskog, S. (1989). *Biochemistry*, **28**, 7913-7918.
- Vagin, A. & Teplakov, A. (1997). *J. Appl. Crystallogr.* **30**, 1022-1025.
- Venta, P. J. (2000). *The Carbonic Anhydrases, New Horizons*, edited by W. R. Chegwidden, N. D. Carter & Y. H. Edwards, pp. 403-412. Switzerland: Birkhauser Verlag Basel.
- Venta, P. J., Welty, R. J., Johnson, T. M., Sly, W. S. & Tashian, R. E. (1991). *Am. J. Hum. Genet.* **49**, 1082-1090.
- Verpoorte, J. A., Mehta, S. & Edsall, J. T. (1967). *J. Biol. Chem.*, **242**, 4221-4229.
- Vince, J. W. & Reithmeier, R. A. F. (1998). *J. Biol. Chem.* **273**, 28430-28437.
- Whittaker, M. M. & Whittaker, J. W. (1997). *Biochemistry*, **36**, 8923-8931.
- Whittaker, M. M. & Whittaker, J. W. (1998). *J. Biol. Chem.* **273**, 22188-22193.
- Williams, T. J. & Henkens, R. W. (1985). *Biochemistry*, **24**, 2459-2462.
- Xue, Y., Liljas, A., Jonsson, B. H. & Lindskog, S. (1993). *Proteins*, **15**, 80-87.
- Youn, H. D., Kim, E. J., Roe, J. H., Hah, Y. C. & Kang, S. O. (1996). *Biochem. J.* **318**, 889-896.
- Youn, H. D., Youn, H., Lee, J. W., Yim, Y. I., Lee, J. K., Hah, Y. C. & Kang, S. O. (1996b). *Arch. Biochem. Biophys.* **334**, 341-348.
- Zheng, J., Domsic, J. F., Cabelli, D., McKenna, R. & Silverman, D. N. (2007). *Biochemistry*, **46**, 14830-14837.

BIOGRAPHICAL SKETCH

John Francis Domsic was born in Erie, PA in 1983. He attended Fort LeBoeuf High School, graduating in 2001. He immediately entered the undergraduate program at Allegheny College in Meadville, PA and completed his B.S. in Biology in 2005. He spent his senior year studying the capsid protein of bacteriophage HK97 under the guidance of Dr. Brandi Baros. In the fall of 2005, John began his graduate school training in the University of Florida's Interdisciplinary Program in the Biomedical Sciences. He joined the lab of Dr. Robert McKenna in the spring of 2006 to begin his research on the structural basis of catalysis in the metalloenzymes human manganese superoxide dismutase and the carbonic anhydrases.